INSTITUTE
FOR
AEROSPACE STUDIES

UNIVERSITY OF TORONTO

IDEAL EFFICIENCY OF PROPELLERS BASED ON THEODORSEN'S THEORY: A REVIEW AND COMPUTER STUDY, WITH EXTENDED PLUS SIMPLIFIED CHARTS

by

Stephen P. Foster

FOREWORD AND APPENDIX SEGMENTS

by

H. S. Ribner

February 1991

UTIAS Technical Note No. 271
CN ISSN 0082-5263

IDEAL EFFICIENCY OF PROPELLERS BASED ON THEODORSEN'S THEORY: A REVIEW AND COMPUTER STUDY, WITH EXTENDED PLUS SIMPLIFIED CHARTS

by

Stephen P. Foster

FOREWORD AND APPENDIX SEGMENTS

by

H. S. Ribner

Submitted October 1990

February 1991

UTIAS Technical Note No. 271
CN ISSN 0082-5263

Foreword

Computed early results of the M.A.Sc. project of Stephen Foster have been incorporated in a paper* by Ribner and Foster, to be published in the Journal of Aircraft. Substantial extensions and vastly more computed curves are included in the lengthy thesis.† These are presented in the context of a detailed review of relevant parts of Theodorsen's theory of propellers.

The present Technical Note is essentially a duplicate of the thesis (slightly revised), made more readily available. As such it contains expository accounts of aerodynamic theory and relevant mathematics not normally included in a research paper: on balance, it was decided to retain these.

Since the format and exposition are Foster's, but the concepts and analytical methods are a mix of Theodorsen's, his, and mine there are differences of interpretation. I have presented some additional thoughts in Appendix D: these take the form of new developments bearing on slipstream contraction and displacement velocity. In addition, a short direct derivation of the integral conservation equation for propeller power has been inserted as Appendix A.3.

H. S. Ribner

---

*Ribner, H. S., and Foster, S. P., "Ideal Efficiency of Propellers: Theodorsen Revisited," J. Aircraft, Vol. 27, No. 9, Sept. 1990, pp. 810-819.

†Foster, Stephen P., "Ideal Efficiency of Propellers: A Computer Study," University of Toronto Institute for Aerospace Studies, M.A.Sc. Thesis, Jan. 1990, 75 pp. + 50 charts.

Acknowledgement

Theodorsen's classical study of the theory of propellers forms the foundation of the present work. There are also major conceptual inputs from Professor H. S. Ribner; following traditional thesis format, these are not specifically indicated at the points of use. The research was supported by a grant to him from the Natural Sciences and Engineering Research Council of Canada, and by his tenure part-time at NASA Langley Research Center as a Distinguished Research Associate. The computations were carried out on the Cray X-MP/24 operated by the Ontario Centre for Large Scale Computation at the University of Toronto

Stephen P. Foster

Abstract

Ideal propeller performance is explored in an examination of Theodorsen's theory of propellers. This work presents an overview of the theory with analysis and interpretation. Computational methods are used in place of Theodorsen's analog techniques to calculate key parameters for more cases. In addition, relations between the fundamental quantities — thrust, power, advance, efficiency — are presented in his format plus a more convenient one that avoids iteration. Theodorsen's methodology is further applied to calculate the slipstream contraction; however, a slightly more general approach is taken with the removal of several light loading assumptions. A review of how the updated results may be applied to the design of single rotation propellers is also provided.

Contents

List of Figures

List of Tables

NOMENCLATURE

a_0 = displacement velocity at the propeller plane

$\bar{a}_0 = a_0/V$

c = blade element chord

$\bar{c} = c/R$

c_e = power loss coefficient $[\dot{E}/(1/2\rho V^3 \pi R_\infty^2)]$

c_p = power coefficient $[P/(1/2\rho V^3 \pi R_\infty^2)]$

$c_{p,p} = \left(\frac{R_\infty}{R}\right)^2 c_p$

$\hat{c}_p$ = power coefficient due only to wake overpressure

c_s = thrust coefficient $[T/(1/2\rho V^3 \pi R_\infty^2)]$

$c_{s,p} = \left(\frac{R_\infty}{R}\right)^2 c_s$

c_{ij}^{α} = influence coefficient for the velocity component in direction α at the i^{th} control point due to the j^{th} filament

$\hat{c}_s$ = thrust coefficient due only to wake overpressure

$\underline{e}^{\alpha}$ = principal coordinate unit vector

l = axial distance between turns

m = number of helical filaments per blade

(n_i^1, n_i^2, n_i^3) = coordinates of normal to the helicoid

n = number of wake diameters over which numerical integration of the Biot-Savart integral is performed

p = fluid pressure

p_0 = fluid pressure in the far field

r = radial distance from the propeller axis

$t_a = D_a/(1/2\rho V^2 \pi R^2)$

$t_t = \omega \mathcal{Q} /(1/2\rho V^3 \pi R^2)$

u = local flow speed relative to a propeller blade element

$\bar{u} = u/V$

$\vec{v}$ = disturbance velocity due to motion of the helical wake

$\vec{v}_i$ = induced velocity at i^{th} control point

v_z, v_t, v_r = axial, tangential, radial components of v

$w =$ rearward speed of helical wake infinitely far downstream of the propeller (the displacement velocity)

$\bar{w} = w/V$

$A =$ area of wake cross section projected on a plane perpendicular to the wake axis

$B =$ blade number

$C_L =$ blade section lift coefficient

$D_a =$ total axial force arising from blade drag

$\mathcal{D} =$ drag distribution along propeller blade

$\dot{E} =$ power lost to the fluid comprising the propeller wake

$\mathcal{E} =$ kinetic energy per unit length of 2-blade propeller in the limit of infinitely large advance ($\lambda \to \infty$)

$F_{ij} = \sum_{\alpha=1}^{3} c_{ij}^{\alpha} n_i^{\alpha}$

$K =$ non-dimensional circulation function

$K_{100} =$ approximation to K based on 100 filaments per blade

$P =$ propeller power

$\mathcal{P}_0 =$ geometric pitch of the propeller path

$\mathcal{P}(r) =$ pitch of the wake helicoid

$\mathcal{P}_\infty =$ far wake pitch

$Q =$ propeller torque

$\mathcal{Q} =$ torque due to blade drag

$Q_\infty^B =$ torque of B-blade propeller in the limit $\lambda \to \infty$

$R =$ propeller radius

$R_\infty =$ ultimate radius of the helical wake far downstream of the propeller

$\Delta R =$ absolute wake contraction

$S_j(x) = j^{th}$ cubic polynomial utilized in spline interpolation

$T =$ propeller thrust

$\hat{T} =$ thrust arising from wake overpressure

$V =$ Forward speed of propeller

$Y =$ contraction ratio $\left(\frac{\Delta R}{R}\frac{\kappa}{c_s}\right)$

$\hat{Y} =$ contraction coefficient $\frac{1}{2\bar{w}}\frac{\Delta R}{R}$

$\alpha =$ number which indicates a particular principal coordinate direction ($\alpha = 1, 2, 3$ corresponds to the x,y z axes respectively)

$\gamma_j =$ vortex strength of the j^{th} helical filament

$\hat{\gamma}_j = \gamma_j / wl$

$\phi =$ disturbance velocity potential

$\psi =$ angular offset from x-axis of vortex sheets at the xy plane

$\omega =$ angular speed of propeller

$\tilde{\omega} =$ angular velocity of helical rotation that is kinematically equivalent to axial motion with speed w

$\theta(r) =$ pitch angle of the wake helicoid

$\theta_0(r) =$ geometric pitch angle of the propeller path

$\sigma_B = Q_\infty^B / Q_\infty^2$

$\eta =$ propeller efficiency

$\eta_a =$ actuator disc efficiency

$\eta_\Delta =$ efficiency of differential element of thrust

$\lambda =$ advance coefficient $(V/\omega R_\infty)$

$\lambda_T =$ helical advance coefficient $[(V + w)/\omega R_\infty]$

$\lambda_P =$ propeller advance coefficient $(V/\omega R)$

$\rho =$ fluid density

$\kappa =$ mass coefficient $(\int v_z ds / wA)$

$\epsilon =$ axial kinetic energy loss factor $(\int v_z^2 ds / w^2 A)$

$\tau = 2n/\lambda_T$

$(\xi_j^1, \xi_j^2, \xi_j^3) =$ coordinates of a point on Υ

$(\zeta_i^1, \zeta_i^2, \zeta_i^3) =$ coordinates of the i^{th} control point

$\Gamma =$ propeller circulation function

$\vec{\Omega} =$ fluid vorticity

$\Upsilon_k =$ helical filament of radius r_j from k^{th} propeller blade

1 Introduction

1.1 The Propeller Problem

The function of a propeller, in the most general terms, is to produce thrust in order that forces opposing the motion of a vehicle through a fluid medium may be balanced. A propeller generates thrust by imparting a rearward change in momentum of the fluid through which it operates. The momentum change is a consequence of the aerodynamic forces of lift and drag that are generated along each blade. These forces are responsible for the total thrust and torque experienced by the propeller. Moreover, it is the reactions to these forces that gives rise to the change in kinetic energy and momentum of the fluid that flows through the disc swept by the propeller and subsequently forms the slipstream.

An important task of propeller theory is to model propeller operation with sufficent accuracy for prediction and design purposes. Prediction is concerned with the estimation of the thrust, torque and efficiency of a particular propeller design under given operating conditions. Many modern computational algorithms are available for the analysis of specific propeller designs. However, these codes do not give an indication of the highest possible efficiency, neglecting blade profile drag, given the set of basic propeller parameters: blade number, propeller advance coefficient, and power (or thrust) loading. This work, built within the theoretical framework of Theodorsen [1] examines the performance of ideal or optimum propellers using numerical techniques. Moreover, this work assists in the interpretation of Theodorsens's theory, updates and extends some of its main results.

1.2 Historical Background

Early developments in propeller theory were divided into two schools of thought. The first approach, proposed by Rankine in 1865, is known as the simple momemtum or actuator disc theory. Because of its extensive simplifying assumptions, the actuator disc theory provided only a very crude estimate of the upper limit to propeller efficiency. Propeller operation is modelled by a thin disc across which a discontinuous jump in pressure is produced; and, the resulting slipstream is modelled by a uniform velocity field wherein residual fluid axial kinetic energy constitutes the only loss mechanism. Consequently, the actuator disc theory (ADT) completely fails

[1] T. Theodorsen, *Theory of Propellers* , (New York: McGraw-Hill, 1948)

to fix propeller geometry. In addition, the actuator disc model is not a true limit case of the propeller. [2]

A second approach to the propeller problem was first proposed by W. Froude in 1878 and later expanded by Drzewiecki in 1892. The early blade element theory made blade geometry central to the analysis. As a basic premise of the theory, each propeller blade is modelled by a number of blade elements, each regarded as an independent airfoil with an impinging flow derived from translation and rotation of the blade. The aerodynamic properties of each element are determined exclusively from experimental data with arbitrarily assumed aspect ratios. Similar to actuator disc theory, no information is *derived* about propeller geometry; in contrast, the simple blade element theory predicts an efficiency of 100% for frictionless flow while the actuator disc model maintains that the ideal efficiency must be less than 100% for all non-zero loadings.

Attempts to reconcile fundamental differences between the two propeller models resulted in a marriage of the two theories. The idea was to couple the inflow velocity at the propeller plane from momentum theory with the conception of independent blade elements from the blade element theory. A great deal of empiricism still remained until the association of lift with circulation about a contour was made. Lanchester proposed in 1907 that the effective velocity at each blade element must include the velocity induced by a trailing vortex system.

Similar to wing theory, the vortex theory of the propeller led to the concept of an optimum distribution of circulation for minimum induced loss. In 1919, Betz proved that the optimum circulation distribution is realized when the self-induced motion of the trailing vortex system emulates the motion of a rigid screw surface; but, the complexity of the optimum circulation problem forced Betz to the simplifying assumption of infinite blade number. Prandtl subsequently derived an approximate correction factor to obtain solutions corresponding to finite blade numbers. Prandtl obtained these tip loss correction factors by modelling the wake by a cascade of planar lamina which move with the uniform axial velocity w. However, the tip loss correction factors gave reasonably accurate results only for propellers with large blade numbers or for propellers operating at small values of advance. It wasn't until 1929 that Goldstein [3] calculated an exact solution for

[2] T. Theodorsen, *Theory of Propellers* (New York:Mcgraw-Hill,1948), p. 31.

[3] S. Goldstein, 'On the Vortex Theory of Screw Propellers', Proc. Roy. Soc., London, Vol 123, 1929.

the optimum radial distribution of circultion for a propeller having a finite number of blades. Goldstein's analytic solution to the potential flow problem involves the use of Bessel functions and the evaluation of infinite series. Goldstein's method of solution was not without problems: his assumptions of light blade loadings raised concerns about the applicability of his results to normal design loadings. Moreover, Goldstein's series solution had certain convergence difficulties at large values of advance.

Theodorsen addressed some of the limitations of Goldstein's work in the form of a general theory of propellers. Theodorsen asserted that the Goldstein circulation functions need not be restricted to light loadings provided that reference is made to the same ultimate wake helix infinitely far downstream of the propeller. By formulating the problem in terms of parameters referring to the far wake, Theodorsen removed the propeller configuration (except blade number) from consideration, except as a final step in the design process. Theodorsen also addressed the problems involved with generating optimum circulation functions by employing an analog model to the potential flow problem: solutions were obtained experimentally by exploiting the mathematical identity of ideal fluid flow with the flow of electric current under equivalent boundary conditions. Theodorsen integrated these ideal circulation functions into a general theory which characterizes ideal propeller behavior including large advance coefficients and high blade loadings.

2 Flow Model

In the examination of ideal propeller properties, the flow field is assumed to be incompressible, irrotational and inviscid. Similar to wing theory, propeller theory is based on the concept of a trailing wake consisting of vorticity shed from each finite lifting surface . The wake is modelled by sheets of vorticity which are considered to be infinitely thin surfaces of discontinuity within a potential flow field. Specification of the wake geometry can be utilized to determine the ideal properties of the propeller. In fact, Theodorsen showed that thrust, torque and efficiency of the ideal propeller are completely determined by the far wake.

2.1 Potential Flow

The magnitude of vorticity at a point within a vortex field is defined as a limit of the circulation of the velocity field about a closed contour c per unit

enclosed area s,

$$\Omega = \lim_{s \to 0} \frac{\oint_c \vec{v} \circ \vec{dl}}{s} \tag{1}$$

In accordance with vector calculus convention, the vortex field may be expressed in terms of the velocity field by the relation

$$\vec{\Omega} = \vec{\nabla} \times \vec{v} \tag{2}$$

A region of the flow field is defined as being irrotational if $\vec{\Omega} = \vec{0}$ at all points within the region. Thus, the following vector identity for an arbitrary scalar function f,

$$\vec{\nabla} \times (\vec{\nabla} f) \equiv 0 \tag{3}$$

can be used to express an irrotational velocity field in terms of the gradient of a scalar function ϕ, giving finally

$$\vec{v}(x, y, z, t) = \vec{\nabla} \phi(x, y, z, t) \tag{4}$$

Equation 4 defines a velocity field that is potential.

2.2 Vortex Flow

Similar to streamlines in the velocity field, the vorticity field given by equation 2 may be considered to be composed of vector lines. A vortex line is a line in which the vorticity vector at every point is directed along a tangent of the line. Thus, a vortex line satisfies the relation

$$\frac{\Omega_x}{dx} = \frac{\Omega_y}{dy} = \frac{\Omega_z}{dz} \tag{5}$$

Another useful construct, the vortex tube, is an extension of the vortex line concept: a vortex tube is a union of vortex lines in a cylindrical form which may be thought of as a bundle of vortex lines. The circulation about a simply connected path c about a vortex tube is defined by

$$\Gamma = \oint_c \vec{v} \circ \vec{dl} \tag{6}$$

Stokes' theorem applied to equation 6 yields

$$\Gamma = \int_A \vec{\Omega} \circ \vec{ds} \tag{7}$$

with $\mathcal{A}$ being a cross-section perpendicular to the vortex tube axis. Γ may be referred to as the strength of the vortex tube. Consider now a vortex tube as the area of $\mathcal{A}$ becomes small. In such a limit, the vortex tube becomes a filament of cross sectional area σ with a vortex strength of $\Gamma = \Omega\sigma$.

A law governing vortex filament conservation, first derived by Helmholtz in 1858, may be deduced from the following vector identity,

$$\vec{\nabla} \circ (\vec{\nabla} \times \vec{v}) \equiv 0 \tag{8}$$

or equivalently,

$$\vec{\nabla} \circ \vec{\Omega} \equiv 0 \tag{9}$$

Integrating equation 9 through the volume between two endpoints of a vortex filament enclosed by the surface Σ yields, upon application of Gauss' theorem,

$$\int_{\Sigma} \vec{\Omega} \circ \vec{ds} = 0 \tag{10}$$

Since the circumferential surface of a vortex filament is composed entirely of vector lines, $\vec{\Omega} \circ \vec{ds} = 0$ everywhere except at the endpoints. Thus, surface integral 10 reduces to

$$\Omega_1\sigma_1 = \Omega_2\sigma_2 \tag{11}$$

which simply states that the intensity of a vortex filament must be constant along the length of the filament. Helmholtz further established a theorem governing the conservation of vortex lines, which states:

> Assuming an ideal (i.e. inviscid) barotropic [4] fluid, with a body force having a potential, the fluid particles which at a certain instant of time form a vortex line will form a vortex line at all times of the motion [5]

A very similar result, known as Thompson's theorem may be represented by the following equation under the same assumptions

$$\frac{D}{Dt} \oint_c \vec{v} \circ \vec{dl} = 0 \tag{12}$$

where differentiation is taken following a set of fluid particles. Thus, circulation about the moving path c is constant throughout the motion. A corollary of Thompson's theorem, known as Lagrange's theorem, states the following:

---

[4] a fluid in which the density is a function of pressure alone is said to be barotropic

[5] N.E. Kochin et al, *Theoretical Hydromechanics* (New York:John Wiley, 1964), p. 155

> If at the initial instant of time there are no vortices in a certain part of the fluid, this part of the fluid did not contain any vortices in the past and will not contain any vortices in the future [6]

Consequently, one may consider vorticity to be transported through the fluid as if it were physically attached to individual fluid particles.

2.2.1 The Biot-Savart Law

The equation of mass conservation for incompressible flow may be written in the vector form

$$\vec{\nabla} \circ \vec{v} = 0 \tag{13}$$

which when coupled with vector identity 8 guarantees the existence of a function $\vec{A}$ such that

$$\vec{v} = \vec{\nabla} \times \vec{A} \tag{14}$$

Equation 2 then becomes

$$\vec{\Omega} = \vec{\nabla} \times (\vec{\nabla} \times \vec{A}) \tag{15}$$

which is transformed by a vector identity to become

$$\vec{\Omega} = \vec{\nabla}(\vec{\nabla} \circ \vec{A}) - \nabla^2 \vec{A} \tag{16}$$

Without loss of generality [7] , $\vec{A}$ can be chosen such that $\vec{\nabla} \circ \vec{A} = 0$. Then, the vector potential function $\vec{A}$ satisfies Poisson's equation,

$$\nabla^2 \vec{A} = -\vec{\Omega} \tag{17}$$

It can be shown [8] that the following volume integral is a particular solution of equation 17

$$\vec{A} = \frac{1}{4\pi} \int \frac{\vec{\Omega}(\xi, \eta, \zeta)}{r} d\tau \tag{18}$$

where (ξ, η, ζ) are cartesian coordinates of the differential volume element $d\tau$ within the vortex field. If the spatial distribution of vorticity is that of a vortex filament, then one may express the vorticity vector as the product

[6] ibid., p. 154
[7] N.E. Kochin et al, *op. cit.*, p. 188
[8] ibid.

of a magnitude and unit tangent at every point of the filament; and, the differential volume element becomes $d\tau = \sigma dl$. Equation 18 then gives the line integral,

$$\vec{A} = \frac{\left|\vec{\Omega}\right|\sigma}{4\pi} \int \frac{1}{r} \left[\frac{d\xi}{dl}\vec{i} + \frac{d\eta}{dl}\vec{j} + \frac{d\zeta}{dl}\vec{k} \right] dl \tag{19}$$

If (x, y, z) is the coordinate of the point at which the induction of the vortex system is to be evaluated, then

$$r = \left[(\xi - x)^2 + (\eta - y)^2 + (\zeta - z)^2 \right]^{\frac{1}{2}} \tag{20}$$

Substituting equations 19 and 20 into equation 14 while noting that $\left|\vec{\Omega}\right| \sigma = \Gamma$ finally yields the Biot Savart law for the induction of a vortex filament:

$$\vec{v}(x, y, z) = \frac{\Gamma}{4\pi} \int \frac{\vec{r} \times \vec{dl}}{r^3} \tag{21}$$

2.2.2 The Formation of Vortices

A wake of vorticity is generated by a propeller as it progresses through fluid regions which were previously irrotational . In light of Lagrange's theorem, however, parts of the fluid that at one time were irrotational cannot contain vortices at any other instant in time: the assumption of ideal fluid flow precludes the creation of a trailing vortex system. This paradox is resolved by the realization that the formation of vorticity is a consequence of non-ideal fluid behavior; and, an ideal fluid formulation is constructed to model this result.

The viscosity of a real fluid results in a no-slip condition for the flow at the surface of each propeller blade i.e. the fluid in contact with the propeller blade must move with the blade. Consequently, vorticity is generated at the blade surfaces, and is subsequently shed downstream. Hence, the production of thrust and the formation of a trailing wake are ultimately consequences of viscosity.

An ideal fluid flow model of the propeller is described in section 2.3.

2.3 Propeller Model

As a propeller moves through a fluid with forward speed V and angular speed ω, the lift distribution generated along each propeller blade is modelled by a radial distribution of 'bound' circulation in an ideal fluid. In

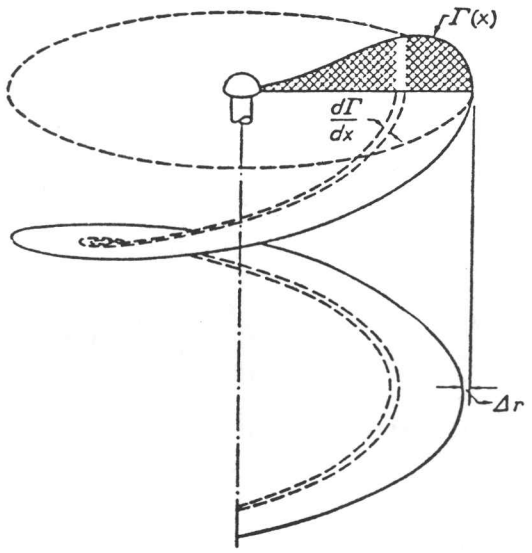

Figure 1: Circulation Along A Blade with Shed Wake

accordance with the vortex intensity conservation theorem (equation 11), changes in bound circulation can only be accomplished by the addition of vorticity from vortex filaments extending to infinity. The propeller wake is modelled by a continuous distribution of such vortex filaments which constitute helical vortex sheets of infinite length. These vortex sheets float freely within the surrounding potential flow field as massless, infinitely flexible and impenetrable entities. Continuity ensures that the flow component normal to a vortex sheet must be the same on both sides. In contrast, tangential flow components are different on opposite sides: the discontinuous jump in tangential flow velocity is a direct measure of the local intensity of the vortex sheet.

As a direct consequence of vortex conservation, the radial distribution of circulation at the propeller is the same as the distribution of circulation in the far wake. Theodorsen maps the distribution along the propeller $\Gamma(r/R)$ to an unaltered distribution $\Gamma(r/R_\infty)$ far downstream ($R_\infty < R$) i.e the circulation at radius r in the far wake is identical to the circulation at an associated point $r + \delta r$ at the propeller.

The detailed design of the propeller (i.e. pitch, chord distribution and airfoil selection) is of no concern for the purpose of ideal performance calculations: the propeller is regarded purely as a device that produces a set of helical vortex sheets which extend infinitely far downstream and which possess a certain distribution of circulation. The conservation laws of energy, momentum, and vorticity are sufficient to relate the kinetic energy, potential energy, momentum and vorticity of the wake to the thrust, torque, efficiency and bound circulation of the optimum propeller.

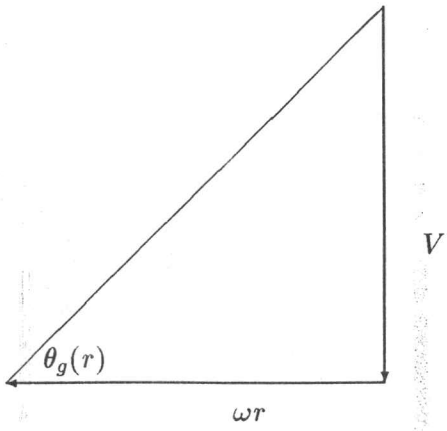

Figure 2: Relative flow for non-thrusting propeller

2.4 The Betz Condition

As stated earlier, Betz proved that minimum induced loss results when the shed vortex system forms a helical surface which, by its self-induced motion, appears to move as if rigid. It is, however, not obvious why this must be the case. To reinterpret Betz's theorem, consider an infinitesimal variation of the wake vorticity distribution by introducing an imaginary second propeller located infinitely far downstream of the first propeller with its blades tracing a path nearly coincident with the preceding wake helicoid. As the first propeller moves through the fluid with forward speed V and angular speed ω, the trailing edge of each blade will trace out a path known as the advance helicoid. The geometric pitch of the advance helicoid (a constant) is related to its pitch angle distribution $\theta_g(r)$ (see fig. 2) by

$$\mathcal{P}_g = 2\pi r \tan\theta_g(r) \tag{22}$$

Due to wake self-induction, the pitch distribution, $\mathcal{P}(r)$, of the *far wake* helicoid will differ from the geometric pitch of the propeller path,

$$\mathcal{P}(r) = 2\pi r \tan\theta(r) \tag{23}$$

Let dL denote the increment in lift at the second propeller due to the variation in circulation. Since the relative flow at the second propeller is inclined to the plane of rotation by the angle $\theta(r)$, the thrust and torque variation at r is given by

$$dT = dL\cos\theta(r) \tag{24}$$

$$dQ = rdL\sin\theta(r) \tag{25}$$

The efficiency of the differential load increment is,

$$\eta_\Delta = \frac{V\,dT}{\omega dQ} \tag{26}$$

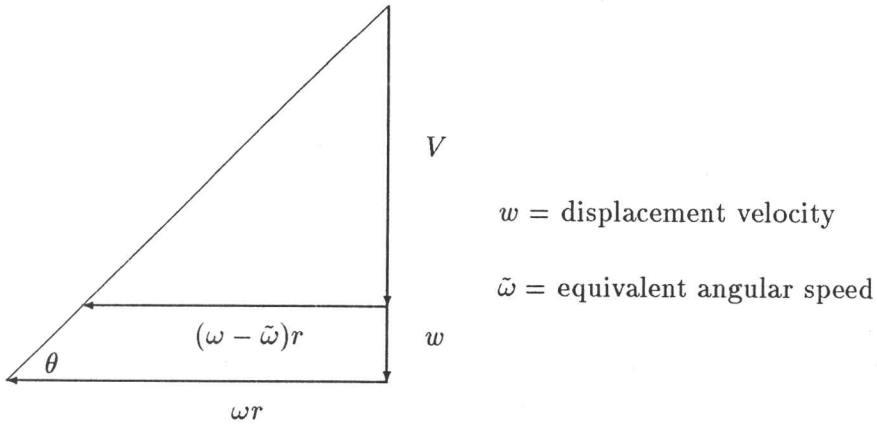

Figure 3: Equivalence of wake induction parameters

which upon substution of equations 24 and 25 plus $V/\omega r = \tan\theta_g(r)$ yields

$$\eta_\Delta = \frac{\tan\theta_g(r)}{\tan\theta(r)} \tag{27}$$

From equation 22 and 23, the efficiency is finally given by

$$\eta_\Delta = \frac{\mathcal{P}_g}{\mathcal{P}(r)} \tag{28}$$

Therefore, the efficiency of the differential element of loading is simply given by the pitch ratio of the advance helicoid to the wake helicoid far dowstream of the first propeller. If the pitch of the wake spiral changes with radius, then it would be possible to vary the circulation distribution to reduce power while maintaining constant thrust. This can be accomplished by the addition of differential thrust elements in regions of higher efficiency while decreasing the thrust by equal amounts in regions of lower efficiency; but, further reductions in power cannot be achieved once the pitch distribution is constant. With a constant far wake pitch, any further variation in the circulation distribution at constant total thrust will cause no change in the total power input. Therefore, a stationary value is achieved for the total propeller efficiency; and, the wake will appear as a rigid screw surface.

2.5 The Displacement Velocity

The displacement velocity represents the self-induced axial motion of a helical surface moving with speed w. Equivalently, the induced motion may be regarded as purely rotational with angular speed $\tilde{\omega}$. This motion equivalence is strictly a consequence of the helical geometry. The relation between these quantities can be seen by the velocity diagram in the propeller frame of reference (fig. 3):

$$\frac{V+w}{\omega r} = \frac{V}{(\omega-\tilde{\omega})r} \tag{29}$$

For a system of vortices to move as if rigid (i.e. non-distorting), the displacement velocity, w, must be independent of wake radius. Note, however, that *the displacement velocity is not the fluid velocity.*

The far wake pitch, P_∞, is nondimensionalized by the wake circumference $2\pi R_\infty$. The *generalized wake advance coefficient* thus derived is equivalent to the tangent of the tip helix angle infinitely far downstream of the propeller i.e.,

$$\lambda_t \equiv \frac{P_\infty}{2\pi R_\infty} = \tan\theta_{tip} \tag{30}$$

Expressed in terms of velocity parameters, this is equivalent to

$$\lambda_t = \frac{V}{\omega R_\infty}(1+\bar{w}) \tag{31}$$

where $\bar{w} \equiv w/V$ is the dimensionless displacement velocity. The coefficient defined by

$$\lambda = \frac{V}{\omega R_\infty} \tag{32}$$

is used as an approximation to the propeller advance coefficient $\lambda_p = V/\omega R$ where R is the propeller radius.

2.5.1 Example: Optimum Circulation Distribution For A Propeller Having An Infinite Number of Blades

The following is an example illustrating the application of the Betz condition to obtain the ideal circulation distribution for a propeller having an infinite number of blades. If the pitch of the far wake helicoid is P_∞, then the distance between adjacent vortex sheets for a propeller with B blades is then $l = P_\infty/B$. Thus the system of vortex sheets is more tightly packed over one turn of the helicoid as the number of blades increase. For non-zero l, there exists a radial flow component around the edges of each vortex sheet in addition to the axial and rotational flow components. However, $l \to 0$ as $B \to \infty$ which results in the degree of radial flow approaching zero; and, the fluid column receives the full effect of the vortex system motion. Therefore, the velocity field everywhere within the slipstream corresponds exactly to the motion of the vortex sheets [9]. The induced flow is locally normal to the vortex sheet; hence, the induced velocity is given by the component of w on the unit surface normal:

$$v_n = w \cos\theta(r) \tag{33}$$

and, the corresponding fluid velocity components (axial and tangential) are:

$$v_z = w \cos^2\theta(r) \tag{34}$$

and,

$$v_t = w \cos\theta(r) \sin\theta(r) \tag{35}$$

The total circulation shed from B blades into the slipstream will be equal to the contour integral at r,

$$B\Gamma = \oint_c \vec{v} \circ \vec{dl} \tag{36}$$

where c is a contour of radius r coaxial with the wake vortex system taken about a plane perpendicular to the axis of symmetry. As $B \to \infty$, the velocity field within the slipstream becomes independent of z and θ. Consequently,

$$\begin{aligned} B\Gamma &= 2\pi r v_t & (37)\\ &= 2\pi r w \cos\theta(r) \sin\theta(r) & (38) \end{aligned}$$

[9] this is also the case for propellers of finite blade number as $\lambda_t \to 0$

The wake advance coefficient, defined by equation 30 is used in conjunction with the relations

$$\cos\theta(r) = \frac{\omega r}{\sqrt{(\omega r)^2 + (V+w)^2}} \tag{39}$$

$$\sin\theta(r) = \frac{V+w}{\sqrt{(\omega r)^2 + (V+w)^2}} \tag{40}$$

to express 38 in the form

$$B\Gamma(r) = 2\pi r w \frac{(r/R_\infty)\cdot\lambda_t}{(r/R_\infty)^2 + \lambda_t^2} \tag{41}$$

But, the circulation function may be non-dimensionalized by the following,

$$\Gamma(r) = lwK(r) \tag{42}$$

$$= \frac{P_\infty}{B} wK(r) \tag{43}$$

$$= \frac{2\pi R_\infty \lambda_t}{B} wK(r) \tag{44}$$

Substituting 44 into 41 yields the optimum circulation distribution,

$$K(\frac{r}{R_\infty}) = \frac{(r/R_\infty)^2}{(r/R_\infty)^2 + \lambda_t^2} \tag{45}$$

3 Theodorsen's Formulation

Theodorsen introduced a general theory based on optimum circulation functions to describe ideal propeller behavior. Goldstein's solutions for optimum circulation functions were originally thought to apply only for lightly loaded propellers. However, Theodorsen introduced the generalization that Goldstein functions need not be limited to light loadings if reference is made to the ultimate helix surface infinitely far downstream of the propeller. For example, the optimum circulation function of a heavily loaded propeller is the same as that of a lightly loaded propeller operating at a higher geometric advance since they can produce identical far wake helicoids: the geometry of the far wake governs the non-dimensional circulation function which is independent of loading. If the problem is cast in terms of the far-wake advance coefficient (equation 30), instead of the advance coefficient (equation 32), then the restriction to light propeller loadings is eliminated. If

the degree of wake contraction is small, then the displacement velocity w is sufficient to relate the wake advance coefficient to the propeller advance for most purposes (see section 7). Theodorsen's formalism is cast in terms of the initially unknown displacement velocity and parameters describing the far wake; hence, an iteration procedure is required to relate conditions in the far wake to corresponding values at the propeller. This approach represents somewhat of a reversal of design procedure: the design of the propeller is not considered, except as the final step in the design process.

3.1 The Mass Coefficient

The mass coefficient is defined by the relation

$$\kappa \equiv \frac{\int_{\mathcal{F}} v_z ds}{wA} \tag{46}$$

where the integral is evaluated over the helicoid cross section and out to $r = \infty$. Since the circumferential average of v_z is zero for $r > R_\infty$, this represents the average axial velocity over the helicoid cross section F of area $A = \pi R_\infty^2$. Equation 46 applies to any wake section far back; thus, an axial average over a distance l of the righthand side does not alter the value of κ:

$$\kappa = \frac{\rho \int_0^l dz \int_{\mathcal{F}} v_z ds}{\rho l w A} \tag{47}$$

$$= \frac{m_z}{\rho l w A} \tag{48}$$

Here m_z is the axial momentum of the fluid contained in a wake cylinder of height $l = P_\infty / B$ where l is the axial separation between adjacent vortex sheets.

Since the potential ϕ is constant along a helical path of pitch P_∞, the difference in potential between adjacent vortex sheets is equal to the jump in potential across one sheet which is equivalent to Γ. Upon interchanging the order of integration, the numerator of equation 47 becomes

$$m_z = \rho \int \int_{\mathcal{F}} \frac{\partial \phi}{\partial z} dz ds \tag{49}$$

$$= \rho \int_{\mathcal{F}} \Gamma ds \tag{50}$$

This is non-dimensionalized by

$$\Gamma = wlK \tag{51}$$

$$ds = rdrd\theta \quad (52)$$

$$= R_\infty^2 xdxd\theta \quad (53)$$

to give

$$m_z = \rho wAl \cdot 2\int_0^1 K(x)xdx \quad (54)$$

From equation 48, this leads to the important result

$$\kappa = 2\int_0^1 K(x)xdx \quad (55)$$

The mass coefficient, one of the most fundamental parameters in Theodorsen's theoretical formulation, may be interpreted as the ratio of an effective wake cross section (based on axial momentum) to the wake area A. It can be seen from equation 48 that the vortex system may be considered to impart a uniform axial velocity w to a fluid column of cross sectional area κA.

3.2 Equation of Motion

The velocity potential characterizing the motion of the far wake is time dependent; and, it is governed by the unsteady Bernoulli equation,

$$\frac{\partial\phi}{\partial t} + \frac{1}{2}v^2 + \frac{p}{\rho} = const. \quad (56)$$

Because of helical geometry, $\frac{\partial\phi}{\partial t}$ can be expressed in terms of flow velocities. As detailed earlier, the slipstream field pattern may be considered to move with a uniform axial velocity w. Thus the velocity potential has the functional form,

$$\phi = \phi(r,\theta,z-wt) \quad (57)$$

from which the following may be derived,

$$\frac{\partial\phi}{\partial t} = -wv_z \quad (58)$$

Far away from the wake axis $\frac{\partial\phi}{\partial t} \to 0, v^2 \to 0$; hence, the constant of equation 56 approaches p_0/ρ. Equation 56 finally becomes,

$$(p-p_0) + \frac{1}{2}\rho v^2 = \rho wv_z \quad (59)$$

3.3 Thrust, Power and Efficiency

Ideal propeller thrust, power and efficiency are determined exclusively from conditions in the ultimate wake. Conservation laws of momentum and energy are applied to a control volume of infinite extent surrounding the far wake to obtain the desired relation. Conservation of momentum leads to the expression

$$T = \int_{\Pi}[(p - p_0) + \rho(V + v_z)v_z]ds \tag{60}$$

where Π is an infinite plane perpendicular to the propeller axis, located infinitely far downstream (i.e. the Trefftz plane). Similarly, conservation of energy results in the following expression for the power lost to the wake,

$$\frac{dE}{dt} = \int_{\Pi}[(p - p_0 + \frac{1}{2}\rho v^2)v_z + \frac{1}{2}\rho v^2 V]ds \tag{61}$$

The pressure term, $(p-p_0)$, in equations 60 and 61 is an important feature of the theoretical formulation. In contrast to the actuator disc, Theodorsen's model permits the existence of a wake pressure exceeding ambient conditions (see section 3.4). Substituting equation 59 into 60 - 61 yields

$$T = \rho \int_{\Pi}[(V + w)v_z + v_z^2 - \frac{1}{2}v^2]ds \tag{62}$$

and

$$\frac{dE}{dt} = \rho \int_{\Pi}(wv_z^2 + \frac{1}{2}Vv^2)ds \tag{63}$$

Equations 62 and 63 can be expressed in terms of physically significant integrated parameters; these being the mass coefficient and the axial kinetic energy loss coefficient. In addition to the earlier description of the mass coefficient, this parameter may also be interpreted as the total kinetic energy loss coefficient (see Appendix A). Secondly, the axial kinetic energy loss coefficient, defined by

$$\frac{1}{2}\rho \int_{\Pi} v_z^2 ds \equiv \epsilon[\frac{1}{2}\rho A w^2] \tag{64}$$

may be thought of as a factor which relates the wake area, $A = \pi R_\infty^2$, to an effective cross section (in terms of axial kinetic energy), ϵA, upon which the vortex system may be considered to impart a pure axial velocity equal to

the displacement velocity. Equations 62 and 63 are now expressed in terms of the coefficients κ and ϵ:

$$T = \rho\kappa w A[V + w(\frac{1}{2} + \frac{\epsilon}{\kappa})] \tag{65}$$

$$\frac{dE}{dt} = \rho\kappa w^2 A[\frac{\epsilon}{\kappa}w + \frac{1}{2}V] \tag{66}$$

The total power input required by the ideal propeller must equal the sum of the useful power and induced power,

$$P = TV + \frac{dE}{dt} = \rho\kappa w A(V + w)(V + w\frac{\epsilon}{\kappa}) \tag{67}$$

In nondimensional coefficient form, thrust and power equations 65 and 67 become

$$\begin{aligned} c_s &= \frac{T}{\frac{1}{2}\rho V^2 A} \\ &= 2\kappa\bar{w}[1 + \bar{w}(\frac{1}{2} + \frac{\epsilon}{\kappa})] \end{aligned} \tag{68}$$

$$\begin{aligned} c_p &= \frac{P}{\frac{1}{2}\rho V^3 A} \\ &= 2\kappa\bar{w}(1 + \bar{w})(1 + \bar{w}\frac{\epsilon}{\kappa}) \end{aligned} \tag{69}$$

where $\bar{w} \equiv w/V$. For further information, one could refer to the development of the above equations in Theodorsen [10]; but, a more detailed derivation has been provided in appendix A.

The efficiency is defined by the ratio

$$\eta = \frac{c_s}{c_p} \tag{70}$$

Thus from equations 68 and 69 one obtains

$$\eta = \frac{1 + \bar{w}(\frac{1}{2} + \frac{\epsilon}{\kappa})}{(1 + \bar{w})(1 + \bar{w}\frac{\epsilon}{\kappa})} \tag{71}$$

[10] Theodorsen, *op. cit.*, pp. 23-29

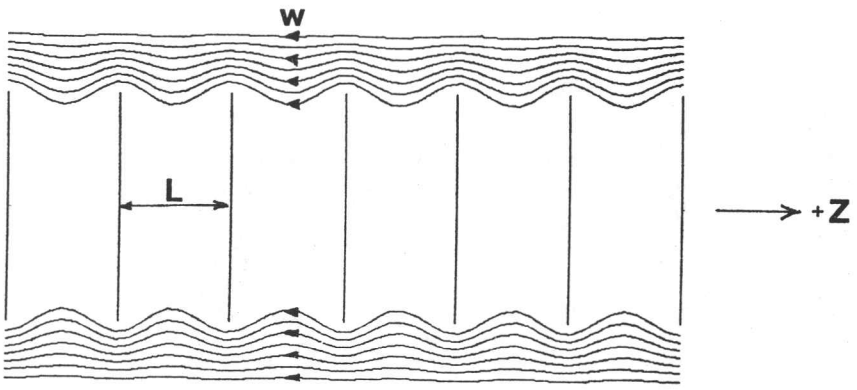

Figure 4: Flow about an axially moving cascade (cascade frame of reference)

The connection between the axial and total kinetic energy factors is, from Theodorsen [11]

$$\epsilon = \kappa + \frac{1}{2}\lambda_t \frac{d\kappa}{d\lambda_t} \tag{72}$$

This relation was derived by equating the efficiency of a differential element of loading to the functions c_s and c_p:

$$\frac{c_s'}{c_p'} = \frac{1}{1+\bar{w}} \tag{73}$$

where differentiation with respect to $\bar{w}$ is denoted by primes.

3.4 Wake Overpressure

A physical basis for overpressure within the wake can be explored by considering flow within boundary regions of the wake produced by a finite number of blades. If the wake is approximated by a cascade of planar lamina moving axially with speed w, then the flow field has the illustrated form (fig. 4). The approximation represented by figure 4 is that employed by Prandtl in his estimate of the losses represented by the consequent flow in the edge regions [12]. This model, for which analytic solutions exist, serves to illustrate the curvature of the streamlines between vortex sheets. The centripetal acceleration of the edge flow between sheets must be accompanied by an inwardly directed pressure gradient; thus, higher pressures result within the

[11] ibid., p. 35

[12] W.F. Durand, *Aerodynamic Theory*, Vol. iv, 1935, pp. 261-267

wake. Strictly speaking, the above flow depiction is truly representative for small values of advance; nonetheless, the above model generally characterizes the situation that occurs near the outer regions of the wake for finite blade numbers. Wake overpressure represents an additional mechanism for the loss of energy to the slipstream. Theodorsen's model then accounts for a total of four loss mechanisms: axial kinetic energy loss, swirl loss (rotational kinetic energy), radial flow kinetic energy loss and energy loss due to wake overpressure ($p - p_0 > 0$).

4 Asymptotic Results

Analysis of the various limit cases lend insights to propeller behavior and provide a valuable means for verification of computational algorithms (section 5). This section examines the properties of ideal propellers in the limit of both large and small advance coefficients.

4.1 Limit Case: $\lambda_t \to 0$

Upon the examination of helicoid geometry, some physical insights into propeller behavior can be realized in the limit $\lambda_t \to 0$. One can consider this case to arise when the flight speed of a propeller approaches zero. As the pitch of each helicoidal vortex sheet becomes small, the distance between adjacent vortex sheets is also reduced. The reduction in vortex spacing extends the region within the wake for which radial flow is negligible; thus, the magnitude of tip loss is diminished with λ_t. In this sense the ideal circulation function for a propeller having a finite number of blades approaches the distribution for an infinite blade propeller at the same generalized advance coefficient λ_t. A further consequence of reduced pitch is that the pitch angle distribution along each sheet is diminished according to the relation

$$\theta(r) = \arctan \frac{\lambda_t}{(r/R_\infty)} \tag{74}$$

Since the fluid becomes *trapped* between vortex sheets for small λ_t, the fluid velocity field approaches the velocity of the vortex system. Thus, the gradient $v = \partial\phi/\partial n$ ($\vec{n}$ is normal to the vortex surface) more closely represents the slipstream velocity field. In accordance with equation 74, the magnitude of slipstream rotation is diminished with λ_t because $\vec{n}$ becomes more aligned with the propeller axis as the pitch approaches zero; thus, axial flow dominates throughout the wake. The influence on the mass coefficient is clear: as the flow becomes purely axial, the real flow velocity approaches the displacement velocity which causes the effective wake cross section, based on axial momentum, to approach the wake area. Hence, the mass coefficient approaches unity as $\lambda_t \to 0$. Likewise, the effective cross section based on axial kinetic energy will approach the wake area resulting in $\epsilon \to 1$. Applying these deductions to equations 68, 69 and 71 yields

$$\lim_{\lambda_t \to 0} c_s = 2\bar{w}(1 + \frac{3}{2}\bar{w}) \tag{75}$$

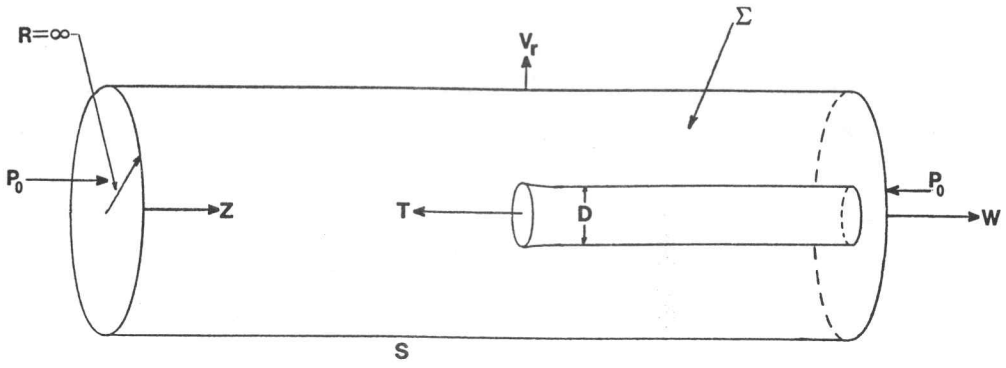

Figure 5: Infinite Control Volume Containing Actuator Disc and Wake

$$\lim_{\lambda_t \to 0} c_p = 2\bar{w}(1+\bar{w})^2 \tag{76}$$

$$\lim_{\lambda_t \to 0} \eta = \frac{1+\frac{3}{2}\bar{w}}{(1+\bar{w})^2} \tag{77}$$

Note that these relations are independent of blade number.

4.1.1 Comparison with the Actuator Disc Model

Herein the equations of thrust,power and efficiency for the actuator disc model are derived by applying conservation laws to a control volume that is stationary with respect to the far field and which encloses the disc and wake (Fig. 5).

Conservation of axial momentum yields,

$$\frac{\partial}{\partial t}\int_\Sigma \rho v_z d\tau + \int_S \rho v_z < \vec{v} \circ \vec{n} > ds = T - \int_S p < \vec{n} \circ \vec{k} > ds \tag{78}$$

Since the pressure is everywhere equal to ambient pressure p_0,

$$\int_S p < \vec{n} \circ \vec{k} > ds = 0 \tag{79}$$

The rate of increase in axial momentum within the control volume due to the rate of elongation of the wake,

$$\frac{\partial}{\partial t}\int_S \rho v_z d\tau = \rho w V A \tag{80}$$

and, the net momentum flux across the control surface

$$\int_S \rho v_z < \vec{v} \circ \vec{n} > ds = \rho w^2 A \tag{81}$$

yield, upon substitution into equation 78, an expression for the total thrust,

$$T = \rho w A(V + w) \tag{82}$$

or, in coefficient form based on the area of the far wake, $A = \pi R_\infty^2$,

$$c_{s,a} = 2\bar{w}(1 + \bar{w}) \tag{83}$$

The following equation represents the principle of energy conservation applied to the same control volume,

$$\frac{\partial}{\partial t}\int_\Sigma \frac{1}{2}\rho v^2 d\tau + \int_S \frac{1}{2}\rho v^2 < \vec{v} \circ \vec{n} > ds = \frac{dE}{dt} - \int_S p < \vec{v} \circ \vec{n} > ds \tag{84}$$

where $\frac{dE}{dt}$ is the rate of energy loss to the slipstream. Evaluating each term in the above equation, in accordance with the actuator disc model, gives an expression for the energy loss rate,

$$\frac{dE}{dt} = \frac{1}{2}\rho w^2 A(V + w) \tag{85}$$

or

$$c_{e,a} = \bar{w}^2(1 + \bar{w}) \tag{86}$$

Then, the total power, $P = TV + dE/dt$, is given in coefficient form by

$$c_{p,a} = c_{s,a} + c_{e,a} = \bar{w}(1 + \bar{w})(2 + \bar{w}) \tag{87}$$

to give the efficiency

$$\eta_a = \frac{c_{s,a}}{c_{p,a}} = \frac{1}{1 + \frac{1}{2}\bar{w}} \tag{88}$$

The initial expectation is that the actuator disc model should agree with the limit case $\lambda_t \to 0$ of Theodorsen's equations. However, a comparison of equations 83, 87 and 88 with the asymptotic relations 77 belie intuitive expectation. This is consistent with Theodorsen's assertion that the actuator disc model is not a true limit of the propeller as $\lambda_t \to 0$ [13].

To reconcile the differences between the two formulations, Theodosen's pressure integral can be evaluated separately in the limit $\lambda_t \to 0$. The contribution of wake overpressure to the thrust expression is then

$$\hat{T} = \int (p - p_0) ds \tag{89}$$

[13] T. Theodorsen, *Theory of Propellers* (New York:McGraw-Hill,1948), p. 31

but, substitution of equation 59 into equation 89 gives

$$\hat{T} = \rho \int (wv_z - \frac{1}{2}v^2)ds \tag{90}$$

Evaluating 90 in the limit $\lambda_t \to 0$ yields

$$\hat{T} = \rho \frac{1}{2} w^2 A \tag{91}$$

or,

$$\hat{c}_s = \bar{w}^2 \tag{92}$$

Similarly, the contribution of the pressure term to the energy equation is then

$$\begin{aligned} \frac{dE}{dt} &= \int (p - p_0) v_z ds \\ &= \rho \int (wv_z^2 - \frac{1}{2}v^2 v_z) ds \end{aligned} \tag{93}$$

In the limit as $\lambda_t \to 0$, equation 93 becomes

$$\frac{dE}{dt} = \rho(\frac{1}{2}w^3)A \tag{94}$$

or, in coefficient form

$$\hat{c}_e = \bar{w}^3 \tag{95}$$

and

$$\hat{c}_p = \bar{w}^2 + \bar{w}^3 \tag{96}$$

Subtracting 92 and 96 from equations 77 yield expressions without the contribution of wake overpressure in the limit of small λ_t:

$$\begin{aligned} c_s &= 2\bar{w}(1 + \frac{3}{2}\bar{w}) - \bar{w}^2 \\ &= 2\bar{w}(1 + \bar{w}) \end{aligned} \tag{97}$$

$$\begin{aligned} c_p &= 2\bar{w}(1 + \bar{w})^2 - (\bar{w}^2 + \bar{w}^3) \\ &= \bar{w}(1 + \bar{w})(2 + \bar{w}) \end{aligned} \tag{98}$$

The above equations are precisely the same relations derived from actuator disc theory . Therefore, the difference between actuator disc theory and the limit case $\lambda_t \to 0$ of Theodorsen's equations lies in the absence of the pressure integral $\int (p - p_0) ds$.

4.2 Limit Case: $B \to \infty$

As shown in section 2.5.1, the Betz condition governs the optimum circulation distribution as the blade number approaches infinity resulting in the exact solution,

$$K(x) = \frac{x^2}{x^2 + \lambda_t^2} \tag{99}$$

where $x \equiv r/R_\infty$. Analytic solutions for the loss coefficients are readily obtained by substituting the ideal circulation distribution 99 into equation 54. Theodorsen gives,

$$\kappa(\lambda_t) = 1 - \lambda_t^2 \ln(1 + 1/\lambda_t^2) \tag{100}$$

$$\epsilon(\lambda_t) = 1 + \frac{\lambda_t^2}{1 + \lambda_t^2} - 2\lambda_t^2 \ln(1 + 1/\lambda_t^2) \tag{101}$$

As the blade number approaches infinity, the distance between adjacent vortex sheet approaches zero for an arbitrary advance coefficient. Consequently, radial flow becomes non-existent throughout the slipstream; but, in constrast with the limit of small advance coefficients, swirl loss is maintained for all $\lambda_t > 0$.

4.3 Limit Case: $\lambda_t \to \infty$

As shown in section 2.5, the helicoidal vortex system can be characterized by either an equivalent axial velocity w or an equivalent angular veolcity $\tilde{\omega}$. The helix angle may then be represented by one of the following,

$$\tan\theta(r) = \frac{P_\infty}{2\pi r} = \frac{V + w}{\omega r} = \frac{V}{(\omega - \tilde{\omega})r} = \frac{\lambda_t}{r/R_\infty} \tag{102}$$

For large advance coefficients, the helicoid may be considered to be a ribbon-like structure of width $2R_\infty$ rotating with an angular velocity $\tilde{\omega}$. Ribner [14] examined such a case for which it was shown that the kinetic energy per unit length of the wake of a two blade propeller at large advance coefficients approaches the value

$$\mathcal{E} = \frac{\pi}{16}\rho\tilde{\omega}^2 R_\infty^4 \tag{103}$$

[14] H.S. Ribner, 'A Transonic Propeller of Triangular Plan Form', NACA TN 1303, 1947.

B	$Q_\infty^{(B)}/Q_\infty^{(2)}$
2	1
3	1.35
4	1.621
6	2.03
8	2.33

Table 1: Propeller Torque Ratios for Infinitely Large Advance Coefficients

However, another expression can be derived from Theodorsen's formalism

$$\mathcal{E} = \kappa(\lambda_t; B) \cdot \frac{1}{2}\rho w^2 \pi R_\infty^2 \tag{104}$$

where $\kappa(\lambda_t; B)$ denotes the total kinetic energy loss factor (or mass coefficient) of a B-blade propeller. Equating relations 103 and 104 generates an expression for the mass coefficient of a 2-blade propeller,

$$\kappa(\lambda_t; B = 2) \overset{\lambda_t >> 1}{\longrightarrow} \frac{1}{8\lambda_t^2} \tag{105}$$

Ribner further demonstrated that torque, $Q_\infty^{(B)}$, scales with kinetic energy per unit length of the ultimate wake for large λ_t . It then follows from 104

$$\frac{\kappa(\lambda_t; B = 2)}{\kappa(\lambda_t; B)} \rightarrow \frac{Q_\infty^{(2)}}{Q_\infty^{(B)}} \tag{106}$$

so that

$$\kappa(\lambda_t; B) \rightarrow \frac{Q_\infty^{(B)}}{8\lambda_t^2 Q_\infty^{(2)}} \tag{107}$$

where the torque ratios [15] are given by table 1. From the definition of the axial kinetic energy loss coefficient (eqn. 72), it can be easily shown that $\epsilon/\kappa \rightarrow 0$ for $\lambda_t >> 1$. Consequently, equations 68, 69 and 71 with the substitution $\lambda_t = (1 + \bar{w})\lambda$ become in the limit

$$c_s = \frac{Q_\infty^{(B)}}{Q_\infty^{(2)}} \cdot \frac{\bar{w}(1 + \frac{1}{2}\bar{w})}{4\lambda^2(1 + \bar{w})^2} \tag{108}$$

[15] H.S. Ribner, 'Damping in Roll of Cruciform and Some Related Delta Wings at Supersonic Speeds', NACA TN 2285, 1951.

$$c_p = \frac{Q_\infty^{(B)}}{Q_\infty^{(2)}} \cdot \frac{\bar{w}}{4\lambda^2(1+\bar{w})}$$

$$\eta = \frac{1+\frac{1}{2}\bar{w}}{(1+\bar{w})}$$

The displacement velocity may be expressed in terms of the ideal efficiency

$$\bar{w} = \frac{2(1-\eta)}{2\eta - 1} \tag{109}$$

so the equations 108 are expressed in terms of the ideal propeller efficiency

$$c_s = \frac{Q_\infty^{(B)}}{Q_\infty^{(2)}} \cdot \frac{\eta(1-\eta)}{2\lambda^2} \tag{110}$$

$$c_p = \frac{Q_\infty^{(B)}}{Q_\infty^{(2)}} \cdot \frac{(1-\eta)}{2\lambda^2} \tag{111}$$

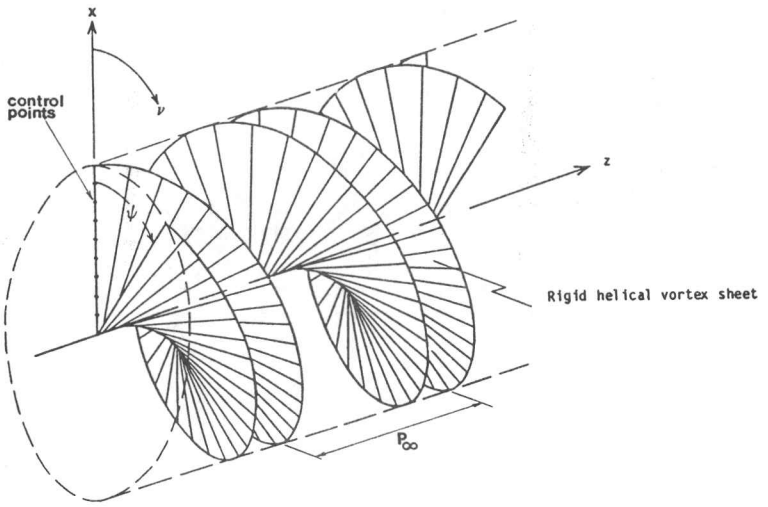

Figure 6: Coordinate System of the Computational Domain

5 Numerical Algorithms

Following Theodorsen's approach, only the properties of the far wake, characterized by the generalized advance coefficient, are considered in the evaluation of ideal propeller behavior. Within the far wake there exists a certain distribution of circulation $\Gamma(\frac{r}{R_\infty})$ for which the self induced motion results in minimum induced energy loss. The following discussion describes the computational algorithms employed to calculate optimum circulation distributions and the associated parameters derived therefrom.

Betz's theorem stipulates the condition necessary for a propeller to operate at maximum ideal efficiency (section 2.4). In short, the Betz condition requires that the vortex sheets move as if rigid, which is equivalent to requiring the apparent axial velocity w to be independent of radius.

Approximate solutions for the ideal circulation function are obtained by discretizing each helical vortex surface of constant pitch into a finite number of helical vortex filaments. The induction of the vortex system is calculated at specified control points by means of computed influence coefficients and unknown filament intensities. In this way, the Betz condition is manifest as a linear system of equations in terms of unknown filament strengths.

A cartesian coordinate system is constructed with the x axis coincident with one vortex sheet and the z coordinate direction forming the wake axis. The y axis then completes the right hand coordinate system. The situation is shown by fig. 6. By virtue of skewsymmetry, the displacement velocity at one end of the semi-infinite wake extending from $z = 0$ to $z = +\infty$ is precisely one half of the value induced by the infinite wake. Full advantage is made of this result to minimize computational cost: only one half of the wake needs to be considered in the computation of influence coefficients. The

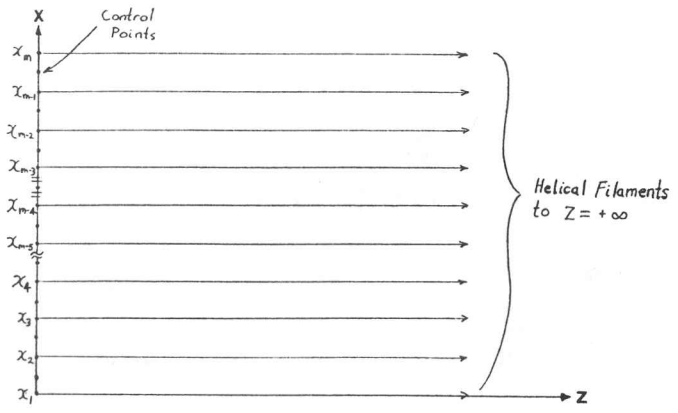

Figure 7: Control point-vortex filament positioning

xy plane may then be viewed as a cutting plane which eliminates the region $z < 0$ from consideration. The control point and vortex filament geometry is illustrated by fig. 7. Each x_i denotes a point at which a filament is severed from the upstream section of the wake. The direction of vorticity is defined as positive in the rearward sense. The radial distribution of circulation is then modelled as a summation of helical vortices of strength $\gamma_j \approx -(\frac{d\Gamma}{dx})\delta x$.

In accordance with the Betz condition, the infinite wake must induce a velocity of magnitude $w \cos\theta_i$ locally normal to the helicoid at point P_i, where θ_i is the local helix angle, and w is the unknown constant displacement velocity. Let $\vec{v}_i$ be the velocity induced by the collection of vortices of strength γ_j which approximate the infinite wake. If we further define $\vec{n}_i$ as the local normal to the vortex sheet at P_i, then to satisfy the Betz condition we must have

$$\vec{v}_i \circ \vec{n}_i = \sum_{\alpha=1}^{3} v_i^\alpha n_i^\alpha = w \cos\theta_i \tag{112}$$

with the local normal given by helicoid geometry,

$$\begin{aligned} n_i^1 &= 0 \\ n_i^2 &= -\sin\theta_i \\ n_i^3 &= \cos\theta_i \end{aligned} \tag{113}$$

The local velocity $\vec{v}_i$ results from the combined influence of all helical vortex filaments. Each velocity component of $\vec{v}_i$ may be expressed as the sum of the product of vortex strength and influence coefficient pairs over all helical

filaments

$$v_i^\alpha \equiv w \sum_{j=1}^{m} c_{ij}^\alpha \hat{\gamma}_j \tag{114}$$

where $\hat{\gamma}_j = \gamma_j / wl$. Equation 114 into 112 yields

$$\sum_{\alpha=1}^{3} (w \sum_{j=1}^{m} c_{ij}^\alpha \hat{\gamma}_j) n_i^\alpha = w \cos\theta_i \tag{115}$$

Exchanging the order of summation,

$$\sum_{j=1}^{m} \sum_{\alpha=1}^{3} c_{ij}^\alpha n_i^\alpha \hat{\gamma}_j = \cos\theta_i \tag{116}$$

and further defining the set of influence factors

$$F_{ij} \equiv \sum_{\alpha=1}^{3} c_{ij}^\alpha n_i^\alpha \tag{117}$$

finally results in the system of equations

$$\sum_{j=1}^{m} F_{ij} \hat{\gamma}_j = \cos\theta_i \quad 1 \leq i \leq m-1 \tag{118}$$

where m is the number of helical filaments per blade. With the condition of vortex continuity

$$\sum_{j=1}^{m} \hat{\gamma}_j = 0 \tag{119}$$

appended to the linear system 118, the discrete approximation to the circulation distribution is readily obtained.

5.1 Influence Coefficients

The Biot-Savart law (section 2.2.1) is used to compute the velocity induced by a line vortex. The induced velocity at point P_i due to a single helical filament of radius r_j is then

$$\vec{v}_{ij} \equiv \sum_{\alpha=1}^{3} v_{ij}^\alpha \underline{e}^\alpha$$

$$= \frac{\gamma_j}{4\pi} \int_{\Upsilon} \frac{\vec{\rho} \times \vec{dl}}{|\vec{\rho}|^3} \tag{120}$$

where $\underline{e}^{\alpha}$ = principal coordinate unit vector

Υ = helical path of radius r_j

$\vec{\rho}$ = vector from P_i to a point on Υ

However, the above equation fails to account for more than one vortex sheet (i.e. for more than one propeller blade). To account for multiple blade number it is necessary to include the induction from a set of helical filaments of the same radius with one filament associated with each blade. The induced velocity of B filaments of radius r_j at P_i becomes

$$\begin{aligned} \vec{v}_{ij} &= w\hat{\gamma}_j \sum_{\alpha=1}^{3} c_{ij}^{\alpha} \underline{e}^{\alpha} \\ &= \frac{wl\hat{\gamma}_j}{4\pi} \sum_{k=1}^{B} \int_{\Upsilon_k} \frac{\vec{\rho} \times \vec{dl}}{|\vec{\rho}|^3} \end{aligned} \tag{121}$$

where Υ_k is a vortex filament of radius r_j from blade k. Expressing the Biot-Savart integral in equation 121 in non-dimensional form gives finally

$$\sum_{\alpha=1}^{3} c_{ij}^{\alpha} \underline{e}^{\alpha} = \frac{\lambda_t}{2B} \sum_{k=1}^{B} \int_{\Upsilon_k} \frac{(\vec{\rho}/R_{\infty}) \times (\vec{dL}/R_{\infty})}{|\vec{\rho}/R_{\infty}|^3} \tag{122}$$

The cartesian coordinates of a point on the helical filament Υ_k are defined by $(\xi_j^1, \xi_j^2, \xi_j^3)$. Expressed in terms of the parameter ν, the coordinates are given by

$$\begin{aligned} \xi_j^1 &= r_j \cos(\nu + \psi_k) \\ \xi_j^2 &= r_j \sin(\nu + \psi_k) \end{aligned} \tag{123}$$

$$\xi_j^3 = \lambda_t R_{\infty} \nu \tag{124}$$

where

$$\psi_k = \frac{2\pi(k-1)}{B} \tag{125}$$

The angular separation between helical filaments originating from adjacent propeller blades is $\psi_{k+1} - \psi_k$. If the coordinates of the control point P_i are designated by $P_i = (\zeta_i^1, \zeta_i^2, \zeta_i^3)$ then the vector $\vec{\rho}$ can be expressed as

$$\vec{\rho} = (r_j \cos(\nu + \psi_k) - \zeta_i^1, r_j \sin(\nu + \psi_k) - \zeta_i^2, \lambda_t R_{\infty} \nu - \zeta_i^3) \tag{126}$$

The infinite wake influence coefficients are then given by the expansion of equation 122,

$$
\begin{aligned}
c_{ij}^1 &= \frac{\lambda_t^2}{2B}\int_{-\infty}^{\infty}\sum_{k=1}^{B}\frac{\frac{r_j}{R_\infty}\sin(\nu+\psi_k)-\frac{\zeta_i^2}{R_\infty}-\frac{r_j}{R_\infty}\cos(\nu+\psi_k)(\nu-\frac{\zeta_i^3}{\lambda_t R_\infty})}{|\vec{\rho}/R_\infty|^3}d\nu \\
c_{ij}^2 &= -\frac{\lambda_t^2}{2B}\int_{-\infty}^{\infty}\sum_{k=1}^{B}\frac{\frac{r_j}{R_\infty}\cos(\nu+\psi_k)-\frac{\zeta_i^1}{R_\infty}+\frac{r_j}{R_\infty}\sin(\nu+\psi_k)(\nu-\frac{\zeta_i^3}{\lambda_t R_\infty})}{|\vec{\rho}/R_\infty|^3}d\nu \\
c_{ij}^3 &= \frac{\lambda_t}{2B}\cdot\frac{r_j}{R_\infty}\int_{-\infty}^{\infty}\sum_{k=1}^{B}\frac{\frac{r_j}{R_\infty}-\frac{\zeta_i^1}{R_\infty}\cos(\nu+\psi_k)-\frac{\zeta_i^2}{R_\infty}\sin(\nu+\psi_k)}{|\vec{\rho}/R_\infty|^3}d\nu \qquad (127)
\end{aligned}
$$

and

$$
\begin{aligned}
\left|\frac{\vec{\rho}}{R_\infty}\right|^3 &= [(\frac{r_j}{R_\infty})^2-2(\frac{r_j}{R_\infty})\{(\frac{\zeta_i^1}{R_\infty})\cos(\nu+\psi_k)+(\frac{\zeta_i^2}{R_\infty})\sin(\nu+\psi_k)\} \\
&\quad +(\frac{\zeta_i^1}{R_\infty})^2+(\frac{\zeta_i^2}{R_\infty})^2+(\lambda_t\nu-\frac{\zeta_i^3}{R_\infty})^2]^{\frac{3}{2}} \qquad (128)
\end{aligned}
$$

However, skewsymmetry of the wake helicoid about $\pm\nu$ may be exploited to obtain

$$
\begin{aligned}
c_{ij}^1 &= 0 \\
c_{ij}^2 &= -\frac{\lambda_t^2}{B}I_2(0,\infty) \qquad (129) \\
c_{ij}^3 &= \frac{\lambda_t}{B}\cdot\frac{r_j}{R_\infty}I_3(0,\infty)
\end{aligned}
$$

where $I_2(0,\infty)$ and $I_3(0,\infty)$ represent the values of the corresponding integrals of 127 with $\nu = 0$ and $\nu = \infty$ as the bounds of integration. Since the integrands of equations 127 decay as $1/|\vec{\rho}|^3$, only the portion of the wake near the control points needs to be considered. For all practical purposes the wake may be truncated at a predetermined distance downstream. Hence, the functions $I_2(0,\infty)$ and $I_3(0,\infty)$ are approximated by $I_2(0,\tau)$ and $I_3(0,\tau)$ where τ is expressed in terms of the number of wake diameters, n, downstream of the control points

$$\tau = \frac{2n}{\lambda_t} \qquad (130)$$

Direct numerical integration is used to evaluate $I_2(0,\tau)$ and $I_3(0,\tau)$ for $n = 5$. The helix is approximated as a set of ring vortices plus a sheath

of axial vorticity beyond $n = 5$ to a final truncation point at $n = 15$. The purpose of this approximation is to further refine each influence coefficient value using less computer time than would otherwise be necessary if the quadrature algorithm were applied over the interval $n = 0$ to $n = 15$.

5.2 Quadrature Algorithm

Initially, standard quadrature routines from IMSL and NAG libraries were used to obtain numerical values for influence coefficients. Code execution profiling demonstrated that numerical integration consumed the greatest proportion of total computer processing time. Early attempts to improve performance focused on reducing the domain over which quadrature algorithms were applied by employing more approximate models for the far wake. Although modest improvements were made, greater performance gains were realized through code optimization specifically for the Cray X-MP/24. It was necessary to specially design a quadrature algorithm to take full advantage of the vector processing capability of this computer system (a brief outline of the vector processing concept has been provided in Appendix B).

The following criteria were applied in the design of the quadrature algorithm:

- Maximize the degree of vectorization
- Minimize the number of quadrature points

The degree of vectorization was increased by storing quadrature points in two large sparse 1-D arrays to which up to 32 points are added at a time. Having the quadrature points stored in vector data constructs permits vectorized point evaluation and vectorized application of the quadrature rule.

An important design requirement is to generate integral estimates with the least number of total function evaluations. Once again, the aforementioned data construct is advantageous since previously calculated quadrature points are retained for successive refinements. The algorithm must generate an integral estimate to within a specified tolerance or relative error. Generally, more closely spaced quadrature points will result in a more accurate integral estimate. But, integrand properties may be such that a high point density may only be required in a certain part of the domain to reach the desired level of accuracy. Early attempts consisted of concentrating quadrature points in regions nearest control points where the close proximity of vortices causes greater rates of change of each integrand. This approach met with limited success: performance was inconsistent across the parameter space. Finally, interval refinement was made dynamic so that the algorithm automatically responds to the behavior of each particular integrand. A stack based adaptive algorithm was designed to successively refine each half of an

interval in which convergence is not yet achieved. Consequently, quadrature points are concentrated only in regions of more difficult integrand behavior.

The choice of quadrature rule affects the number of function evaluations to convergence. A composite Newton-Cotes 5 point rule was selected to generate integral estimates. With five quadrature points over the interval $[a, b]$, the 5 point rule is

$$\int_a^b f(x)dx \approx \frac{2h}{45}[7f_0 + 32f_1 + 12f_2 + 32f_3 + 7f_4] \qquad (131)$$

where $h = (b-a)/n$ is the width of each one of n subintervals. If n is evenly divisible by four, the following composite rule follows directly from 131

$$\int_a^b f(x)dx \approx \frac{2h}{45}[7f_0 + 32f_1 + 12f_2 + 32f_3 + 14f_4 + \cdots + 7f_n] \qquad (132)$$

The Newton-Cotes 5 point rule is essentially an integral estimate given by a quartic polynomial fit over four subintervals; hence, the 5 point rule is exact for all polynomials of degree ≤ 5. The following illustrates the algorithm:

1. Divide the main integration interval into 32 subintervals.
2. Apply composite rule 132 to obtain integral estimate I_1.
3. Divide the interval into 64 subintervals.
4. Apply 132 to obtain I_2.
5. If $|(I_2 - I_1)/I_2|$ is less than the specified tolerance, then the desired integral value has been reached for the current subinterval.
6. If $|(I_2 - I_1)/I_2|$ is greater than the specified tolerance, then divide the current interval in half. The location within the work arrays of one half of this interval is saved in a stack to be processed at a later time. The other half interval is then processed through stages 2-6.
7. If convergence is difficult to obtain, many iterations of 2-6 will take place with many stack entries. Once convergence is reached for a subinterval, a previously stored subinterval is then recalled and processed in accordance with 2-6.
8. The final integral estimate is obtained once the stack is empty i.e. convergence has been achieved for all subintervals.

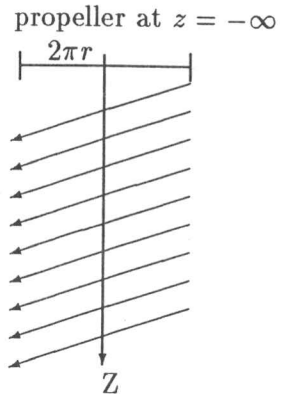

Figure 8: Two-dimensional representation of helical vortex system

The final algorithm design increased the average speed performance of the entire code by a factor of 2-3 times. In certain extreme cases such as large blade numbers and small advance coefficients, a better than four-fold increase in performance was realized.

5.3 The Far-Wake Approximation

The vorticity vector along a helical vortex line may be resolved into axial and circumferential components. The situation is illustrated in a two-dimensional representation ('unfolding') of a succession of helical filaments of radius r (fig. 8)

The vorticity vector $\vec{\Omega}$ along a helical filament may be resolved into axial and tangential components Ω_z, Ω_ν respectively. Total tangential vorticity due to a set of vortex filaments of equal radius is approximated by a cascade of ring vortices centered about the wake axis; and, total axial vorticity is approximated by a sheath of vorticity which is uniformly distributed over an imaginary cylindrical surface on which the helical filaments lie.

5.3.1 Ring Influence Coefficients

Ring vortices are separated by a distance equivalent to the axial separation between adjacent helical filaments, $l = P_\infty/B$. Each ring is positioned according to the relation,

$$\frac{z_k}{R_\infty} = 2n + \frac{2k-1}{2} \cdot \frac{2\pi\lambda_t}{B} \; ; k = 1, 2, 3 \ldots \tag{133}$$

where n is the number of wake diameters over which numerical integration is applied. Rings are added in accordance with equation 133 until a distance of 15 wake diameters from the xy plane is reached.

The approximate nature of the ring vortex cascade is such that a high degree of accuracy for each constituent ring influence coefficient is essentially

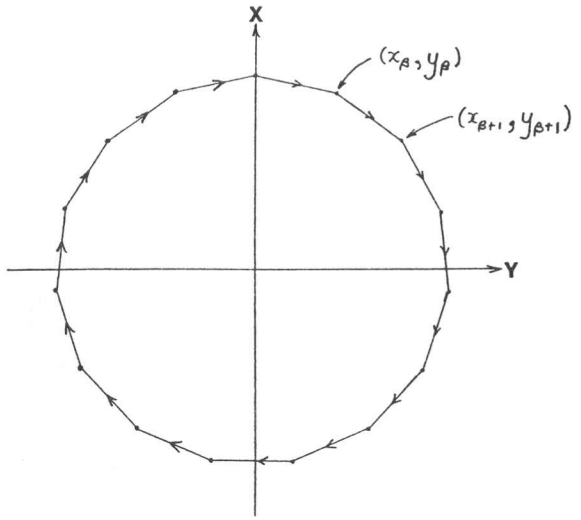

Figure 9: Approximation to a ring vortex

superfluous. Sufficient accuracy was obtained by generating each ring vortex from 15 straight-line segments. The advantage of this formulation lies in the fact that the influence coefficients for each segment are expressed in closed form. With the ring vortex geometry shown in fig. 9, the influence coefficient of ring vortex k at control point $\mathcal{P}(\zeta_i^1, 0, 0)$ is given by a summation over 15 straight-line elements,

$$\tilde{c}_{ik}^3 = \frac{\lambda_t}{B} \sum_{\beta=1}^{15} \{(x_\beta - \zeta_i^1)(y_{\beta+1} - y_\beta) - y_\beta(x_{\beta+1} - x_\beta)\} D \tag{134}$$

where

$$D = \frac{1}{ac - b^2} \left[\frac{a+b}{\sqrt{a+2b+c}} - \frac{b}{\sqrt{c}} \right] \tag{135}$$

$$a = (x_{\beta+1} - x_\beta)^2 + (y_{\beta+1} - y_\beta)^2 \tag{136}$$

$$b = (x_{\beta+1} - x_\beta)(x_\beta - \zeta_i^1) + (y_{\beta+1} - y_\beta) y_\beta \tag{137}$$

$$c = (x_\beta - \zeta_i^1)^2 + y_\beta^2 + z_k^2 \tag{138}$$

5.3.2 Sheath Influence Coefficients

Axial vorticity Ω_z is smeared out over a cylindrical surface of radius r_j to form a vortex sheath. Consider the corresponding two-dimensional case illustrated by figure 10. If the sheath vortex density is defined as γ_s then circulation about the differential arc element is

$$d\Gamma_z = \gamma_s r d\nu \; ; \; \gamma_s = \text{constant} \tag{139}$$

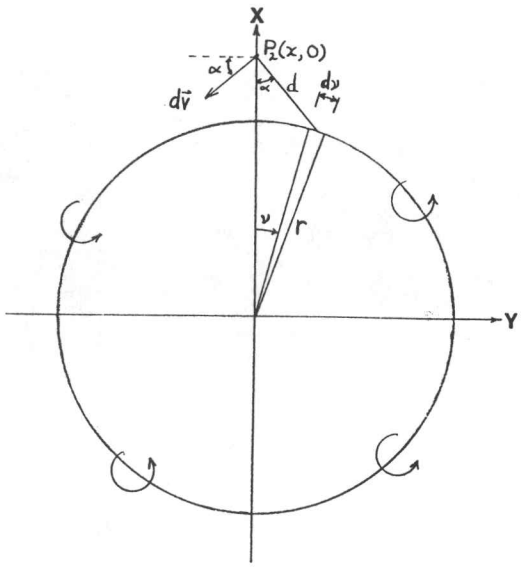

Figure 10: Sheath Induction - Exterior Region

From the definition of a 2-D vortex, the magnitude of the induced velocity at $\mathcal{P}_2$ is simply

$$|d\vec{v}| = \frac{\gamma_s r d\nu}{2\pi d} \tag{140}$$

By symmetry it can be seen that the integrated velocity due to the entire sheath will retain only the y component. Then,

$$dv_y = \frac{\gamma_s r d\nu}{2\pi d} \cdot \cos\alpha \tag{141}$$

but

$$\cos\alpha = \frac{x - r\cos\nu}{d} \tag{142}$$

giving

$$dv_y = \frac{\gamma_s r(x - r\cos\nu)}{2\pi d^2} d\nu \tag{143}$$

The distance d from the field point to a point on the sheath is also a function of ν

$$d^2 = x^2 + r^2 - 2xr\cos\nu \tag{144}$$

giving the integral

$$v_y = \frac{\gamma_s r}{2\pi} \int_0^{2\pi} \frac{x - r\cos\nu}{x^2 + r^2 - 2xr\cos\nu} d\nu \tag{145}$$

which finally yields

$$v_y = \frac{2\pi r\gamma_s}{2\pi x} \tag{146}$$

It can be readily seen from equation 146 that the vortex distribution is equivalent to a point vortex of intensity $2\pi r\gamma_s$ situated at the center.

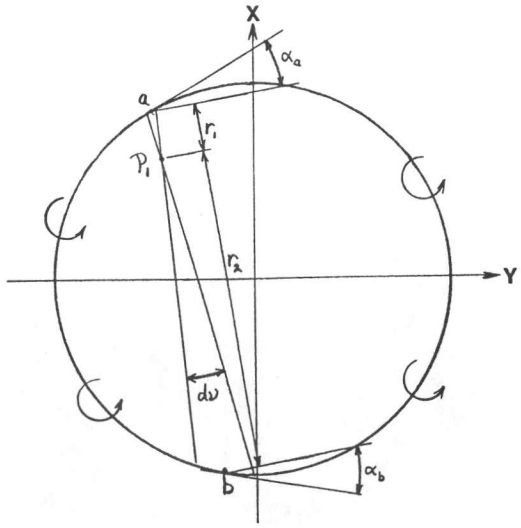

Figure 11: Sheath Induction - Interior Region

The induced velocity field in the interior regions of a vortex sheath can be explored through arguments of symmetry. Consider an arbitrary point $\mathcal{P}_1$ within the circular region enclosed by the vortex sheath, as shown by figure 11. Consider two chords which meet at $\mathcal{P}_1$ with the differential angle $d\nu$. Further, denote the point on the circumference which is a distance of r_1 for $\mathcal{P}_1$ by a. Similarly, denote the point on the opposite side which is a distance of r_2 from $\mathcal{P}_1$ by b. The differential arc lengths at a and b are then

$$ds_a = \frac{r_1 d\nu}{\cos\alpha_a} \tag{147}$$

$$ds_b = \frac{r_2 d\nu}{\cos\alpha_b} \tag{148}$$

where α_a and α_b are angles between the tangent to the circumference and the normal to the chord at a and b respectively. The velocity induced at $\mathcal{P}_1$ by the vortex elements of length ds_a and ds_b is

$$d\vec{v} = \left[\frac{\gamma_s ds_a}{2\pi r_1} - \frac{\gamma_s ds_b}{2\pi r_2}\right]\hat{n} \; ; \; \hat{n} = \text{unit normal to } ab \tag{149}$$

Upon substitution of equations 148 one obtains

$$d\vec{v} = \frac{\gamma_s d\nu}{2\pi}\left[\frac{1}{\cos\alpha_a} - \frac{1}{\cos\alpha_b}\right]\hat{n} \tag{150}$$

But, an axis of symmetry bisecting the chord ab will always exist. Therefore, the angles α_a and α_b are equivalent, which results in $d\vec{v} = 0$. The induction of the circumferential distribution of vorticity can be derived by the summation of all possible opposing element pairs in the above fashion.

Consequently, the flow velocity at all points within the circular region is equal to zero. The previous derivations have been developed assuming two dimensional flow. However, similar conclusions can be drawn in an extension to three dimensions. The parallel 3-D case is given simply by replacing the 2-D sheath with a cylindrical surface of vorticity; and, the equivalent point vortex is replaced by a line vortex of infinite extent. As a part of the far wake assumption the sheath approximation is introduced for the portion of the wake beyond $z_0/D_\infty = 5$. Consequently, the contribution to the rotational component is approximated by the influence coefficient of a line vortex coincident with the wake axis extending from $z/D_\infty = 5$ to $z/D_\infty = +\infty$. Specifically, for B filaments of radius r_j the approximate influence coefficient values for the far wake approximation are

$$\begin{aligned} \tilde{c}^2_{ij} &= 0 && \zeta^1_i < r_j \\ \tilde{c}^2_{ij} &= \frac{\lambda_t}{\zeta^1_i/R_\infty} \cdot \left(1 - \frac{z_0/R_\infty}{\sqrt{(\zeta^1_i/R_\infty)^2+(z_0/R_\infty)^2}}\right) && \zeta^1_i > r_j \end{aligned} \tag{151}$$

5.4 The Optimum Circulation Function

The solution of the system of equations 118 represents a set of nondimensional vortex filament intensities $\{\hat{\gamma}_j\}$. The ideal circulation function is then approximated by the distribution formed by a set of step discontinuities - each step being of magnitude $\hat{\gamma}_j$. Let $x_j = r_j/R_\infty$ be the nondimensional radius of a particular set of B helical filaments. The assigned value for the circulation distribution function at x_j is assumed to be equal to the average across the step as shown by figure 12. The approximate circulation intensity at points within $\{x_j\}$ is then

$$K_j = \begin{cases} 0 & j = 1, j = m \\ \frac{1}{2}\hat{\gamma}_j + \sum_{i=1}^{j-1} \hat{\gamma}_i & 1 < j < m \end{cases} \tag{152}$$

Functions $K(\lambda_t; x, B)$, calculated using 100 vortex filaments per propeller blade, are presented as lines of constant radius of which $x = 0.1$, 0.2, 0.3, 0.4, 0.5, 0.6, 0.7, 0.8, 0.85, 0.9, 0.95 (see figs. 20-28). These curves essentially represent a cross plot of data from equation 152 which approximates the function $K(x; \lambda_t, B)$. Circulation functions are computed for 22 values of λ_t over the interval $0.1 \leq \lambda_t \leq 3$. The curves are extended to $\lambda_t = 0$ using cubic spline interpolation over the interval $0 \leq \lambda_t \leq 3$. The spline is evaulated using theoretical boundary values $K(\lambda_t = 0; x, B) = 1$ and $\frac{dK}{d\lambda_t}\Big|_{\lambda_t=0} = 0$.

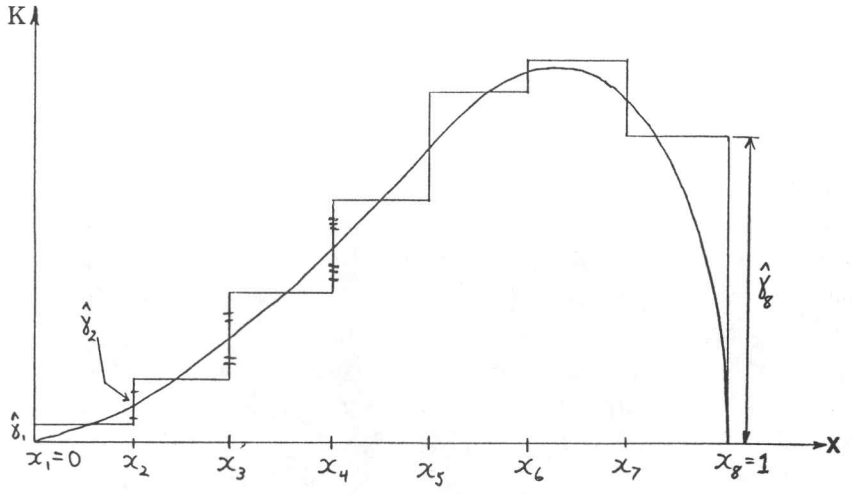

Figure 12: Step Approximation to the Ideal Circulation Function

5.5 The Mass Coefficient

The mass coefficient is defined by the integral (see section 3.1)

$$\kappa(\lambda_t; B) = 2 \int_0^1 K(x; \lambda_t, B) x dx \tag{153}$$

which is numerically evaluated by exactly integrating a cubic spline which is fit to the discrete distribution 152. A cubic spline is a piecewise cubic polynomial interpolation function in which the first and second derivatives are continuous across each data point. The spline consists of $m-1$ cubic polynomials each of which is defined by

$$S_j(x) = \alpha_j^0 + \alpha_j^1(x - x_j) + \alpha_j^2(x - x_j)^2 + \alpha_j^3(x - x_j)^3 \tag{154}$$

where

$$\begin{array}{l} x_j \le x \le x_{j+1} \\ 1 \le j \le m-1 \end{array} \tag{155}$$

Finally, the mass coefficient is approximated by

$$\kappa(\lambda_t; B) \approx 2 \sum_{j=1}^{m-1} \int_{x_j}^{x_{j+1}} S_j(x) x dx \tag{156}$$

The accuracy of each mass coefficient estimate improves with the number of helical filaments used to approximate each vortex sheet; however, practical computational limits are reached very rapidly as the number of filaments increase because of the m^2 dependence of processing time. One hundred filaments per blade was finally selected as the density limit. But, even more accurate mass coefficient values were obtained by extrapolating to an

infinite vortex filament density. Final mass coefficient values are obtained by extrapolating the series $\{\kappa_{m=25}, \kappa_{m=50}, \kappa_{m=100}\}$ to the limit $m = \infty$. The assumed interpolation function

$$\tilde{\kappa}_m = g_0 + g_1/m + g_2/m^2 \tag{157}$$

is used to obtain the refined estimate

$$\kappa(\lambda_t; B) \approx \lim_{m\to\infty} \tilde{\kappa}_m = g_0 \tag{158}$$

Mass coefficient values are calculated in this way for a set of values over $0 < \lambda_t \leq 10$.

Early calculations assumed endpoint values of the circulation function to be equal to one half of the step height at $x = 0$ and $x = 1$; but, the circulation should be identically equal to zero at the endpoints of the distribution. It has been shown that this oversight introduced less than 0.05% error in the final mass coefficient values.

5.6 Evaluation of Thrust and Power Coefficients

From section 3.3, the main performance parameters are given by

$$\begin{aligned} c_s &= 2\kappa\bar{w}[1 + \bar{w}(\frac{1}{2} + \frac{\epsilon}{\kappa})] \\ c_p &= 2\kappa\bar{w}(1 + \bar{w})(1 + \bar{w}\frac{\epsilon}{\kappa}) \\ \eta &= \frac{1 + \bar{w}(1/2 + \epsilon/\kappa)}{(1 + \bar{w})(1 + \bar{w}\cdot\epsilon/\kappa)} \end{aligned} \tag{159}$$

Since the coefficients κ and ϵ are functions of blade number and the far wake advance coefficient, the following functional dependencies are evident

$$\begin{aligned} c_s &= \mathcal{F}_n(\lambda_t, \bar{w}, B) \\ c_p &= \mathcal{F}_n(\lambda_t, \bar{w}, B) \\ \eta &= \mathcal{F}_n(\lambda_t, \bar{w}, B) \end{aligned} \tag{160}$$

But, this can be carried a step further since the far wake advance coefficient is related to the advance coefficient by

$$\lambda_t = (1 + \bar{w})\lambda \tag{161}$$

hence, the functional relationships become

$$c_s = \mathcal{F}_n(\lambda, \bar{w}, B) \quad (162)$$
$$c_p = \mathcal{F}_n(\lambda, \bar{w}, B) \quad (163)$$
$$\eta = \mathcal{F}_n(\lambda, \bar{w}, B) \quad (164)$$

However, it is more convenient to eliminate the displacement velocity in the thrust and power relations using

$$\bar{w} = \mathcal{F}_n(\lambda, \eta, B) \quad (165)$$

which is derived from 164. Hence, the more abstract displacement velocity is replaced by the propeller efficiency η,

$$c_s = \mathcal{F}_n(\lambda, \eta, B) \quad (166)$$
$$c_p = \mathcal{F}_n(\lambda, \eta, B)$$

Therefore, propeller thrust and power may be expressed in terms of the advance coefficient (which is approximated to first order by the *propeller* advance coefficient - see section 7), ideal efficiency (accounts for a total of four loss mechanisms), and the blade number. Following the format due to Kramer [16] curves of thrust or power vs. advance coefficient at constant efficiency were generated for different blade numbers. Figures 29-37 give curves of c_s vs. λ and figures 38-46 represent curves of c_p vs λ - all curves are at constant η. These graphs include the theoretical asymptotes corresponding to the limit $\lambda \rightarrow 0$ (see section 4.1). This format is a substantial improvement over Theodorsen's format in which graphical iteration is required. Instead, iteration is performed for the user which allows for direct interpretation of ideal propeller behavior.

The algorithm for generating curves $c_s(\lambda; \eta, B)$ and $c_p(\lambda; \eta, B)$ begins with solving relation 165 for the displacement velocity: For specified (λ, η, B), the required value for $\bar{w}$ is the root of the equation

$$\eta(1+\bar{w})(1+\frac{\epsilon}{\kappa}\bar{w}) - (\frac{1}{2}+\frac{\epsilon}{\kappa})\bar{w} - 1 = 0 \quad (167)$$

Equation 167 is not a quadratic function since ϵ and κ are implicit functions of $\bar{w}$ through equation 161. The functions $\kappa(\lambda, \bar{w}, B)$ and $\epsilon(\lambda, \bar{w}, B)$ which

[16] K.N. Kramer,"The Induced Efficiency of Optimum Propellers Having a Finite Number of Blades", NACA tech. memo. No. 884

is derived therefrom are limited by the domain of available mass coefficient data. Consequently, the iteration algorithm must be guaranteed to operate within the limited domain at all times. A Newton-Raphson type algorithm illustrates what could otherwise occur: if at some time during the iteration a point near a stationary value is encountered, the next iteration could conceivably go well outside of the domain. The method of regula-falsi [17] was selected because it has a relatively fast rate of convergence and it always stays within a determined bracket about the zero.

For each iteration, the required values of ϵ and κ are calculated from an interpolation function which is constructed from previously computed data $\{\kappa(\lambda_{t_i}; B), 1 \leq i \leq N\}$ where N is the total number of points defining the mass coefficient. A cubic spline, generated with free end boundary conditions, consists of $N-1$ piecewise cubic polynomials defined in a similar fashion to equation 154. The spline is then used to calculate the necessary coefficients:

$$\begin{array}{rcll} \kappa(\lambda_t) & \approx & S_i(\lambda_t) & \lambda_{t_i} \leq \lambda_t \leq \lambda_{t_{i+1}} \\ \frac{\epsilon}{\kappa}(\lambda_t) & \approx & 1 + \frac{1}{2}\frac{\lambda_t}{S_i(\lambda_t)} \cdot \frac{dS_i(\lambda_t)}{d\lambda_t} & \lambda_{t_i} \leq \lambda_t \leq \lambda_{t_{i+1}} \end{array} \tag{168}$$

Once $\bar{w}(\lambda, \eta, B)$ is determined, then substitution into equations 159 with the corresponding interpolated values for κ and ϵ yield the desired thrust and power coefficient values.

[17] R.L. Johnston, *Numerical Methods* , (Toronto: J. Wiley & Sons, 1982), p. 162

6 Algorithm Verification

Verification of the numerical algorithms may be divided into three categories:

1. Comparison with results from Theodorsen and Goldstein.
2. Numerical experiments.
3. Numerical estimates of limiting values and comparisons to theory.

In Theodorsen's approach, values characterizing ideal propeller behavior, including high loadings, are referenced to the far wake. Goldstein computed ideal circulation functions assuming light propeller loadings or, equivalently, vanishingly small displacement velocites $\bar{w}$. But, Goldstein circulation functions are also applicable to high loadings if values of advance are defined in terms of the far wake. A number of data points calculated by Goldstein [18] for a two blade propeller at $\lambda_t = 0.1, 0.25$ along with solutions from Kramer [19] are provided by figure 15 to facilitate a comparison with computed results. Data from Kramer were chosen for $\lambda_t = 0.5, 1.0$ because Kramer managed to circumvent some of the convergence difficulties experienced by Goldstein at large advance coefficients. These points are plotted with distributions generated by the code using 100 vortex filaments per blade for $\lambda_t = 0.1, 0.25, 0.5, 1.0$. Very good agreement is observed. The general tendency is for the code generated curves to lie above values from Goldstein and Kramer.

Goldstein circulation distributions for $\lambda_t = 0.1, 0.25$ were utilized to validate extrapolated mass coefficient estimates. The means of verification consists of calculating the correction factor to κ_{100} based on the differences between the computed circulation distribution K_{100} and Goldstein's data K_g. These values are then compared with the correction factors derived by extrapolation (section 5.5). Define the function $\varphi(x)$ such that

$$K_g(x) = [1 + \varphi(x)]K_{100}(x) \tag{169}$$

Then, the corresponding mass coefficient values are related by

$$\kappa_g = \kappa_{100} + 2\int_0^1 \varphi(x) x K_{100}(x) dx \tag{170}$$

[18] T. Theodorsen, *Theory of Propellers* (New York, 1948),p. 20

[19] Kramer, *op. cit.*

m	$\lambda_t = 0.2$	$\lambda_t = 0.5$	$\lambda_t = 1.0$	$\lambda_t = 5.0$
25	.62944	.27485	.10074	.0050302
50	.62792	.27331	.10009	.0049963
100	.62614	.27209	.099587	.0049696
200	.62490	.27133	.099275	.0049529
200*	.62499	.27137	.099291	.0049538
∞*	.62367	.27058	.098966	.0049364

Table 2: Mass coefficients based on m filaments/blade($B = 2$); * = extrapolated value based on $m = 25, 50, 100$

Consequently, the relative difference between the two mass coefficient estimates is then

$$\frac{\kappa_g - \kappa_{100}}{\kappa_{100}} = \frac{2\int_0^1 \varphi(x) x K_{100}(x) dx}{2\int_0^1 x K_{100}(x) dx} \tag{171}$$

Equation 171 simply represents an average of the relative difference in the circulation functions that is weighted by $xK_{100}(x)$. A discrete version of the weighted average was applied to the data listed by table 9 and table 10. For $\lambda_t = 0.1$ the weighted relative difference is -0.4% compared with the correction factor of -0.3% predicted by mass coefficient extrapolation. Similarly, the weighted relative difference for $\lambda_t = 0.25$ is -0.6% and a correction factor of -0.57% is predicted by mass coefficient extrapolation. Correction factors for all blade numbers range from -0.2% for small advance coefficients to -0.8% for large advance coefficients. Comparisons with Goldstein's data (three figure accuracy) lend a great deal of credibility to the refinement of mass coefficient values through extrapolation. Further validation of the extrapolation procedure was provided by comparing mass coefficients derived by extrapolation to 200 filaments per blade with directly computed values ($m = 200$). Test results for $B = 2$ at various values of advance are given by table 2. It can be seen from this table that the relative differences between extrapolated values ($m = 200$) and explicitly computed results are one order of magnitude smaller than the relative differences between κ_{100} and κ_{200}. Spotchecks for other blade numbers confirm these findings.

Various numerical experiments were performed to estimate the magnitude of error introduced by wake truncation and the far wake approximation. The effect of truncation was gauged for $B = 2$ and $B = 6$ by the progression of a series of mass coefficient values with $\{n = 1, 2, 5, 10, 15\}$ where n is the number of wake diameters to the point of truncation. Each value is com-

n	$\lambda_t = 0.2$		$\lambda_t = 0.5$		$\lambda_t = 1.0$		$\lambda_t = 5.0$	
1	.6632		.2784		.1001		.004966	
2	.6344	-4.3%	.2727	-2.0%	.09932	-0.8%	.004942	-.5%
5	.6249	-1.5	.2709	-.7	.09906	-.3	.004940	-.04
10	.6235	-.2	.2707	-.07	.09902	-.04	.004940	–
15	.6232	-.05	.2706	-.04	.09901	-.01	.004940	–

Table 3: Influence of truncation point on mass coefficient estimate, $B = 2$

n	$\lambda_t = 0.2$		$\lambda_t = 0.5$		$\lambda_t = 1.0$		$\lambda_t = 5.0$	
1	.8466		.4700		.1934		.01011	
2	.8019	-5.3%	.4549	-3.2%	.1902	-1.7%	.01004	-.7%
5	.7869	-1.9	.4499	-1.1	.1892	-.5	.01003	-.1
10	.7846	-.3	.4492	-.2	.1891	-.05	.01003	–
15	.7842	-.05	.4490	-.04	.1891	–	.01003	–

Table 4: Influence of truncation point on mass coefficient estimate, $B = 6$

puted without the use of the ring/sheath approximation; but, extrapolation to an infinite vortex filament density is performed. The degree of error due to truncation is inferred from the rate of convergence of each series. The results are given by table 3 and table 4 for $\lambda_t = 0.2, 0.5, 1.0, 5.0$. It has been generally observed that the change in mass coefficient values from $n = 10$ to $n = 15$ is less than 0.05%. It is perhaps a little surprising to realize that for small λ_t mass coefficient values reach 5-10% of their final values after only $n = 1$; and, mass coefficient values are within 1% of their final values for large λ_t. The error introduced by the far wake approximation is estimated by a few spot checks computed with numerical integration of the Biot- Savart law over the first 5 wake diameters (specified integration relative error = 0.000005) followed by the ring/sheath approximation beyond $n = 5$ to $n = 15$ (table 5). A comparison with results generated exclusively from the quadrature algorithm to $n = 15$ implies that the ring/sheath model introduces an error typically in the range of 0.05% to 0.1%. Combined, truncation and the ring/sheath approximation introduce errors in the order of 0.1%.

Figure 16 gives the mass coefficient for $B = 2, 3, 4, 6, 10, 12, \infty$ with a few data points taken from Theodorsen [20] for comparison. Note that data representing the case $B = 6$ were obtained by graphical interpolation from

[20] Theodorsen, *op. cit.*, p.36

B	$\lambda_t = 0.2$	$\lambda_t = 0.5$	$\lambda_t = 1.0$	$\lambda_t = 5.0$
2	.6236	.2706	.09897	.004936
6	.7845	.4491	.1889	.01002

Table 5: Mass coefficient values - wake approximation over the interval $5 < z/D_\infty \leq 15$

a set of curves [21] and are subject to graph reproduction and reading error whereas the data for $B = 2, 4$ are tabulated and are not subject to such additional error. The data points from Theodorsen generally agree with the computed curves to within 1-3%. Similarly, figure 17 compares the loss coefficient ratio curves ϵ/κ with tabulated data for $B = 2, 4$. However, a discrepancy with Theodorsen appears for the case $B = 4$ for $\lambda_t > 0.75$. Since the behavior of Theodorsen's results is inconsistent with behavior exhibited by curves $B = 2$ and $B = \infty$ (known exactly), these points can be safely discounted.

Theoretical propeller characteristics at large values of advance (see section 4.3) are used to formulate a further check on numerical solutions. The asymptotes to which computed values should progress are estimated by extrapolation and compared with theory. Ribner [22] showed, in effect (see pp. 28 herein), that for large λ_t the mass coefficient of a two blade propeller behaves as

$$\kappa(\lambda_t; B = 2) \longrightarrow \frac{1}{8\lambda_t^2} \tag{172}$$

Further, it was shown that propeller torque scales with wake kinetic energy per unit length giving,

$$\kappa(\lambda_t; B) \longrightarrow \frac{1}{8\lambda_t^2} \cdot \frac{Q_\infty^{(B)}}{Q_\infty^{(2)}} \tag{173}$$

Theoretical torque ratio values for different blade numbers are listed in table 1. For convenience, the torque ratio is denoted by

$$\sigma_B = \frac{Q_\infty^{(B)}}{Q_\infty^{(2)}} \tag{174}$$

Although the domain of computed data is $\lambda_t \leq 10$, the value of σ_B can be estimated from the ratio of code generated mass coefficients to the theoretical values $\{\kappa(\lambda_t, B = 2); \lambda_t >> 1\}$. An assumed extrapolation function

[21] Theodorsen, *op. cit.* , p.133
[22] Ribner *op. cit.*

B	$\lambda_t = 8$	$\lambda_t = 9$	$\lambda_t = 10$	$8a_1$
2	.0019425	.0015365	.0012455	0.998
3	.0026114	.0020655	.0016744	1.347
4	.0031471	.0024894	.0020180	1.618
6	.0039460	.0031220	.0025310	2.024
8	.0045114	.0035692	.0028938	2.327

Table 6: Mass coefficients and resulting approximate torque ratios

was used to estimate the value of this ratio in the limit of large advance coefficients. If the mass coefficient is assumed to take the form

$$\kappa(\lambda_t; B) \approx \frac{a_1}{\lambda_t^2} + \frac{a_2}{\lambda_t^3} + \frac{a_3}{\lambda_t^4} \tag{175}$$

then applying the interpolation condition at points $\{\lambda_{t_1} = 8, \lambda_{t_2} = 9, \lambda_{t_3} = 10\}$ yields the unknown constants a_i. The extrapolation will approach the curve a_1/λ_t^2 for large λ_t. The ratio of approximation 175 for $\lambda_t >> 1$ to equation 172 yields

$$\sigma_B \approx 8a_1 \tag{176}$$

The results are given by table 6. The torque ratios deduced by extrapolated code output agree with theory (table 1) to within 0.2% .

A similar approach was taken to find the asymptote of the thrust coefficient curve for large λ_t. The following assumed function is used to extrapolate thrust coefficient data:

$$c_s = \frac{b_1}{\lambda^2} + \frac{b_2}{\lambda^3} + \frac{b_3}{\lambda^4} \tag{177}$$

Hence, for large values of advance, the thrust coefficient will behave as

$$c_s \longrightarrow \frac{b_1}{\lambda^2} \tag{178}$$

If the numerical algorithms for c_s are correct then b_1, which is derived from computed data using equation 177, should match theoretical expectation (section 4.3), namely

$$b_1 \approx \frac{1}{2}\eta(1-\eta)\frac{Q_\infty^{(B)}}{Q_\infty^{(2)}} \tag{179}$$

Results are provided by table 7 and table 8. Excellent agreement is realized for most cases; however, agreement is not as good for the case $\eta = 0.5$.

η	b_1	$\frac{1}{2}\eta(1-\eta)\sigma_2$
0.5	0.1297	0.1250
0.7	0.10503	0.1050
0.9	0.04502	0.04500
0.95	0.02373	0.02375
0.99	0.004945	0.004950

Table 7: Constants defining c_s for $\lambda >> 1$; $(B = 2)$

η	b_1	$\frac{1}{2}\eta(1-\eta)\sigma_8$
0.5	0.2554	0.2913
0.7	0.2439	0.2447
0.9	0.1052	0.1049
0.95	0.05528	0.05534
0.99	0.01151	0.01153

Table 8: Constants defining c_s for $\lambda >> 1$; $(B = 8)$

This is probably due to the limited domain of computed data which spans $0.06 \leq \lambda_t \leq 10$. Consequently, the behavior in the limit is evaluated using much smaller values of λ for large $\bar{w}$. In fact the estimate for $\eta = 0.5$ had to be computed using the values $\{\lambda = 0.6, 0.7, 0.8\}$.

7 Slipstream Contraction

In addition to axial and rotational motion, wake self induction maintains a generally small radial component, v_r, which is responsible for contraction of the slipstream. The magnitude of v_r decreases from its value at the propeller to asymptotically approach zero in the far wake: arguments of antisymmetry can be used to prove that radial motion of a filament must vanish infinitely far downstream. Consequently, the wake radius asymptotically approaches the far wake value R_∞ starting from the radius at the propeller R.

For heavy blade loadings, slipstream contraction is important in relating conditions in the far wake to conditions at the propeller - a necessary task in applying Theodorsen's theory. The propeller advance coefficient $\lambda_p = V/\omega R$ is related to the far wake advance coefficient by

$$\lambda_p = \frac{R_\infty}{R} \cdot \lambda \tag{180}$$

$$= \frac{R_\infty}{R} \cdot \frac{\lambda_t}{1+\bar{w}}$$

and thrust and power coefficients based on parameters at the propeller plane,

$$c_{p,p} = \frac{P}{\frac{1}{2}\rho V^3 \pi R^2} \tag{181}$$

$$c_{s,p} = \frac{T}{\frac{1}{2}\rho V^2 \pi R^2} \tag{182}$$

are related to their far wake counterparts by

$$c_{p,p} = (\frac{R_\infty}{R})^2 c_p \tag{183}$$

$$c_{s,p} = (\frac{R_\infty}{R})^2 c_s \tag{184}$$

It can be seen that even a modest degree of slipstream contraction, say 5%, would cause approximately 10% error in the thrust and power coefficients if it were assumed that $R_\infty/R \approx 1$. Fortunately, it turns out that contraction is generally much less for moderate loadings; hence, its effect can usually be ignored. However, slipstream contraction should be examined in an analysis involving heavily loaded propellers.

7.1 Theory

In actuator disc theory, the wake is contained by a stream tube surface through which no fluid may pass. Consequently, mass continuity can be readily applied to relate propeller and far wake radii. In contrast, the vortex model imposes no such condition on the flow; hence, evaluating wake contraction is more complex. Theodorsen detailed two methods from which contraction estimates may be derived [23], the first of which consists of integrating the radial velocity along the edge of a helical vortex sheet. Wake contraction , ΔR, is given by

$$\Delta R = -\int dr \tag{185}$$

$$= -\int_0^\infty \frac{dr}{dz}\, dz$$

[23] Theodorsen, *op. cit.* , pp. 77-87

but,

$$\frac{dr}{dz} = \frac{v_r}{V} \equiv \bar{v}_r \tag{186}$$

giving

$$\Delta R = -\int_0^\infty \bar{v}_r \, dz \tag{187}$$

Theodorsen found it more convenient to express the problem in terms of the angular displacement θ,

$$\begin{aligned} dz &= \frac{d\theta}{2\pi} \cdot P_\infty \\ &= R_\infty \lambda_t d\theta \end{aligned} \tag{188}$$

which yields the integral

$$\frac{\Delta R}{R_\infty} = -\lambda_t \int_0^\infty \bar{v}_r \, d\theta \tag{189}$$

for which Theodorsen obtained numerical estimates for 2 and 4 blades. But, radial velocities were calculated from a prescribed spatial distribution of vorticity; namely, a system of interleaved vortex sheets of *constant pitch* . Since the displacement velocity increases from approximately $w/2$ at the propeller to w in the far wake, helicoid pitch will change significantly with downstream distance under heavy loading. Thus, Theodorsen's contraction coefficients are only valid for light propeller loadings (i.e. $\bar{w} << 1$).

A second approach based on the condition of compatibility between thrust expressions was also developed by Theodorsen.

Vortex continuity equates bound circulation at the propeller with the far wake distribution. Integration of the thrust distribution derived therefrom along a propeller blade yields a value that must be identical with equation 68. Consider the velocity diagram at the propeller plane illustrated by figure 13. Therein a_0 represents the displacement velocity and $\vec{u}$ is the resultant flow vector which is inclined to the plane of rotation by θ_p. The resultant $\vec{u}$ is the vector sum of the induced velocity $a_0 \cos\theta_p$, flight velocity V, and rotational velocity ωr. The magnitude of $\vec{u}$ is given by

$$\begin{aligned} u &= \frac{V + a_0}{\sin\theta_p} - a_0 \sin\theta_p \\ &= \frac{V + a_0 \cos^2\theta_p}{\sin\theta_p} \end{aligned} \tag{190}$$

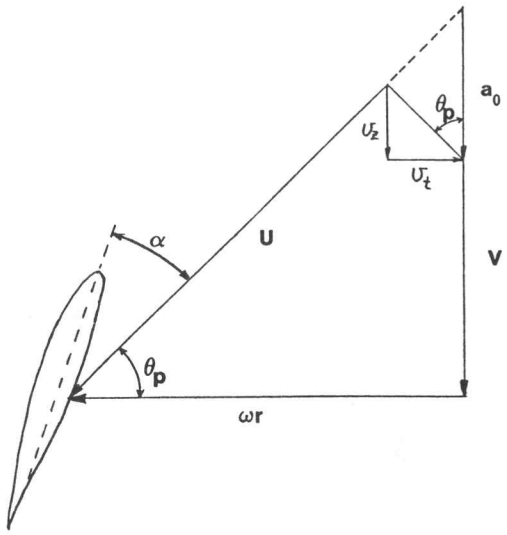

Figure 13: Flow Vector Diagram in Propeller Fixed Frame

From the Kutta-Joukowski theorem, a single blade element at r will generate lift

$$dL = \rho u \Gamma \, dr \tag{191}$$

which has a thrust component of

$$dT = \rho u \Gamma \cos\theta_p \, dr \tag{192}$$

Consequently, a propeller with B blades will produce a total thrust of

$$T = \rho B \int_0^R \frac{V + a_0 \cos^2\theta_p}{\tan\theta_p} \Gamma(r) \, dr \tag{193}$$

Since $\tan\theta_p = (V + a_0)/\omega r$, one has

$$T = \rho B \omega \int_0^R \frac{V + a_0 \cos^2\theta_p}{V + a_0} \Gamma(r) r \, dr \tag{194}$$

Equation 194 is nondimensionalized using

$$\begin{aligned} r &= Rx \\ a_0 &= V\bar{a}_0 \\ w &= V\bar{w} \end{aligned} \tag{195}$$

$$\begin{aligned} T &= \frac{1}{2}\rho V^2 \pi R_\infty^2 c_s \\ \Gamma &= lwK \\ &= \frac{2\pi w(V+w)}{\omega B} \cdot K \end{aligned} \tag{196}$$

which yields

$$(\frac{R_\infty}{R})^2 c_s = \frac{2\bar{w}(1+\bar{w})}{1+\bar{a}_0} \cdot 2 \int_0^1 (1 + \bar{a}_0 \cos^2\theta_p) K(x) x \, dx \tag{197}$$

and, from Theodorsen's theory of the far wake, the quantities

$$\kappa = \int_0^1 2xK(x)dx \tag{198}$$

$$c_s = 2\kappa\bar{w}[1+\bar{w}(\frac{1}{2}+\frac{\epsilon}{\kappa})]$$

are coupled with the definition

$$\mathcal{S} \equiv \frac{1}{\kappa}\int_0^1 2xK(x)\cos^2\theta_p(x)\,dx \tag{199}$$

giving finally

$$(\frac{R_\infty}{R})^2 = \frac{(1+\bar{w})(1+\bar{a}_0\mathcal{S})}{(1+\bar{a}_0)[1+\bar{w}(1/2+\epsilon/\kappa)]} \tag{200}$$

as the equation for evaluating the contraction. Theodorsen [24] states that if the efficiency is written in the form

$$\eta = \frac{1}{1+\bar{a}_0} \tag{201}$$

then the quantity $\bar{a}_0$ gives the displacement velocity at the propeller plane. This result can be seen if one considers the rate at which the reaction to the lift distribution $\mathcal{L}$(r) does work on the induced flow at the propeller plane,

$$P_{loss} = B\int_0^R \mathcal{L}(r)a_0\cos\theta_p(r)\,dr \tag{202}$$

and, the total thrust

$$T = B\int_0^R \mathcal{L}(r)\cos\theta_p(r)\,dr \tag{203}$$

when multiplied by the flight speed gives the rate at which useful work is done. Efficiency is defined by the ratio,

$$\eta = \frac{TV}{TV+P_{loss}} \tag{204}$$

which yields upon substitution of equations 202 and 203 the desired result 201. Equating equation 201 to the efficiency based on the far wake (equation 71) gives,

$$\bar{a}_0 = \frac{\frac{1}{2}\bar{w}+\frac{\epsilon}{\kappa}\bar{w}^2}{1+\bar{w}(\frac{1}{2}+\frac{\epsilon}{\kappa})} \tag{205}$$

[24] Theodorsen, *op. cit.* , p.31

With the corresponding power series in $\bar{w}$ from Theodorsen

$$\bar{a}_0 = \bar{w}/2 - \frac{1}{2}(\frac{1}{2} - \frac{\epsilon}{\kappa})\bar{w}^2 + \frac{1}{2}(\frac{1}{4} - \frac{\epsilon^2}{\kappa^2})\bar{w}^2 + \cdots \tag{206}$$

it can be seen that for light loadings ($\bar{w} << 1$)

$$\bar{a}_0 \approx \frac{1}{2}\bar{w} \tag{207}$$

which is identical to actuator disc theory. Theodorsen used the linearizing approximation $\bar{w} << 1$ several times to obtain

$$Y \equiv \frac{\Delta R}{R} \cdot \frac{\kappa}{c_s} \approx \frac{1}{4}(\frac{\epsilon}{\kappa} - \frac{1}{2}\mathcal{S}) \tag{208}$$

7.2 Numerical Solutions

Numerical techniques were applied to obtain contraction coefficient values without resorting to linearizing approximations. The algorithm is designed to calculate the contraction coefficient

$$\hat{Y} = \frac{1}{2\bar{w}}\frac{\Delta R}{R} \tag{209}$$

given $\bar{w}, \lambda_t, B$. The displacement velocity at the propeller is given immediately by substitution into equation 205. The identity

$$\cos^2\theta_p = \frac{1}{1 + \tan^2\theta_p} \tag{210}$$

and the relation

$$\tan^2\theta_p = \left(\frac{V + a_0}{\omega r}\right)^2 \tag{211}$$

are used to express $\cos^2\theta_p$ in terms of λ_p and $\bar{a}_0$,

$$\cos^2\theta_p = \frac{x^2}{x^2 + \lambda_p^2(1 + \bar{a}_0)^2} \tag{212}$$

hence, 199 becomes

$$\mathcal{S} = \frac{1}{\kappa}\int_0^1 2xK(x)\frac{x^2}{x^2 + (\frac{1+\bar{a}_0}{1+\bar{w}})^2(\frac{R_\infty}{R})^2\lambda_t^2}\,dx \tag{213}$$

The circulation functions needed to evaluate $\mathcal{S}$ are calculated from pre-computed data which consists of 22 distributions over the interval $0 \leq \lambda_t \leq 3$. This data was evaluated using 100 vortex filaments per blade. Circulation distributions for any λ_t within the interval are obtained by cubic spline interpolation. On each iteration, $\mathcal{S}$ is evaluated using cubic spline integration over 100 quadrature points. Note that exact analytic expressions for $K(x)$, κ, and ϵ are used for $B = \infty$.

It is because of the functional dependence of $\mathcal{S}$ on $(\frac{R_\infty}{R})$ that the contraction ratio cannot be evaluated by direct substitution into 200. A regula-falsi iteration is used to solve the equation

$$\left(\frac{R_\infty}{R}\right)^2 - \frac{(1+\bar{w})(1+\bar{a}_0\mathcal{S}(\frac{R_\infty}{R}))}{(1+\bar{a}_0)[1+\bar{w}(\frac{1}{2}+\frac{\epsilon}{\kappa})]} = 0 \tag{214}$$

from which the contraction coefficient is evaluated

$$\hat{Y} = \frac{1}{2\bar{w}}(1 - \frac{R_\infty}{R}) \tag{215}$$

Families of curves $\hat{Y}$ vs. λ_t at various constant $\bar{w}$ are given by figures 47-55 for $B = 2, 3, 4, 5, 6, 8, 10, 12, \infty$. Data presentation includes values from Theodorsen [25] for comparison. Best agreement should be found between Theodorsen's data and the curves $\bar{w} = 0.01$. Only modest agreement is observed for $B = 2, 4$. It should be noted, however, that Theodorsen did express certain reservations about the accuracy of his computed results. He stated that for $B = 2, 4$:

> The calculations involve triple integrations and are therefore somewhat laborious and susceptable to numerical errors ... it is hoped that the values given in this paper will serve the purpose [26]

Very good agreement is seen for $B = \infty$. Further verification was supplied from the theoretical limit $\lambda_t \to 0$. In this limit $\epsilon/\kappa \to 1$ and $\cos^2\theta_p \to 1$ giving

$$\hat{Y} = \frac{1}{2\bar{w}}\left(1 - \sqrt{\frac{1+\bar{w}}{1+\frac{3}{2}\bar{w}}}\right) \tag{216}$$

[25] Theodorsen, *op. cit.*, p. 82

[26] T. Theodorsen, 'The Theory of Propellers III - The Slipstream Contraction with Numerical Values for Two-Blade and Four-Blade Propellers', NACA ACR L4J10, 1944, p. 12

which is independent of blade number. This equation verifies the intercepts along the line $\lambda_t = 0$.

The contraction coefficient is seen to decrease with increasing λ_t. This effect can be attributed to the increase in rotation at the expense of axial flow. In fact, axial flow is non-existant with zero contraction at $\lambda_t = \infty$. A further observation is that the rate at which the contraction coefficient decays with λ_t is greater for $B = 2$ than $B = \infty$. This effect may be ascribed to tip loss: reduced blade number increases the degree of flow spillage outside the helicoid. This effect may also be responsible for the slight wake *expansion* observed for finite blade numbers under high loadings.

As a cautionary note, verification of negative contraction coefficients has not been performed because of time constraints. As a possible means of verification, equation 189 can be numerically evaluated wherein v_r is calculated by the Biot-Savart law along a filament of radius R_∞. But, this process would be complicated by the axial variation in pitch given by

$$P(z) = \frac{2\pi}{\omega}(V + \mathcal{W}(z)) \tag{217}$$

where $\mathcal{W}$ will increase from a_0 at the propeller and asymptotically approach the far wake value w. $\mathcal{W}$ would have to be obtained from a time iteration of the self-induced motion of the wake helicoid. The displacement velocity function would then be calculated from the converged wake shape.

8 Propeller Design

The following is a summary of Theodorsen's design methodology [27] with some slight modifications. Herein the updated and extended curves assist in this design method.

At each blade section, the flow is considered to be locally two dimensional where the resultant relative flow vector is derived from the flight speed and rotation of the propeller plus the axial and rotational increments due to wake induction. Under this assumption, the design problem essentially consists of deriving the pitch distribution, chord distribution and choice of airfoil sections for the optimum propeller given the shaft power, rate of rotation, flight speed and propeller radius.

The flow vector diagram (figure 13) illustrates the desired quantities u, θ_p which are expressed exactly in terms of the far wake parameters $\lambda_t, \bar{w}$. As

[27] Theodorsen, *op. cit.* , pp. 46-65

detailed earlier in section 7, the magnitude of the flow velocity relative to the blade element at radius r is

$$\frac{u}{V} \equiv \bar{u} = \frac{1 + \bar{a}_0 \cos^2 \theta_p}{\sin \theta_p} \tag{218}$$

where the displacement velocity at the propeller plane is

$$\bar{a}_0 = \frac{\frac{1}{2}\bar{w} + \frac{\epsilon}{\kappa}\bar{w}^2}{1 + \bar{w}(\frac{1}{2} + \frac{\epsilon}{\kappa})} \tag{219}$$

and the direction of the flow is given by

$$\tan \theta_p = \frac{V(1 + \bar{a}_0)}{\omega r} \tag{220}$$

In terms of $\lambda_t, \bar{w}$, the direction of $\vec{u}$ becomes

$$\tan \theta_p = \frac{\lambda_t}{x} \cdot \frac{1 + \bar{a}_0}{1 + \bar{w}} \cdot \frac{R_\infty}{R} \tag{221}$$

but, slipstream contraction is given by

$$\frac{\Delta R}{R} = 2\bar{w}\hat{Y}(\lambda_t) \tag{222}$$

yielding

$$\theta_p(x) = \arctan \left\{ \frac{\lambda_t}{x} \cdot \frac{1 + \bar{a}_0}{1 + \bar{w}} \cdot [1 - 2\bar{w}\hat{Y}(\lambda_t)] \right\} \tag{223}$$

where $x \equiv r/R$. Moreover, specification of $\lambda_t, \bar{w}$ immediately gives the optimum circulation function at the propeller,

$$\Gamma(x) = lwK(\frac{r}{R_\infty}; \lambda_t) \tag{224}$$

$$= \frac{2\pi R_\infty \lambda_t}{B} wK(\frac{r}{R_\infty}; \lambda_t) \tag{225}$$

where $K(r/R_\infty)$ is given by a cross-plot of curves $K(\lambda_t; x, B)$ from one of figures 20-28. With the relative flow velocity and circulation known, the distribution of lift results

$$\rho u \Gamma = \frac{1}{2}\rho u^2 c C_L \tag{226}$$

from which one has

$$\bar{c}C_L = \frac{4\pi\lambda_t}{B} \cdot \frac{\bar{w}\sin\theta_p}{1+\bar{a}_0\cos^2\theta_p}(1-2\bar{w}\hat{Y})K \tag{227}$$

where the nondimensionalized chord is given by $\bar{c} \equiv c/R$ and C_L is the section lift coefficient at x. Theodorsen [28] recommends specifying a value for C_L and choosing an airfoil section for which this value represents the ideal lift coefficient. Whatever the choice of C_L and profile section, the combination should correspond to the least possible sectional drag based on experimental data. Once appropriate lift coefficient values are chosen along the propeller blade, equation 227 specifies the chord distribution. The angle of attack, which is specified by the chosen C_L and profile section, is $\alpha = \beta - \theta_p$ where β is the local propeller pitch angle. Therefore,

$$\beta = \alpha + \arctan\left\{\frac{\lambda_t}{x} \cdot \frac{1+\bar{a}_0}{1+\bar{w}}(1-2\bar{w}\hat{Y})\right\} \tag{228}$$

Thus far, all quantities have been expressed exactly in terms of the far wake parameters λ_t and $\bar{w}$; but, these quantities are initially unknown. From the specified design parameters the following coefficient values at the propeller are known

$$c_{p,p} = \frac{P}{\frac{1}{2}\rho V^3 \pi R^2} \tag{229}$$

$$\lambda_p = \frac{V}{\omega R} \tag{230}$$

The power input P represents the sum of useful power TV, induced loss P_{loss}, and power loss due to friction. But, Theodorsen's equations (eqn. nos. 68, 69 and 71) do not account for the latter. If t_t represents the portion of shaft power lost due to drag (in coefficient form) then the power coefficient becomes

$$c_p = \frac{c_{p,p} - t_t}{(1-2\bar{w}\hat{Y})^2} \tag{231}$$

However, Theodorsen argues that t_t is generally quite small ($t_t \approx 0.01 c_p$) and may be ignored; however, if it is found to be a significant term then the correction may be subsequently applied [29]. Therefore, the far wake

[28] Theodorsen, *op. cit.*, p. 61
[29] Theodorsen, *op. cit.*, p. 54

counterparts of equations 229 and 230 are

$$c_p \approx \frac{c_{p,p}}{(1-2\bar{w}\hat{Y})^2} \tag{232}$$

$$\lambda = \frac{\lambda_p}{(1-2\bar{w}\hat{Y})} \tag{233}$$

Herein lies the requirement for iteration: the denominators are functions of the initially unknown parameters. The iteration is initiated by assuming $\hat{Y}_1 = 0$. From equations 232 and 233 one obtains c_{p_1}, λ_1 which is then used to obtain the displacment velocity w_1. The displacement velocity represents the solution of the equation

$$2\bar{w}\kappa(\lambda,\bar{w})[1+\bar{w}][1+\bar{w}\frac{\epsilon}{\kappa}(\lambda,\bar{w})] - c_p = 0 \tag{234}$$

which is numerically evaluated by a process identical to that described in section 5.6. Solutions generated therefrom are presented as curves of $\bar{w}$ vs. c_p at constant λ for various B (figures 56-64): the displacement velocity is then obtained by interpolation.

The updated estimate of the contraction coefficient $\hat{Y}_2$ is obtained for $\lambda_{t_1} = (1+\bar{w}_1)\lambda_1$ by interpolation using one of figures 47-55. Substitution into equation 232 and 233 then yields the next set of values c_{p_2} and λ_2 from which $\bar{w}_2$ is obtained. For most cases the small degree of contraction is such that no more than one iteration may be required.

Drag estimates may be obtained by integrating the drag distribution

$$\vec{\mathcal{D}} = \frac{1}{2}\rho u^2 c C_D \cdot \frac{\vec{u}}{|\vec{u}|} \tag{235}$$

along the span of the propeller. The total axial force opposing the thrust vector is then

$$D_a = B\int_0^R \frac{1}{2}\rho u^2 c C_D \cdot \sin\theta_p \, dr \tag{236}$$

which becomes upon substitution of equation 218

$$D_a = \frac{1}{2}\rho V^2 \int_0^R \frac{(1+\bar{a}_0\cos^2\theta_p)^2}{\sin\theta_p} c C_D \, dr \tag{237}$$

with the nondimensional equivalent based on the propeller radius

$$t_a = \frac{B}{\pi}\int_0^1 \frac{(1+\bar{a}_0\cos^2\theta_p)^2}{\sin\theta_p} \bar{c} C_D \, dx \tag{238}$$

The additional torque due to frictional losses is obtained from the tangential component of $\mathcal{D}$,

$$\mathcal{Q} = B \int_0^R \frac{1}{2} \rho u^2 c C_D \cdot r \cos\theta_p \, dr \tag{239}$$

Again, substitution of equation 218 yields

$$\mathcal{Q} = B \int_0^R \frac{1}{2} \rho V^2 \frac{\omega r^2}{V(1+\bar{a}_0)} \cdot \frac{(1+\bar{a}_0 \cos^2\theta_p)^2}{\sin\theta_p} c C_D \, dr \tag{240}$$

The corresponding power increment expressed in nondimensional form is finally

$$\begin{aligned} t_t &= \frac{\omega \mathcal{Q}}{\frac{1}{2}\rho V^3 \pi R^2} \\ &= \frac{B}{\pi \lambda_p^2} \int_0^1 \frac{(1+\bar{a}_0 \cos^2\theta_p)^2}{(1+\bar{a}_0)\sin\theta_p} \bar{c} C_D x^2 \, dx \end{aligned} \tag{241}$$

Theodorsen's expressions for t_a, t_t can be obtained from equations 238 and 241 by introducing the approximation $\bar{a}_0 = 0$, which is equivalent to the assumption of zero loading.

The influence of viscous losses on total thrust and power coefficients is clear: the axial drag component gives a reduction in thrust

$$c_{s,p} = c_s \cdot (1 - 2\bar{w}\hat{Y})^2 - t_a \tag{242}$$

and the tangential drag component produces an increase in power

$$c_{p,p} = c_p \cdot (1 - 2\bar{w}\hat{Y})^2 + t_t \tag{243}$$

which finally gives the propeller efficiency

$$\eta_p = \frac{c_{s,p}}{c_{p,p}} \tag{244}$$

The preceding analysis differs from Theodorsen in the reduced reliance on the assumption of light loadings: 1) he assumed that $\bar{a}_0 \approx \bar{w}/2$ in the derivation of the function cC_L, 2) he assumed that $c_p \approx c_{p,p}$ essentially omitting corrections necessary to account for wake contraction and viscous losses by arguing that these effects are small and tend to oppose each other, 3) he assumed that $\bar{a}_0 = 0$ in calculating the corrections to ideal thrust and power coefficients due to friction; but, this was justified by the degree

of error in drag coefficient data. The design method is assisted by the curves $\bar{w}(c_p; \lambda, B)$ from which $\bar{w}$ may be obtained directly by interpolation. Moreover, extended circulation function data has been provided by this work for many more cases over a wider domain: load distributions for any λ_t, $(0 \leq \lambda_t \leq 2)$, have been provided for $B = 2, 3, 4, 5, 6, 8, 10, 12, \infty$. Similarly, more extensive contraction coefficient curves have been provided for $B = 2, 3, 4, 5, 6, 8, 10, 12, \infty$.

9 Summary and Discussion

The behavior of ideal propellers has been examined using the theoretical tools provided by Theodorsen. Therein, all results are expressed in terms of parameters describing the far wake. The rationale for this approach lies principally in its ability to remove the restriction to light loadings found in earlier theories. Hence, fundamental wake properties such as momentum and axial kinetic energy cross section ratios (i.e. κ, ϵ) are rendered independent of the displacement velocity $\bar{w}$ (i.e. independent of loading). Similarly, ideal load distributions are collapsed for all $\bar{w}$. The basic equations of thrust, power and efficiency are then expressed as functions of $\bar{w}, \kappa, \epsilon$ using conservation equations. The cost of this approach lies with the initially unknown parameter $\bar{w}$: iteration is required to express $\bar{w}$ in terms of quantities known at the propeller.

The mass coefficient κ represents an average value of the ideal circulation distribution weighted by $2x$. The ideal circulation function is, in turn, a unique function of the far wake pitch for a given blade number. Circulation functions K were calculated using a numerical model of the far wake consisting of a finite number of helical vortex filaments. With this model, the Betz condition is manifest as a linear system of equations in the unknown filament intensities - the solution of which represents an approximation to K. All other quantites, which are essentially subordinate to K, are computed by various quadrature and interpolation algorithms. Mass coefficient values κ, and loss coefficient ratios ϵ/κ are presented by figures 16-19 for various number of blades: B=2,3,4,5,6,8,10, 12,∞.

Figures 20-28 present ideal circulation (100 filaments/blade) as a function of λ_t at constant blade radius. Circulation values are given for any λ_t, $(0 \leq \lambda_t \leq 2)$ at a number of radial stations: x = 0.1, 0.2, 0.3, 0.4, 0.5, 0.6, 0.7, 0.8, 0.85, 0.9, 0.95. Circulation distributions along the wake radius are thus equivalent to a cross plots of these curves.

Theodorsen's theory gives exact expressions for thrust and power in terms of the far wake advance λ_t and the displacement velocity $\bar{w}$. These equations were recast herein in terms of $\lambda = V/\omega R_\infty$, which approximates the propeller advance coefficient $\lambda_p = V/\omega R$, and the ideal efficiency η instead of $\lambda_t, \bar{w}$. Thus, ideal propeller behavior has been expressed (approximately) in terms of quantities at the propeller: the requisite iterations have been performed for the user in the elimination of $\bar{w}$ from the equations. Thrust coefficients for various blade numbers are given as lines of constant ideal efficiency vs. λ by figures 29-37, and figures 38-46 give the corresponding power coefficient curves.

Figures 56-64 present the displacement velocity as a function of c_p at constant λ. Curves $\bar{w}(c_p; \lambda, B)$ represent an improvement over Theodorsen's format in which the user must obtain each $\bar{w}$ by iteration. This is particularly important to the application of this theory to propeller design.

Theodorsen presented two possible means with which one may compute the contraction of the slipstream. Once approach consists of integrating the radial flow velocity along the edge of the helicoid. The second approach is based on the condition of compatibility between thrust at the propeller and thrust expressed in terms of the far wake. Theodorsen applied the first approach to obtain contraction coefficients for two blade and four blade propellers; but, the assumption of light loading was made in his calculations. Herein, contraction coefficients were evaluated using the second approach without the simplifying assumption of light loading. Figures 47-55 give contraction coefficient curves at various constant $\bar{w}$ for various blade numbers. The results demonstrate that wake contraction generally varies inversely with λ_t. Surprisingly, *negative* contraction coefficients were observed for finite blade numbers at certain λ_t under heavy loading. It is possible that this effect is due to tip loss - the flow spillage outside the helicoid. However, verification of this result using a different means has not been perfromed; hence, this result should be viewed with slight caution.

References

[1] Durand, W. F., *Aerodynamic Theory*, Vol. iv, 1935

[2] Glauert, H., *The Elements of Aerofoil and Airscrew Theory*, Cambridge, 1959

[3] Goldstein, S., "On the Vortex Theory of Screw Propellers," Proc. Roy. Soc., London, Vol. 123, 1929

[4] Johnston, R. L., *Numerical Methods*, John Wiley and Sons, Toronto, 1982

[5] Kochin, N. E., et. al., *Theoretical Hydromechanics*, John Wiley and Sons, New York, 1964

[6] Kramer, K. N., "The Induced Efficiency of Optimum Propellers Having A Finite Number of Blades," NACA Tech. Memo. No. 884

[7] McCormick, B. W., *Aerodynamics, Aeronautics, and Flight Mechanics*, John Wiley and Sons, New York, 1979

[8] Mikkelson, D. C., Mitchell, G. A., and Bober, L. J., "Summary of Recent NASA Propeller Research," NASA Tech. Memo. 83733, 1984

[9] Milne-Thompson, L. M., *Theoretical Aerodynamics*, 4^{th} ed., Dover Publications, New York, 1966

[10] Ribner, H. S., " A Transonic Propeller of Triangular Plan Form," NACA TN 1303, 1947

[11] Ribner, H. S., " Damping in Roll of Cruciform and Some Related Delta Wings at Supersonic Speeds," NACA Tech. Memo. No. 2285, 1951

[12] Sullivan, J. P., " Advanced Theoretical Treatments of Propeller Aerodynamics," Von Karman Institute for Fluid Dynamics, Lecture Series 1982-08: Propeller Performance and Noise, May 24-28, 1982

[13] Theodorsen, T., " The Theory of Propellers I - Determination of the Circulation Function and the Mass Coefficient for Dual Rotating Propellers," NACA ACR L4H03, 1944

[14] Theodorsen, T., " The Theory of Propeller II - Method for Calculating the Axial Interference Velocity," NACA ACR L4119, 1944

[15] Theodorsen, T., " The Theory of Propellers III - The Slipstream Contraction with Numerical Values for Two-blade and Four-blade Propellers," NACA ACR L4J10, 1944

[16] Theodorsen, T., " The Theory of Propellers IV - Thrust, Energy, and Efficiency Formulas for Single and Dual-rotating Propellers with Ideal Circulation Distribution," NACA ACR L4J12, 1944

[17] Theodorsen, T., *Theory of Propellers*, McGraw-Hill, New York, 1948

A Detailed Derivation of the Thrust and Power Equations

A.1 Thrust Equation

A cylindrical control volume of infinite radius coaxial with the wake axis is constructed about the propeller and a portion of its wake. Faces 1 and 2 (see fig. 14) are perpendicular to the wake axis and are set far upstream and downstream of the propeller. The thrust produced is then derived from momentum conservation principles applied to this control volume. Momentum conservation requires the rate of change of momentum of a fixed collection of fluid particles to be equal to the net force acting upon the fluid. The net force is composed of the propeller thrust reaction force and the sum of pressure forces acting on the surface of the volume, hence

$$\frac{D}{Dt}\int_{\Sigma'}\rho\vec{v}d\tau = T\vec{k} - \int_{S'}p\vec{n}ds \tag{245}$$

where $\frac{D}{Dt}$ denotes the total or substantial derivative with Σ' denoting a moving control volume and S' denoting a moving control surface accorded to the fixed collection of fluid particles. By Reynold's transport theorem, the substantial derivative can be expressed in terms of integrals over regions Σ and S which are stationary with respect to the far field,

$$\frac{D}{Dt}\int_{\Sigma'}\rho\vec{v}d\tau = \frac{\partial}{\partial t}\int_{\Sigma}\rho\vec{v}d\tau + \int_{S}\rho\vec{v} < \vec{v}\circ\vec{n} > ds \tag{246}$$

The application of Reynold's transport theorem to equation 245 for axial momentum balance yields

$$\frac{\partial}{\partial t}\int_{\Sigma}\rho v_z d\tau + \int_{S}\rho v_z < \vec{v}\circ\vec{n} > ds = T - \int_{S}p < \vec{n}\circ\vec{k} > ds \tag{247}$$

Each constituent integral of 247 is evaluated with reference to figure 14:

1. The first term represents the rate of increase of axial momentum within the fixed volume Σ. Momentum increase is caused by the rate of elongation of the contained wake due to the flight speed of the propeller. In a differential time period one has the increase in momentum,

$$dm_z = V dt\int_{2.}\rho v_z ds \tag{248}$$

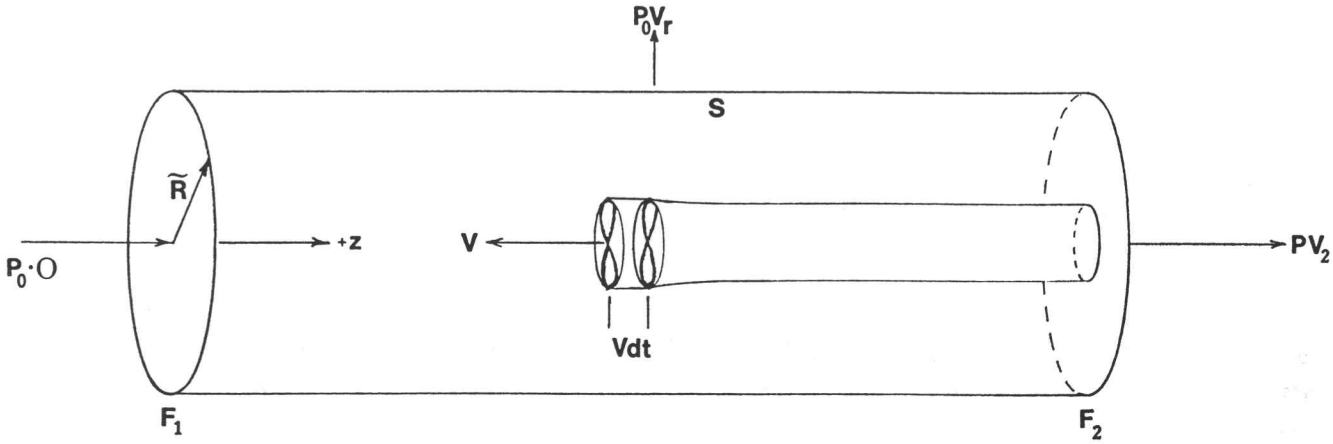

Figure 14: Infinite Control Volume Containing Propeller and Wake

Thus, the integral becomes

$$\frac{\partial}{\partial t}\int_{\Sigma}\rho v_z d\tau = \int_{2.}\rho V v_z ds \tag{249}$$

2. The second integral represents the axial momentum flux out of the control volume over region 2 which is given by

$$\int_S \rho v_z < \vec{v} \circ \vec{n} > ds = \int_{2.}\rho v_z^2 ds \tag{250}$$

3. The final integral becomes

$$\int_S p < \vec{n} \circ \vec{k} > ds = \int_{2.}(p - p_0) ds \tag{251}$$

Consequently, the momentum equation 247 becomes

$$T = \int_{2.}[(p - p_0) + \rho v_z(V + v_z)]ds \tag{252}$$

The unsteady Bernoulli equation (section 3.2) applied to the wake model,

$$(p - p_0) = \rho \underset{\sim}{w} v_z - \frac{1}{2}\rho v^2 \tag{253}$$

substituted into equation 252 finally gives the result

$$T = \rho\int_{2.}[(V + \underset{\sim}{w})v_z + v_z^2 - \frac{1}{2}v^2]ds \tag{254}$$

A.2 Induced Power Loss

The conservation of energy applied to a fixed collection of fluid particles may be stated in the form

$$\frac{D}{Dt}\int_{\Sigma'}\frac{1}{2}\rho v^2 d\tau = \frac{dE}{dt} + \int_{S'}(-p) < \vec{v} \circ \vec{n} > ds \tag{255}$$

where $\frac{dE}{dt}$ represents the rate at which energy is transferred to the slipstream through propeller operation. Again, one obtains the corresponding expression over fixed control regions by Reynold's transport theorem,

$$\frac{dE}{dt} = \frac{\partial}{\partial t}\int_{\Sigma}\frac{1}{2}\rho v^2 d\tau + \int_{S}\frac{1}{2}\rho v^2 < \vec{v} \circ \vec{n} > ds + \int_{S} p < \vec{v} \circ \vec{n} > ds \tag{256}$$

The rate of elongation of the wake within the fixed control volume Σ due to the flight speed of the propeller yields

$$\frac{\partial}{\partial t}\int_{\Sigma}\frac{1}{2}\rho v^2 d\tau = \int_{2.}\frac{1}{2}\rho v^2 V ds \tag{257}$$

and, the rate at which kinetic energy is convected out of the control volume through the surface S is given by

$$\int_{S}\frac{1}{2}\rho v^2 < \vec{v} \circ \vec{n} > ds = \int_{2.}\frac{1}{2}\rho v^2 v_z ds + \int_{3.}\frac{1}{2}\rho v^2 v_r ds \tag{258}$$

However, the product $v^2 v_r$ over surface 3. will decay faster than the circumferencial surface area will increase as the radius approaches infinity; thus, in this limit one has the following,

$$\int_{S}\frac{1}{2}\rho v^2 < \vec{v} \circ \vec{n} > ds \longrightarrow \int_{2.}\frac{1}{2}\rho v^2 v_z ds \tag{259}$$

The term representing work done by the control volume against the external pressure field is expanded,

$$\int_{S} p < \vec{v} \circ \vec{n} > ds = \int_{2.} p v_z ds + \int_{3.} p_0 v_r ds \tag{260}$$

but, continuity demands that

$$\int_{2.} v_z ds + \int_{3.} v_r ds = 0 \tag{261}$$

This requires the following equivalence between work terms:

$$\int_{3.} p_0 v_r ds = -\int_{2.} p_0 v_z ds \tag{262}$$

Substitution of 262 into 260 gives

$$\int_S p < \vec{v} \circ \vec{n} > ds = \int_{2.} (p - p_0) v_z ds \tag{263}$$

Equation 256 then becomes

$$\frac{dE}{dt} = \int_{2.} \{[(p - p_0) + \frac{1}{2}\rho v^2] v_z + \frac{1}{2}\rho v^2 V\} ds \tag{264}$$

With equation 59, the above relation reduces to

$$\frac{dE}{dt} = \int_{2.} [\rho w v_z^2 + \frac{1}{2}\rho v^2 V] ds \tag{265}$$

The first term of the integrand of 265 is given by the definition of the axial kinetic energy loss factor (equation 64). The second term is given by an additional interpretation of the mass coefficient which is derived by the following: The vector identity

$$\nabla \circ (\phi \nabla \phi) = \nabla \phi \circ \nabla \phi + \phi \nabla^2 \phi \tag{266}$$

may be integrated through the volume between adjacent vortex sheets:

$$\int_{\mathcal{V}} \nabla \circ (\phi \nabla \phi) d\tau = \int_{\mathcal{V}} (\nabla \phi)^2 d\tau + \int_{\mathcal{V}} \phi \nabla^2 \phi d\tau \tag{267}$$

where $\mathcal{V}$ is the volume between two adjacent vortex sheets which is enclosed by the surface c; but, within this region one has

$$\nabla^2 \phi = 0 \tag{268}$$

and

$$\vec{v} = \nabla \phi \tag{269}$$

Upon the application of Gauss' theorem one obtains

$$\int_c \phi \frac{\partial \phi}{\partial n} ds = \int_{\mathcal{V}} v^2 d\tau \tag{270}$$

however, the normal flow component at c is given in terms of the displacement velocity

$$\left|\frac{\partial\phi}{\partial n}\right|_c = w\cos\theta \tag{271}$$

where θ is the local pitch angle of the helicoid. Therefore,

$$\int_{\mathcal{V}} v^2 d\tau = w\int_c \phi\cos\theta ds \tag{272}$$

If the surfaces of integration are projected through the angle θ onto the plane $\mathcal{F}$ which is perpendicular to the wake axis, then equation 272 becomes

$$\int_{\mathcal{V}} v^2 d\tau = w\int_{\mathcal{F}} \Gamma ds \tag{273}$$

However, as shown in section 3.1 the mass coefficient is related to the circulation function by

$$w\int_{\mathcal{F}} \Gamma ds = w^2(\kappa A)l \tag{274}$$

Therefore,

$$\rho\int_{\mathcal{V}} v^2 d\tau = \rho w^2(\kappa A)l \tag{275}$$

It can be shown that 275 is equivalent to the relation

$$\rho\int v^2\, ds = \rho w^2(\kappa A) \tag{276}$$

where integration is performed over the Trefftz plane. The propeller may be considered to impart an axial flow velocity equivalent to the displacement velocity on a fluid column with an effective area (in terms of total kinetic energy) κ times the wake area. With the definition of κ from section 3.1, the definition of ϵ from section 3.3 and equation 276, equations 254 and 265 are finally

$$T = \rho\kappa w A[V + w(\frac{1}{2} + \frac{\epsilon}{\kappa})] \tag{277}$$

$$\frac{dE}{dt} = \rho\kappa w^2 A(w\frac{\epsilon}{\kappa} + \frac{1}{2}V) \tag{278}$$

A.3 Total Power (short format suggested by H. S. Ribner)

The algebra for the derivation is simplest if we use a control surface that is stationary with respect to the fluid at infinity; we use a slightly relabeled version of Figure 14, with V being the propeller speed through the fluid:

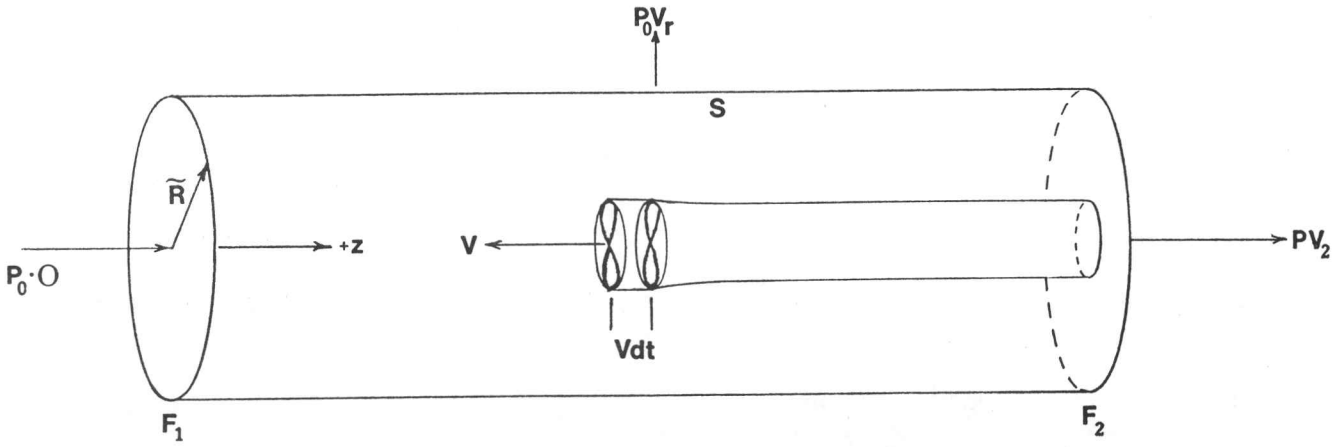

Figure 14a

The pressure does work on the external fluid on faces F_2 and S at a rate

$$\int_S p_o v_r dS + \int_{F_2} p v_z dS \tag{279}$$

By conservation of mass

$$\int_S v_r dS = -\int_{F_2} v_z dS \tag{280}$$

so that (279) becomes

$$\int_{F_2} (p - p_o)v_z dS \tag{281}$$

The wake elongates by an amount $(V + v_z)dt$ in a time dt. Thus the rate of increase of kinetic energy of the fluid is

$$\frac{1}{2}\rho \int_{F_2} v^2(V + v_z)dS \tag{282}$$

The rate of energy lost to the fluid owing to propeller operation, dE/dt, is the sum of (281) and (282). This loss plus the useful power TV is the total (ideal) power P consumed by the propeller. Using the form (252) for T gives after slight reduction

$$P = \int_{F_2} \left[(p - p_o) + \rho\left(\frac{1}{2}v^2 + Vv_z\right)\right](V + v_z)dS \tag{283}$$

The pressure term may be eliminated via the relation

$$p - p_o = \rho \frac{w}{2} v_z - \frac{1}{2}\rho v^2 \tag{59), (253}$$

which results (Sec. 3.2) from application of the unsteady Bernoulli's equation. The $\frac{1}{2}\rho v^2$ term cancels to yield, after a little rearrangement, the final result[16,17]

$$P = \rho \int_{F_2} (V + \frac{w}{2})(Vv_z + v_z^2)dS \tag{284}$$

B Brief Description of the Vector Processing Concept

Vector processing is one of the high performance cornerstones of the Cray X-MP/24 system. All processing of data within the CPU (central processing unit) or transfer of data to and from central memory is coordinated by the system clock. The shortest time interval between changes in machine state is one clock period, which is equal to the reciprocal of the clock signal frequency. For conventional computers, fundamental computations such as multiplies, adds etc., or the transfer of data can occur only once every few clock periods. However, vector architecture permits certain mathematical operations to be performed at a rate of one result per clock period. As an example, consider an addition of a set of numeric pairs. The set of numbers are considered to be processed in a scalar fashion if each pair of operands is read from memory to an add unit of the CPU, processed by the add unit over six clock periods, and stored back into central memory in a sequential fashion. However, if the add functional unit is segmented into six independent sub-units, each performing one sixth of the necessary operations in parallel, then after 6 clock cycles the segmented add unit can produce a result once every clock period. Since conventional memory cannot supply operands at a rate of one per clock period, special registers of high speed memory containing 64 words (1 word=64 bits) are employed. In the case of the above example, two such registers are loaded from main memory. Then, the contents of these registers is processed through a fully segmented functional add unit at the rate of one per clock period. Because of the fashion in which data is processed, this procedure is referred to as vectorization: the data is first collected then processed as a group at very high speed. A set of operands can be processed under vectorization up to 10 times faster than what is possible with scalar processing.

Any quadrature algorithm will evaluate an integrand at a certain number of points within the domain of integration. Off-the-shelf quadrature packages evaluate quadrature points by way of calls to a user supplied sub-program: code execution is transferred to a sub-program once for every quadrature point. However, this process excludes any hope of vectorization.

C Goldstein Circulation Data with Code Generated Values

x	K_{100}	Goldstein	rel. diff	xK_{100}
.02	.1255	.126	.40%	.0025
.04	.2442	.245	.33	.0098
.06	.3514	.352	.17	.0211
.08	.4449	.445	.02	.0356
.10	.5249	.526	.21	.0525
.12	.5926	.593	.07	.0711
.14	.6496	.650	.06	.0909
.16	.6976	.698	.06	.1116
.18	.7379	.738	.01	.1328
.20	.7720	.770	—	.1544
.25	.8363	.836	-.04	.2091
.30	.8794	.878	-.16	.2638
.35	.9088	.908	-.09	.3181
.40	.9290	.927	-.22	.3716
.45	.9428	.940	-.30	.4243
.50	.9517	.950	-.18	.4759
.60	.9574	.955	-.25	.5744
.70	.9438	.941	-.30	.6607
.80	.8919	.890	-.21	.7135
.90	.7427	.738	-.63	.6684
.95	.5758	.569	-1.2	.5470
.98	.3948	.388	-1.7	.3869

Table 9: Code generated values vs. Goldstein data, $\lambda_t = 0.10, B = 2$

x	K_{100}	Goldstein	rel. diff	xK_{100}
.05	.1196	.120	.33%	.0060
.10	.2320	.232	—	.0232
.15	.3324	.331	-.42	.0499
.20	.4185	.418	-.12	.0837
.25	.4901	.489	-.22	.1225
.30	.5482	.548	-.04	.1645
.35	.5943	.592	-.39	.2080
.40	.6296	.628	-.25	.2518
.45	.6553	.654	-.20	.2949
.50	.6720	.670	-.30	.3360
.625	.6772	.676	-.18	.4233
.75	.6264	.621	-.86	.4698
.875	.4949	.486	-1.8	.4330
.95	.3363	.334	-.68	.3195

Table 10: Code generated values vs. Goldstein data, $\lambda_t = 0.25, B = 2$

APPENDIX D

WAKE CONTRACTION AND DISPLACEMENT VELOCITY FOR HEAVY LOADING: AN ALTERNATIVE DERIVATION AT $\lambda_T = 0$ INVOKING DETAILS OF THE AERODYNAMICS

by H. S. Ribner

Theodorsen's treatment of the contraction R_∞/R, as has been pointed out, is deliberately restricted to the light loading case by the a priori specification $\bar{w} << 1$. It is not clear why this was done, since it seems unnecessary. With this in mind, his derivation of $(R_\infty/R)^2$ is carried through in the main text without this restriction. The result, Eq. (200), is more broadly applicable than Theodorsen's (Ref. 17, p. 84, fourth equation from top*): the displacement velocity taken as $\frac{1}{2}\bar{w}$ is replaced in two places by the more general value $\overline{a_0}$, which reduces to $\frac{1}{2}\bar{w}$ for $\bar{w} \to 0$.

The computed contraction is expressed in coefficient form as:

$$\hat{Y} \equiv \frac{1}{2\overline{w}}\left(\frac{\Delta R}{R}\right); \quad \Delta R = R - R_\infty \qquad (209), (215)$$

for comparison with Theodorsen's limiting result for light loading†

$$Y = \frac{1}{2\overline{w}}\left(\frac{\Delta R}{R}\right)_{\overline{w}<<1} = \frac{1}{4}\left(\frac{\varepsilon}{\kappa} - \frac{1}{2}S\right) \qquad (208)$$

where S is an integral defined by Eq. (199) of the main text.

---

* This expression contains a typo inversion. A/F should be replaced by $F/A = \pi R_\infty^2/\pi R^2$.

† Here we eliminate the unnecessary small $\bar{w}$ approximation, $2\bar{w} \simeq c_S/\kappa$ in his definition of Y.

Whereas (for a given number of blades, B) his Y is displayed as a *single* curve vs. λ_T, the generalized contraction coefficient $\hat{Y}$ is displayed (Figs. 47-55) as a *family* of curves for various values of $\bar{w}$.

Compared with Theodorsen's single curve for $\bar{w} \to 0$, the Theodorsen-based family of curves $\hat{Y}$ vs. (λ_T; $\bar{w}$) exhibits two features: *(i) the curves are lower** with increasing $\bar{w}$, and (ii) at the higher $\bar{w}$ and λ_T, some dip slightly below zero: this implies a (weak) expansion rather than a contraction.* The explanation of (ii) involves aerodynamic assumptions that are difficult to prove. However, (i) is accessible to verification *at the $\lambda_T = 0$ limit.* This allows us, in what follows, to apply simple conservation of mass to the flow within the helicoid wake.

D.1 Wake Contraction by Continuity Argument. Advance $\lambda_T = 0$

It is difficult, as pointed out in Section 7.1, to apply mass continuity to determine the wake contraction in the general case. However, as the pitch ($\propto\lambda_T$) of the helicoid surface approaches zero the turns become nearly circular and closely packed. The fluid between the turns is essentially "trapped" and shares the displacement velocity of the surface (except for a small zone near the edges). This uniform velocity is a_o at the propeller plane (radius R) and w far back (radius R_∞). On adding the stream velocity V, simple mass continuity yields

$$\frac{\pi R_\infty^2}{\pi R^2} = \frac{V + a_o}{V + w} = \frac{1 + \bar{a}_o}{1 + \bar{w}}; \quad \bar{a}_o = a_o/V, \quad \bar{w} = w/V \tag{285}$$

** This implies that, for a fixed advance λ_T, the curve of $\Delta R/R$ ($=2\bar{w}\hat{Y}$) vs. $\bar{w}$ is nonlinear: it curves markedly downward from its tangent at the origin (the Theodorsen $\bar{w} \to 0$ straight line).

Theodorsen's expression for $\bar{a}_0$, Eq. (205), may be rearranged in the form

$$1 + \bar{a}_o = \frac{1 + \bar{w} + \frac{\varepsilon}{\kappa}(\bar{w} + \bar{w}^2)}{1 + \bar{w}\left(\frac{1}{2} + \frac{\varepsilon}{\kappa}\right)} \tag{286}$$

Since $\varepsilon/\kappa \rightarrow 1$, this reduces to

$$1 + \bar{a}_o = \frac{(1 + \bar{w})^2}{1 + \frac{3}{2}\bar{w}} \quad \text{at } \lambda_T = 0 \tag{287}$$

so that

$$\left(\frac{R_\infty}{R}\right)^2 = \frac{1 + \bar{w}}{1 + \frac{3}{2}\bar{w}}, \quad \text{at } \lambda_T = 0 \tag{288}$$

The general contraction equation obtained by Theodorsen's methods (but with his restriction to $\bar{w} << 1$ removed), reads

$$\left(\frac{R_\infty}{R}\right)_T^2 = \frac{(1 + \bar{w})(1 + \bar{a}_o S)}{(1 + \bar{a}_o)\left[1 + \bar{w}\left(\frac{1}{2} + \frac{\varepsilon}{\kappa}\right)\right]} \tag{200}$$

Since the parameter S (see text, Eq. (199)) and ε/κ both $\rightarrow 1$ as $\lambda_T \rightarrow 0$, this reduces to

$$\left(\frac{R_\infty}{R}\right)_T^2 = \frac{1 + \bar{w}}{1 + \frac{3}{2}\bar{w}} \quad \text{at } \lambda_T = 0 \tag{289}$$

in exact agreement with Eq. (288). Thus at vanishing advance coefficient the simple continuity argument and Theodorsen's deduction from thrust

considerations give identical results. And both confirm observation (i) made in the last paragraph of the introduction to this section.

D.2 Displacement Velocity a_o at Propeller Plane vs. $\bar{w}$. Advance $\lambda_T = 0$

For finite displacement velocity, the turns of the wake (multiple) helicoid are more crowded (smaller pitch) near the propeller plane than far back (Trefftz plane, $z = \infty$). This follows from the displacement velocity increasing from a_o (of order $\frac{1}{2}w$) to w with increasing axial distance.* Accordingly, the spacing L between turns scales as

$$\frac{L_o}{L} = \frac{V + a_o}{V + w} = \frac{1 + \bar{a}_o}{1 + \bar{w}} ; \quad \bar{w} = \frac{w}{V}, \text{ etc.} \tag{290}$$

In the light loading limit ($\bar{w} \to 0$), L/L_o approaches unity, and the turns are uniformly spaced. In this case a simple symmetry argument applied to the helicoid yields $\bar{a}_o = \frac{1}{2}\bar{w}$. For finite $\bar{w}$ the varying spacing invalidates this argument, and it accounts for $\bar{a}_o \neq \frac{1}{2}\bar{w}$.

For evaluation of $\bar{a}_o$ we must determine L_o/L independently of Eq. (290). For arbitrary advance λ_T this is difficult, so we limit attention to the case $\lambda_T \to 0$. For this case the propeller circulation along the blade is uniform, of value γ, say. Then the tip vortices shed to constitute the helicoid wake have the same value. A cut through these vortices in the wake diametral plane appears as in the sketch, showing the contraction ΔR:

---

* This applies a little beyond the propeller blade trailing edge, where the short-range induced velocities of the bound vortices have become negligible.

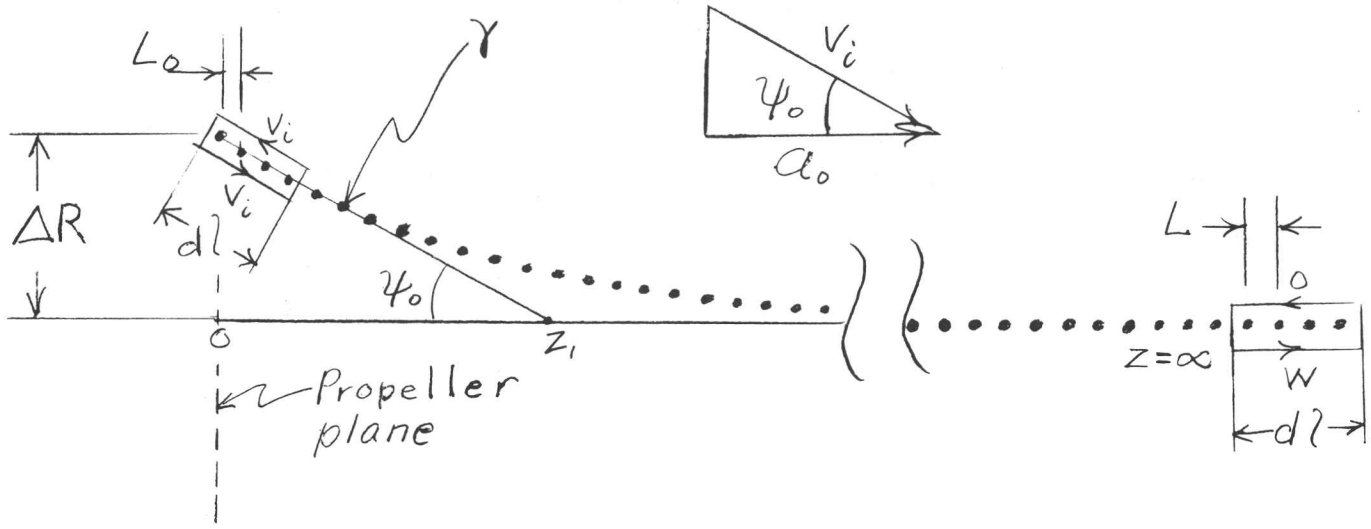

Suppose there are n_o turns in a length $d\ell$ at z = 0 and n turns far back:

$$n_o = d\ell \cos \psi_o / L_o \tag{291}$$

$$n = d\ell / L_o \tag{292}$$

The maximum velocity v_i induced by the sheet of edge vortices must lie along the sheet. Since the axial component is a_o by definition,

$$a_o = v_i \cos \psi_o \tag{293}$$

where ψ_o is the initial slope of the contraction flare. By Ampere's law applied to circuits (1) and (2):

$$\Gamma_o = \int_{(1)} \underline{v}_i \cdot \underline{d\ell} = d\ell \, 2a_o / \cos \psi_o \tag{294}$$

$$\Gamma = \int_{(2)} \underline{v}_i \cdot d\underline{\ell} = d\ell\, w \tag{295}$$

(The contribution of the stream velocity (not shown) = 0.) Since each vortex has strength γ, it is also true that

$$\Gamma_o = n_o\gamma = \gamma d\ell \cos\psi_o/L_o \tag{296}$$

$$\Gamma = n\gamma = \gamma d\ell/L \tag{297}$$

Equating the alternative expressions for the ratio Γ_o/Γ from the last four equations yields

$$\frac{L_o}{L} = \frac{w\cos^2\psi_o}{2a_o} = \frac{\overline{w}\cos^2\psi_o}{2\overline{a}_o} \tag{298}$$

This and the earlier Eq. (290) are alternative expressions for L_o/L; equating and rearranging gives the quadratic

$$2\overline{a}_o^2 + 2\overline{a}_o - \overline{w}(1+\overline{w})\cos^2\psi_o = 0 \tag{299}$$

A formal solution for $\overline{a}_o$ is thus

$$\overline{a}_o = -\frac{1}{2} + \frac{1}{2}\sqrt{1 + 2\overline{w}(1+\overline{w})\cos^2\psi_o} \tag{300}$$

This result applies, by the terms of the derivation, at the $\lambda_T = 0$ limit.

For comparison, Theodorsen's general result for arbitrary advance, Eq. (205), reduces at $\lambda_T = 0$ to

$$\bar{a}_o = \frac{\bar{w}\left(\frac{1}{2} + \bar{w}\right)}{1 + \frac{3}{2}\bar{w}} \tag{301}$$

These two expressions are compared in the following sections.

First Approximation: Wake Flare (~Contraction) Ignored

If the wake contraction had been ignored at the outset ($\psi_o = 0$), the derivation would have been noticeably simplified, with the quick result

$$\bar{a}_o = -\frac{1}{2} + \frac{1}{2}\sqrt{1 + 2\bar{w}(1 + \bar{w})} \tag{302}$$

This is obtained alternatively by letting $\cos^2\psi_o = 1$ in Eq. (300). Table I below shows numerical comparisons of predictions of Eq. (301) of Theodorsen (our extended form) and Eq. (302) above.

Table I

$\bar{a}_o/\bar{w}$

$\bar{w}$	Eq. (302)	Eq. (301)	% Error
.0	.500	.500	0
.5	.581	.571	+1.8
1.0	.618	.600	+3.0
1.5	.638	.611	+3.7
2.0	.651	.625	+4.2

$\psi_o = 0, \quad \lambda_T = 0$

This simplistic approach neglecting ψ_o already gives agreement with Theodorsen's results for $\lambda_T = 0$ within a few percent.

Second Approximation: Wake Flare Angle ψ_o Estimated

Theodorsen[17] computed and plotted the shape of the helicoid contraction flare for several cases (his Fig. 28, a-d). We can infer that the tip tangent scales with ΔR, so that

$$\tan \psi_o = \frac{\Delta R}{z_1} = \frac{\Delta R/R}{z_1/R}, \tag{303}$$

where z_1/R does not depend on $\bar{w}$. The curves show slight or no dependence on blade number B for small λ_T; they give z_1/R of order 0.6 for $\lambda_T = 1/4$, with progressive *increase* for larger λ_T. For our case, $\lambda_T = 0$, a still smaller value of z_1/R seems implied. In (285) we have effectively evaluated $\Delta R/R$ at $\lambda_T = 0$ as

$$\Delta R/R = 1 - \sqrt{(1 + \bar{w})/\left(1 + \tfrac{3}{2}\bar{w}\right)} \tag{304}$$

and we assume here that

$$z_1/R = 0.52 \tag{305}$$

Insertion in Eq. (303) determines the value of ψ_o to be used in Eq. (300); this will yield predictions of $\bar{a}_o/\bar{w}$ vs. $\bar{w}$ by the present method. In the following table these predictions are compared with those by Theodorsen's "exact" formula Eq. (301).

Table II

$\bar{a}/\bar{w}$

$\bar{w}$	This Appendix Eq. (300)	Theodorsen/Foster Eq. (301)
0	.5000	.5000
.5	.5717	.5714
1.0	.6002	.6000
1.5	.6155	.6154
2.0	.6251	.6250

We recall that the choice $z_1/R = \infty$ (Table I), which implies $\psi_o = 0$, yields a maximum error of only 4.2% at $\bar{w} = 2$. The empirical but realistic choice $z_1/R = 0.52$ (Table II) reduces the error consistently to the fourth decimal place. From the internal logic and this agreement one would infer that the present aerodynamic model is essentially correct.

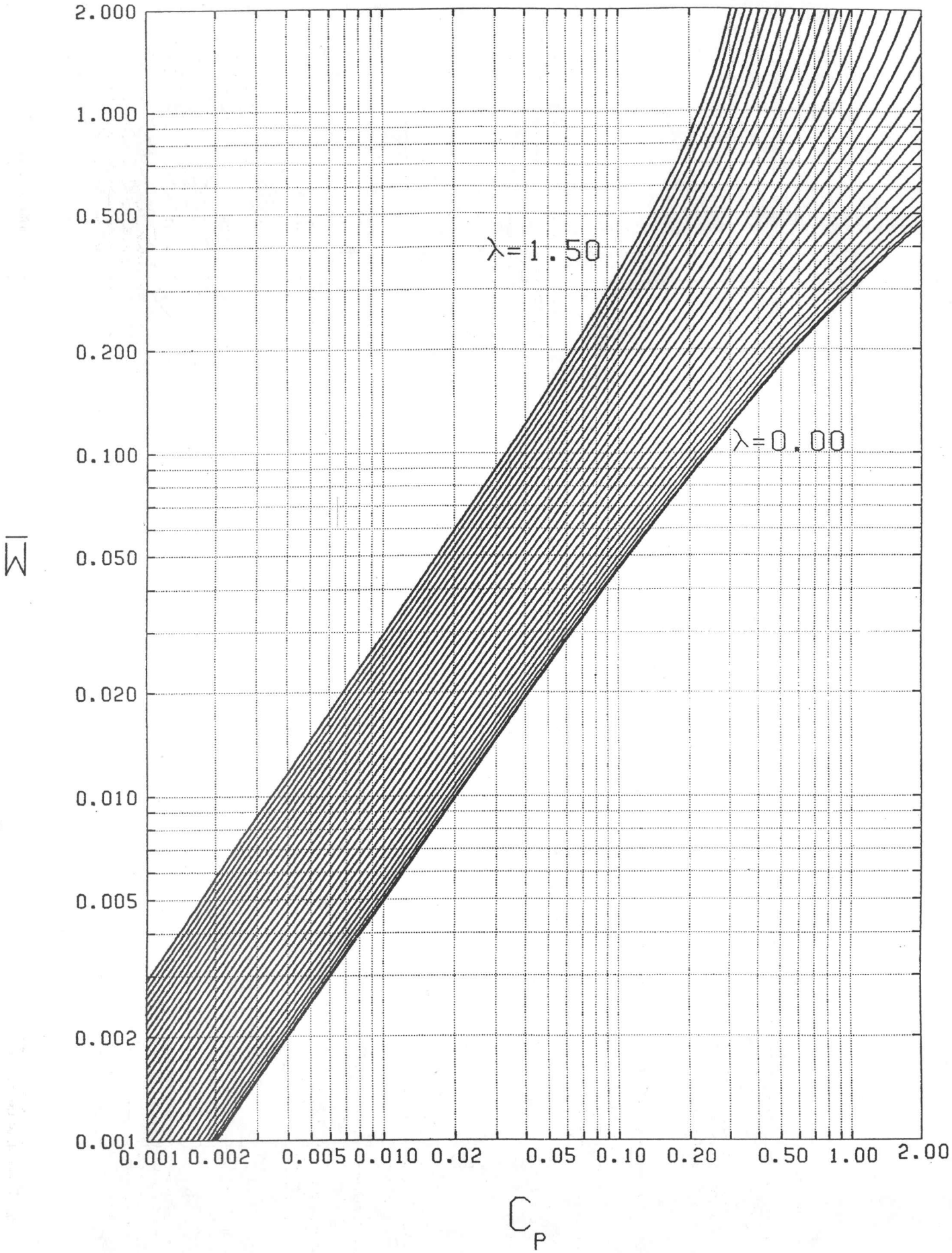

FIG. 64 DISPLACEMENT VELOCITY AT CONSTANT $\lambda = V/\pi n D_\infty$
INFINITE BLADE NUMBER

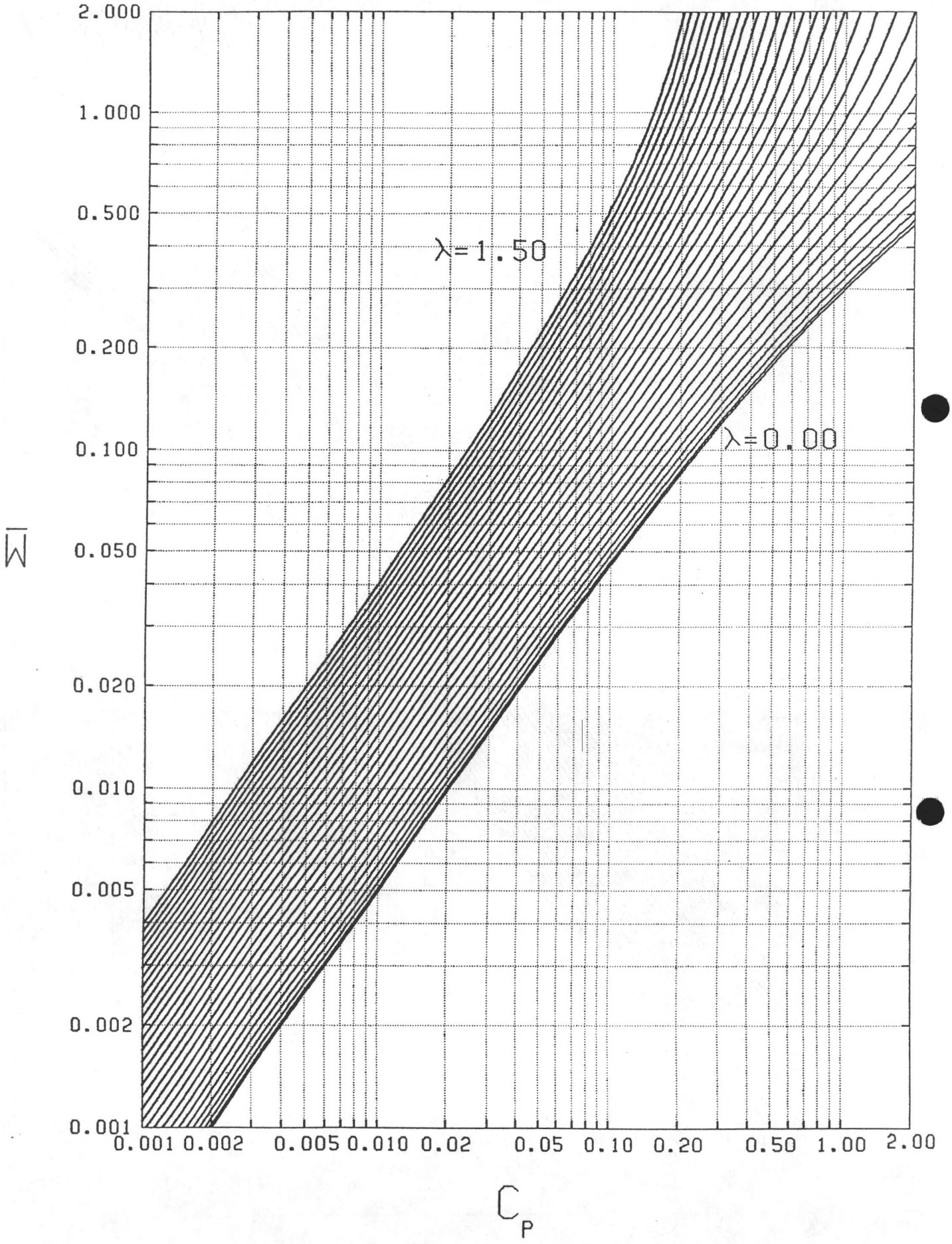

FIG. 63 DISPLACEMENT VELOCITY AT CONSTANT $\lambda = V/\pi n D_\infty$
TWELVE-BLADE PROPELLER

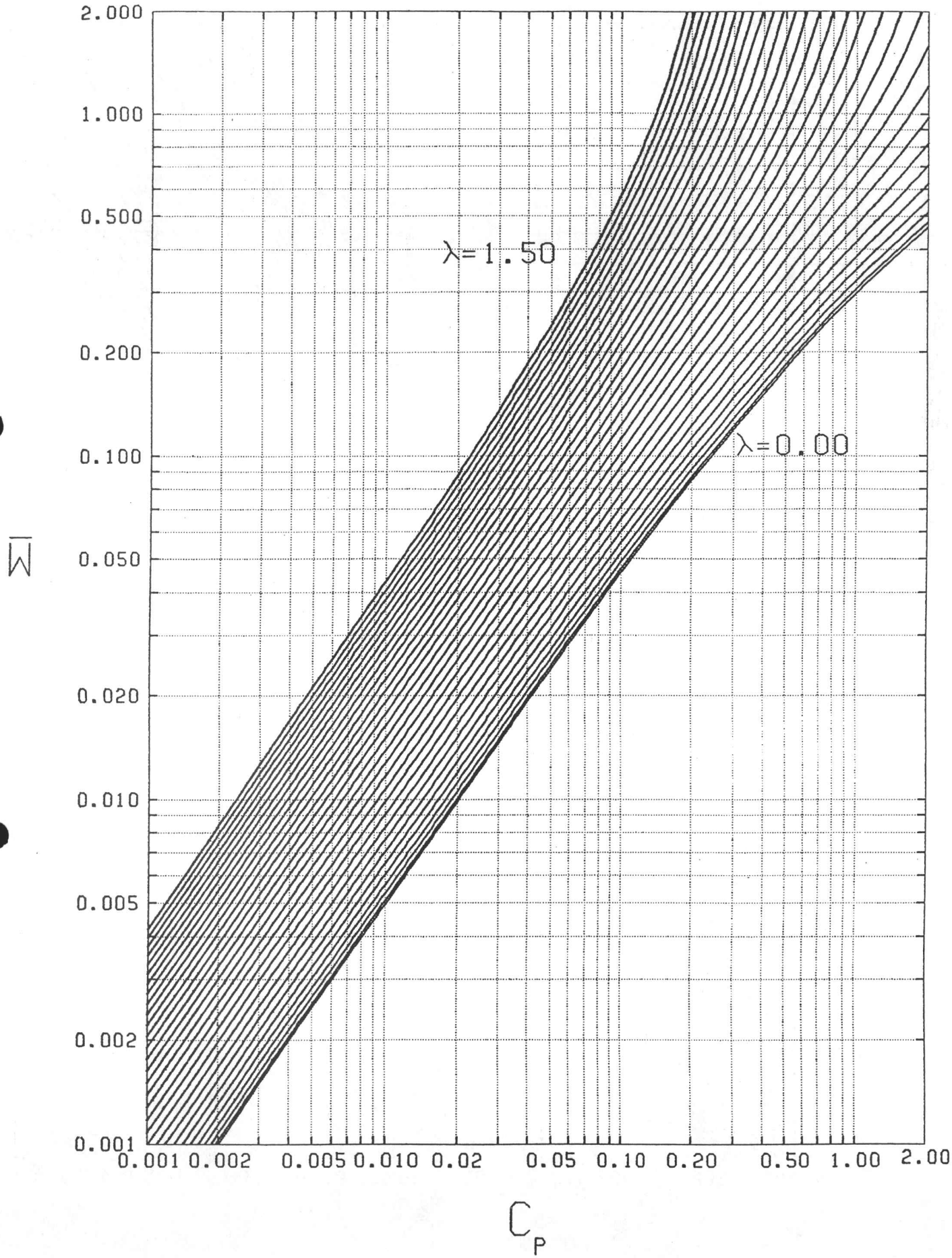

FIG. 62 DISPLACEMENT VELOCITY AT CONSTANT $\lambda = V/\pi n D_\infty$
TEN-BLADE PROPELLER

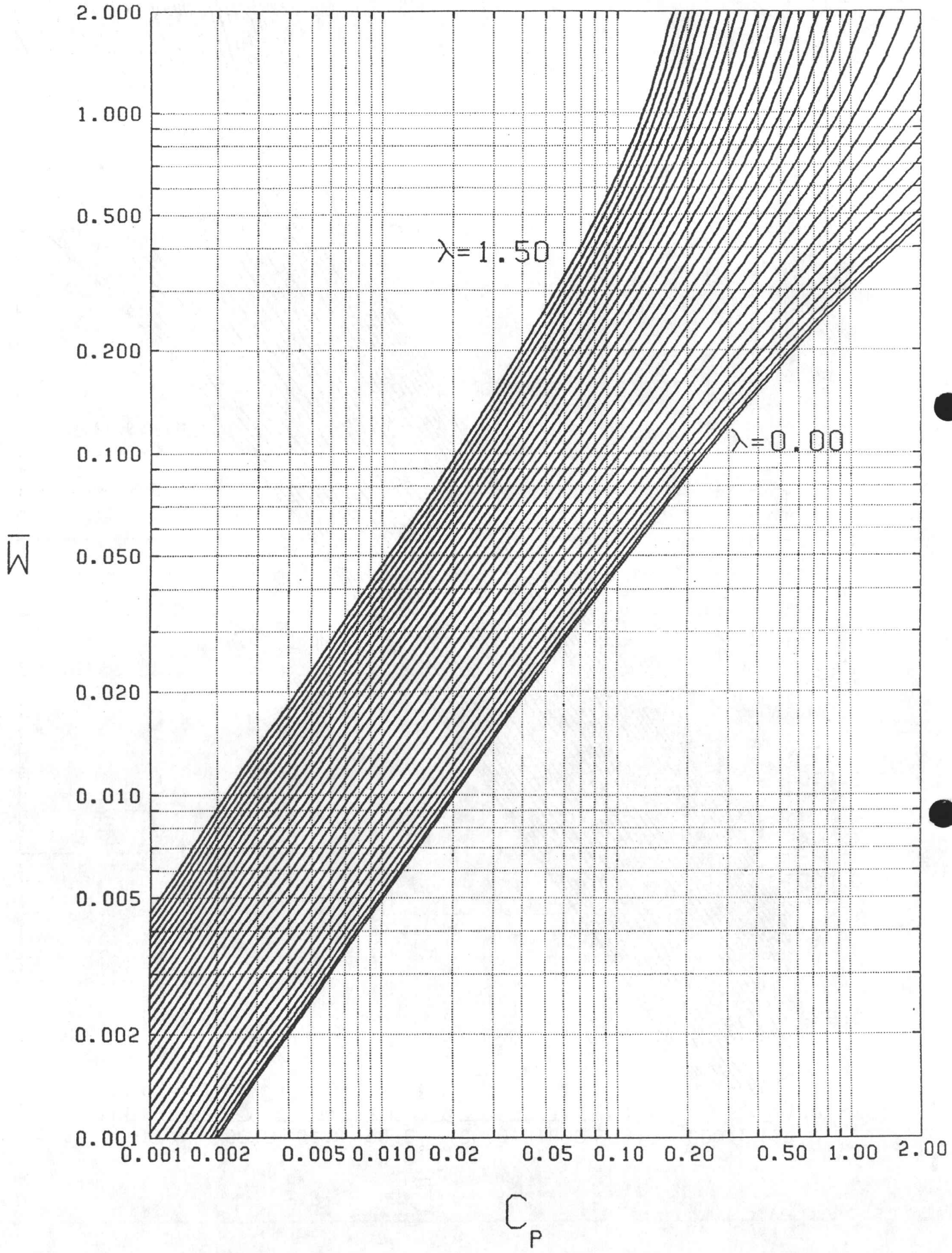

FIG. 61 DISPLACEMENT VELOCITY AT CONSTANT $\lambda = V/\pi n D_\infty$
EIGHT-BLADE PROPELLER

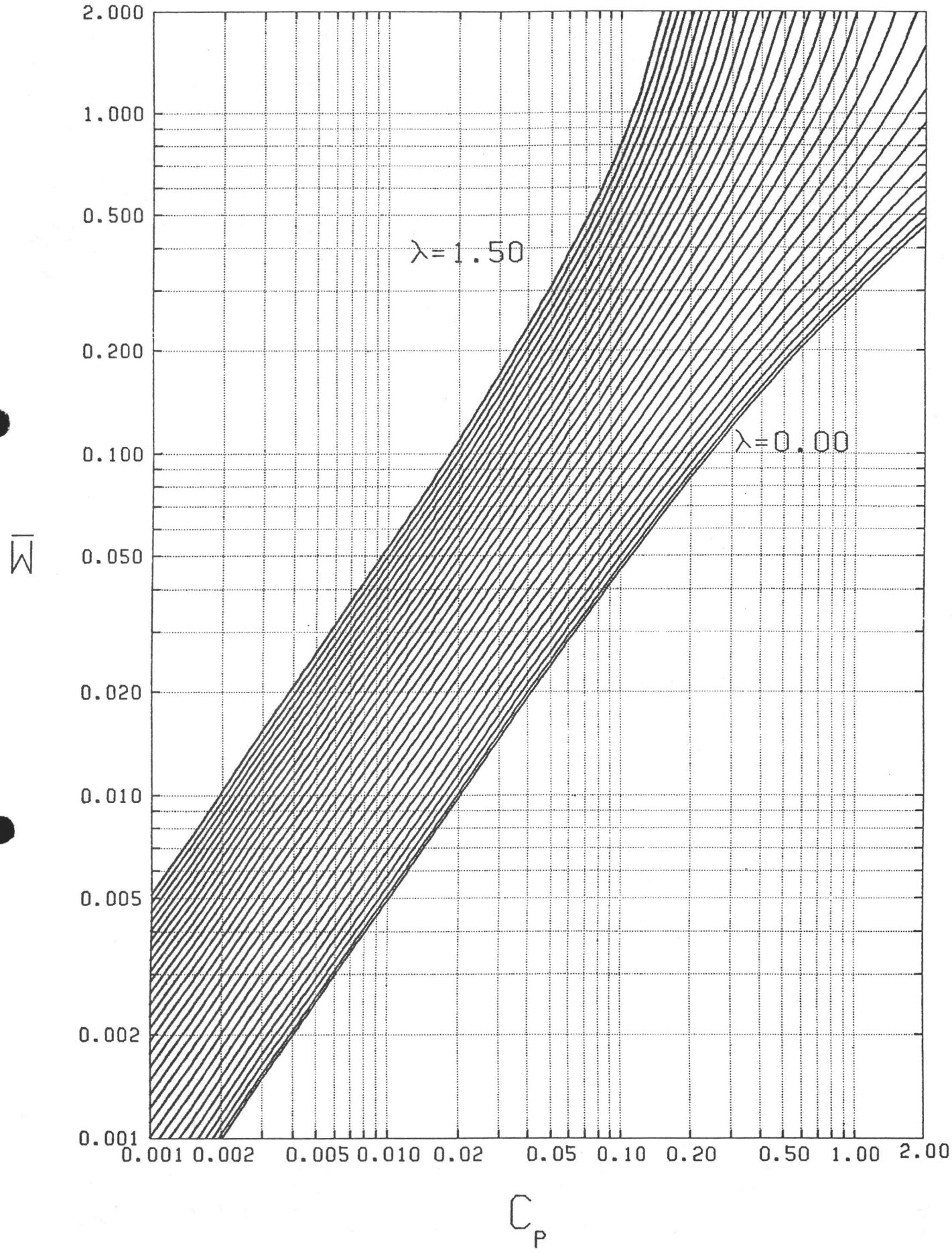

FIG. 60 DISPLACEMENT VELOCITY AT CONSTANT $\lambda = V/\pi n D_\infty$
SIX-BLADE PROPELLER

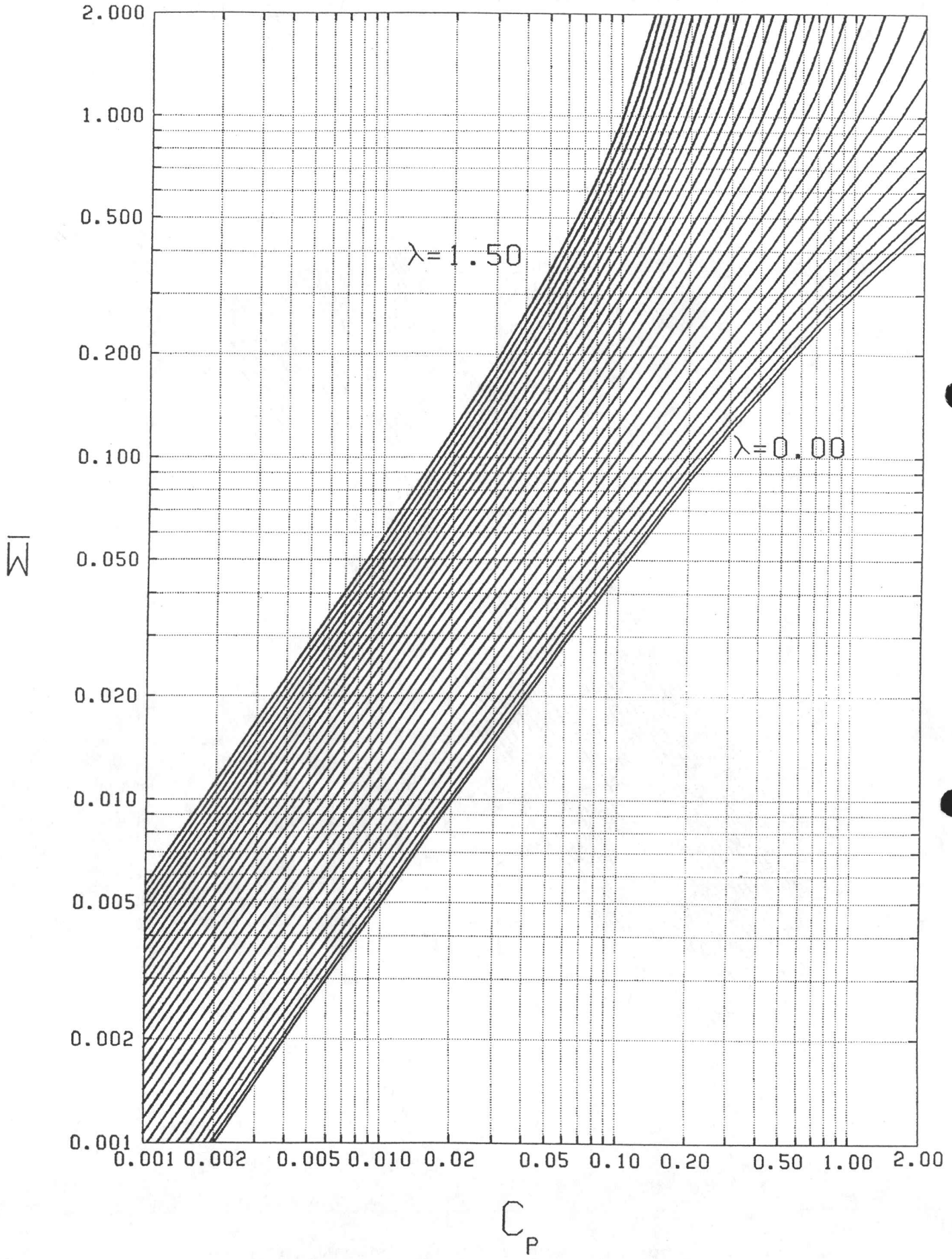

FIG. 59 DISPLACEMENT VELOCITY AT CONSTANT $\lambda = V/\pi n D_\infty$
FIVE-BLADE PROPELLER

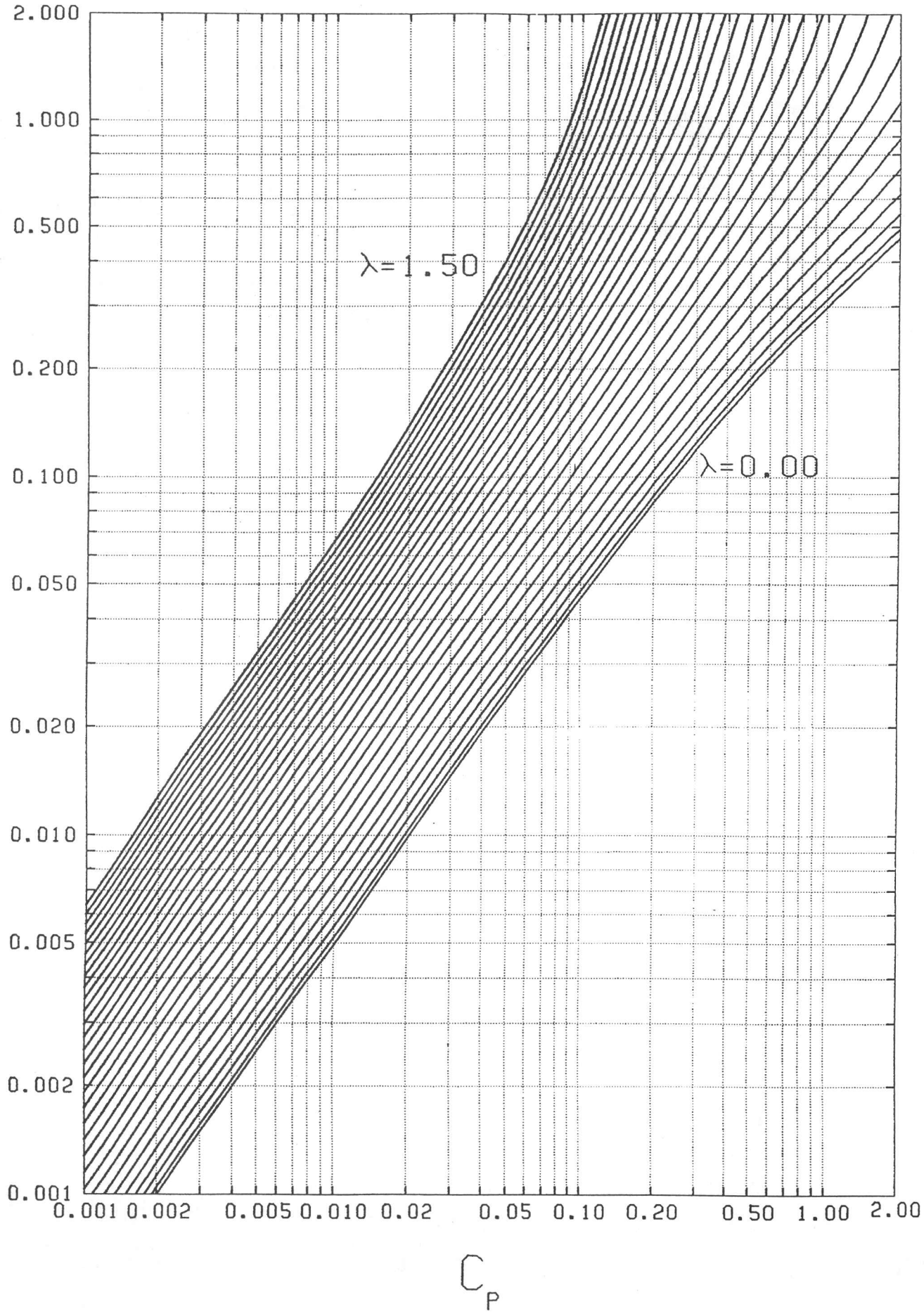

FIG. 58 DISPLACEMENT VELOCITY AT CONSTANT $\lambda = V/\pi n D_\infty$
FOUR BLADE PROPELLER

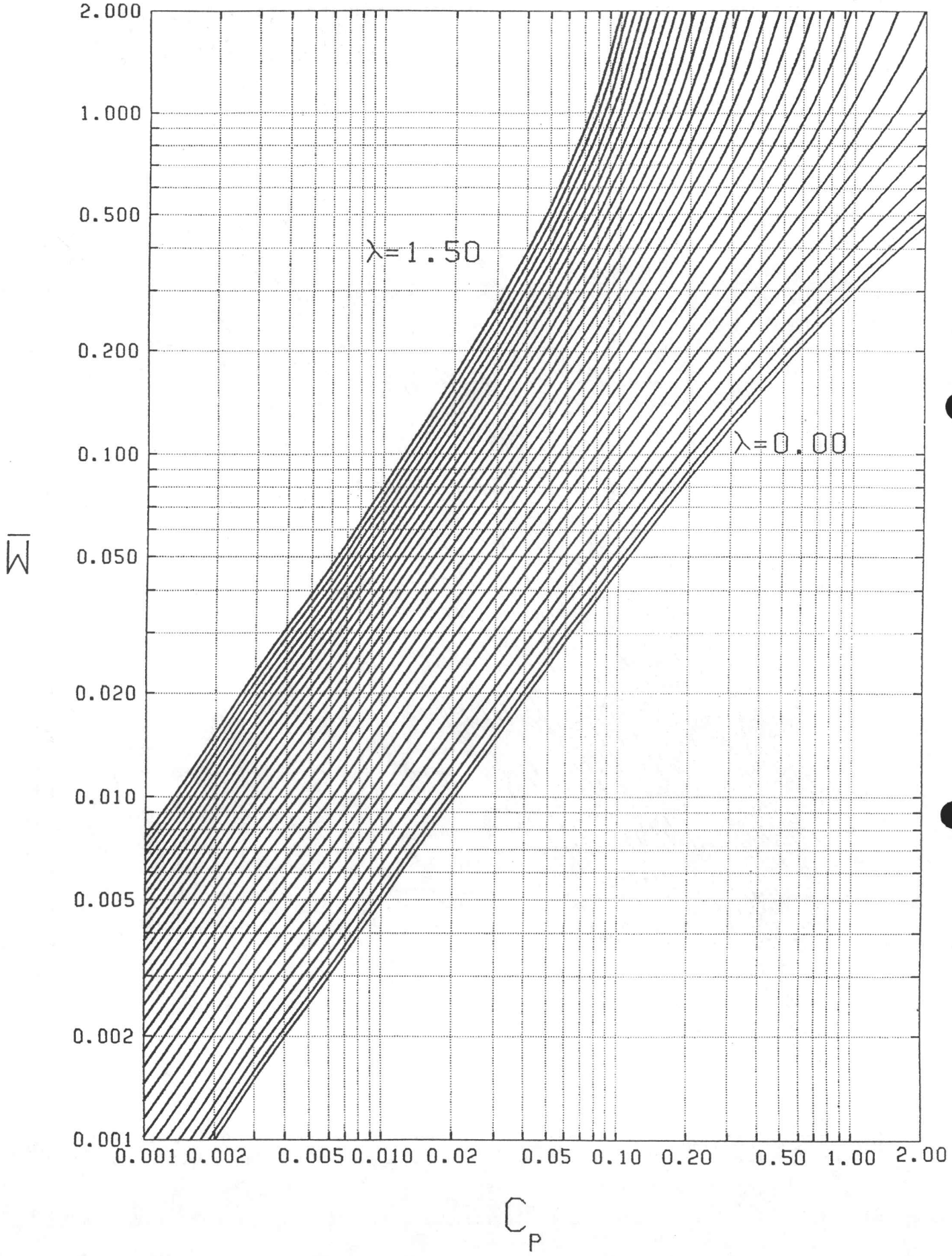

FIG. 57 DISPLACEMENT VELOCITY AT CONSTANT $\lambda = V/\pi n D_\infty$
THREE-BLADE PROPELLER

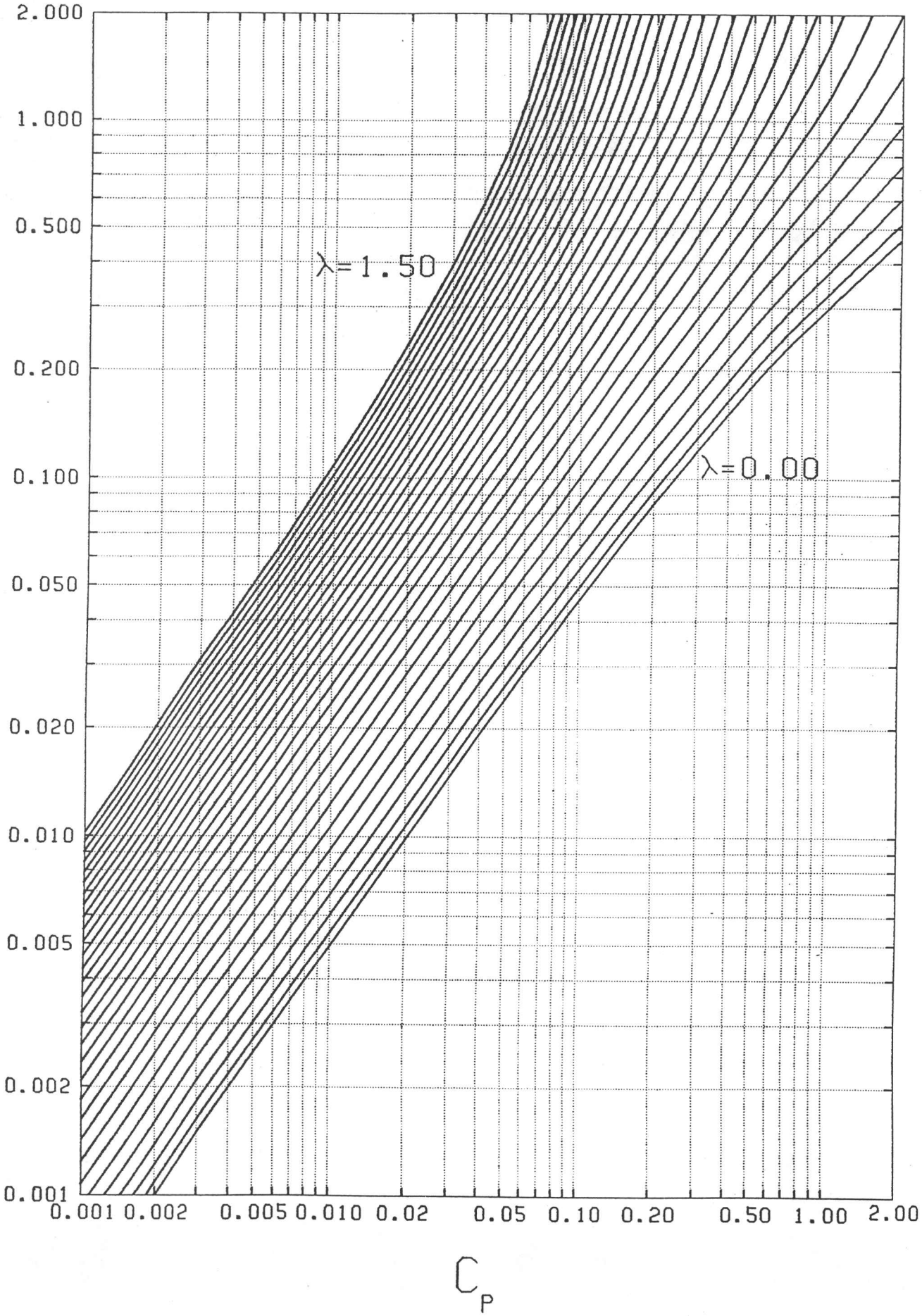

FIG. 56 DISPLACEMENT VELOCITY AT CONSTANT $\lambda = V/\pi n D_\infty$
TWO-BLADE PROPELLER

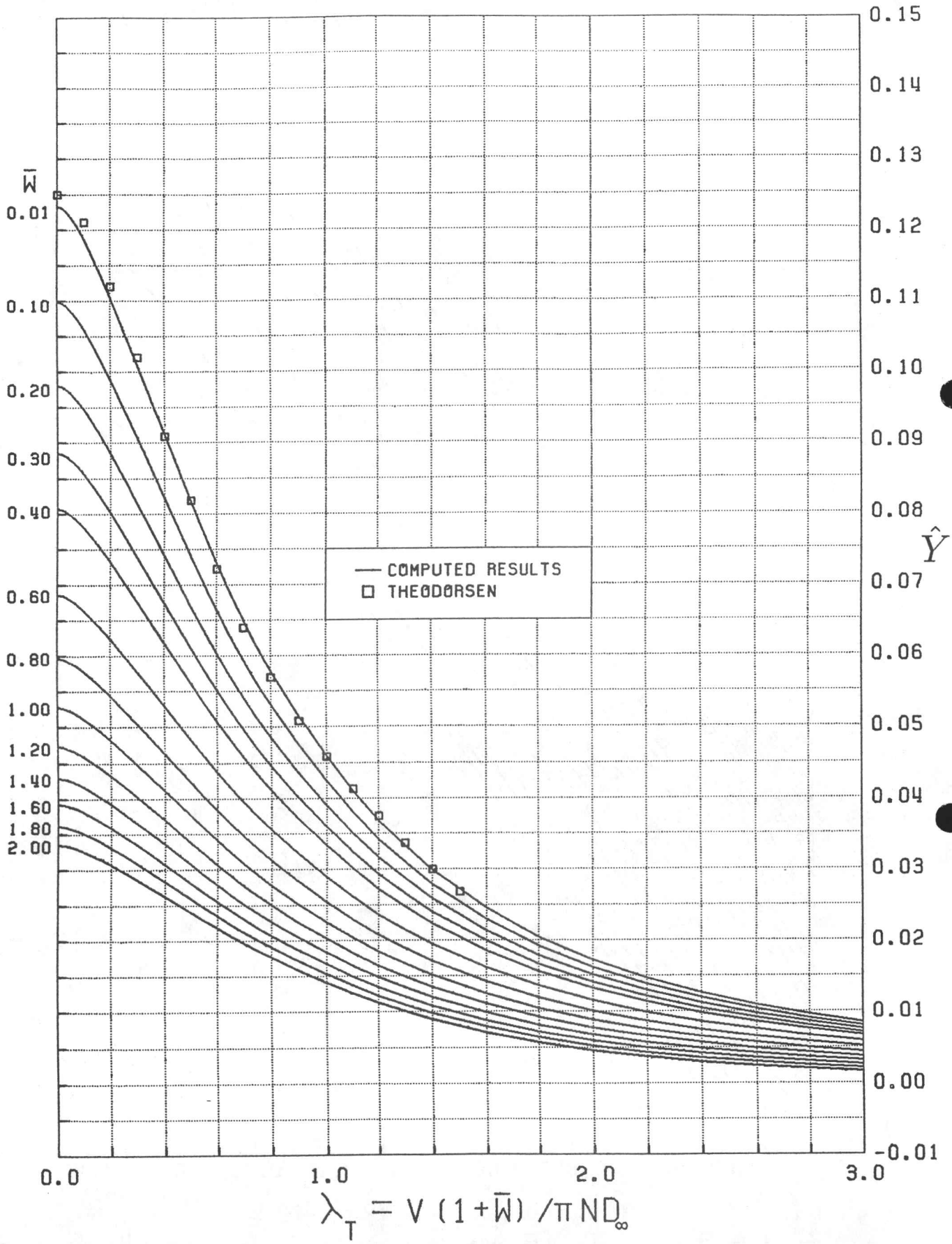

FIG. 55 CONTRACTION COEFFICIENT AT CONSTANT $\bar{w}$
INFINITE BLADE NUMBER

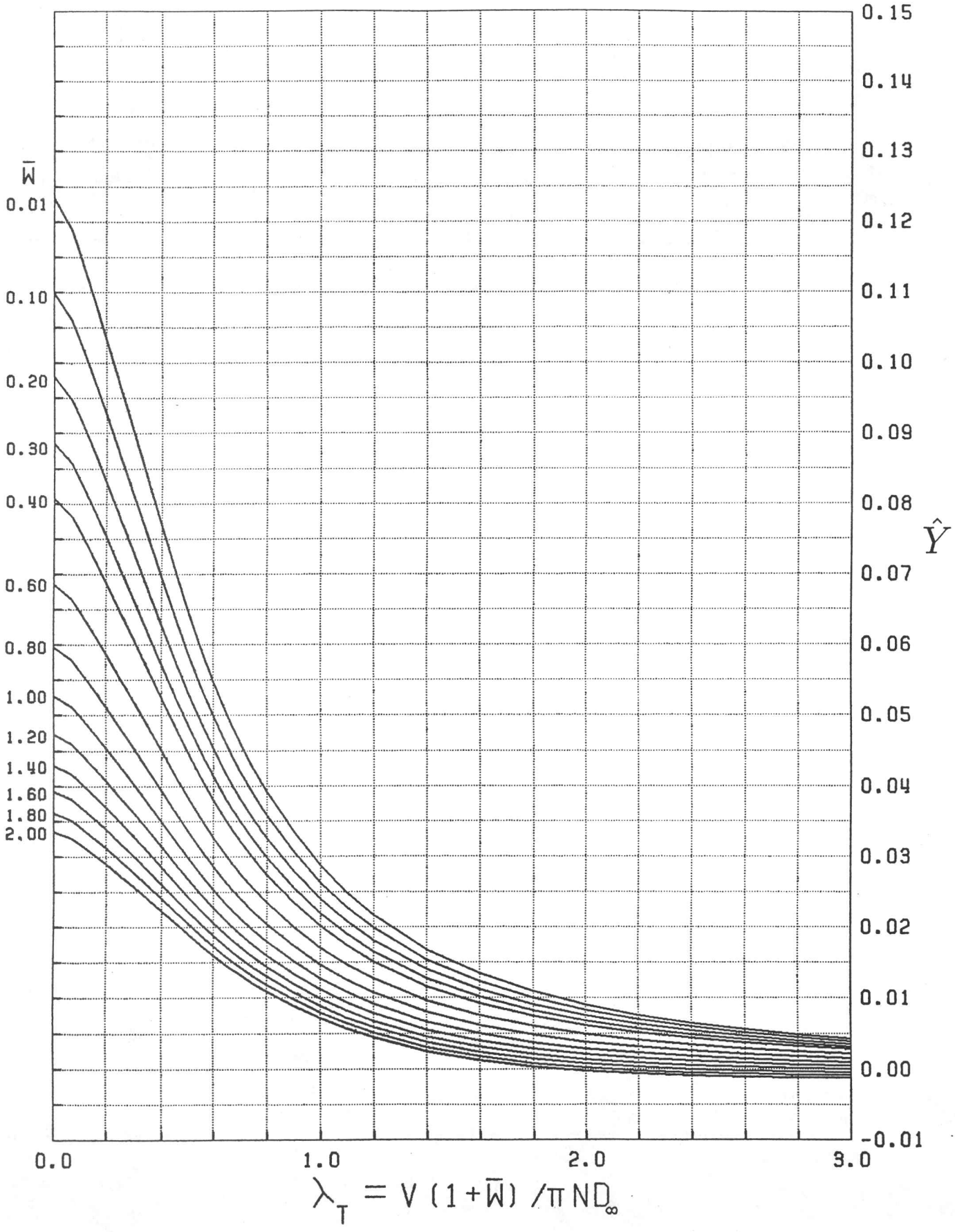

FIG. 54 CONTRACTION COEFFICIENT AT CONSTANT $\bar{w}$
TWELVE-BLADE PROPELLER

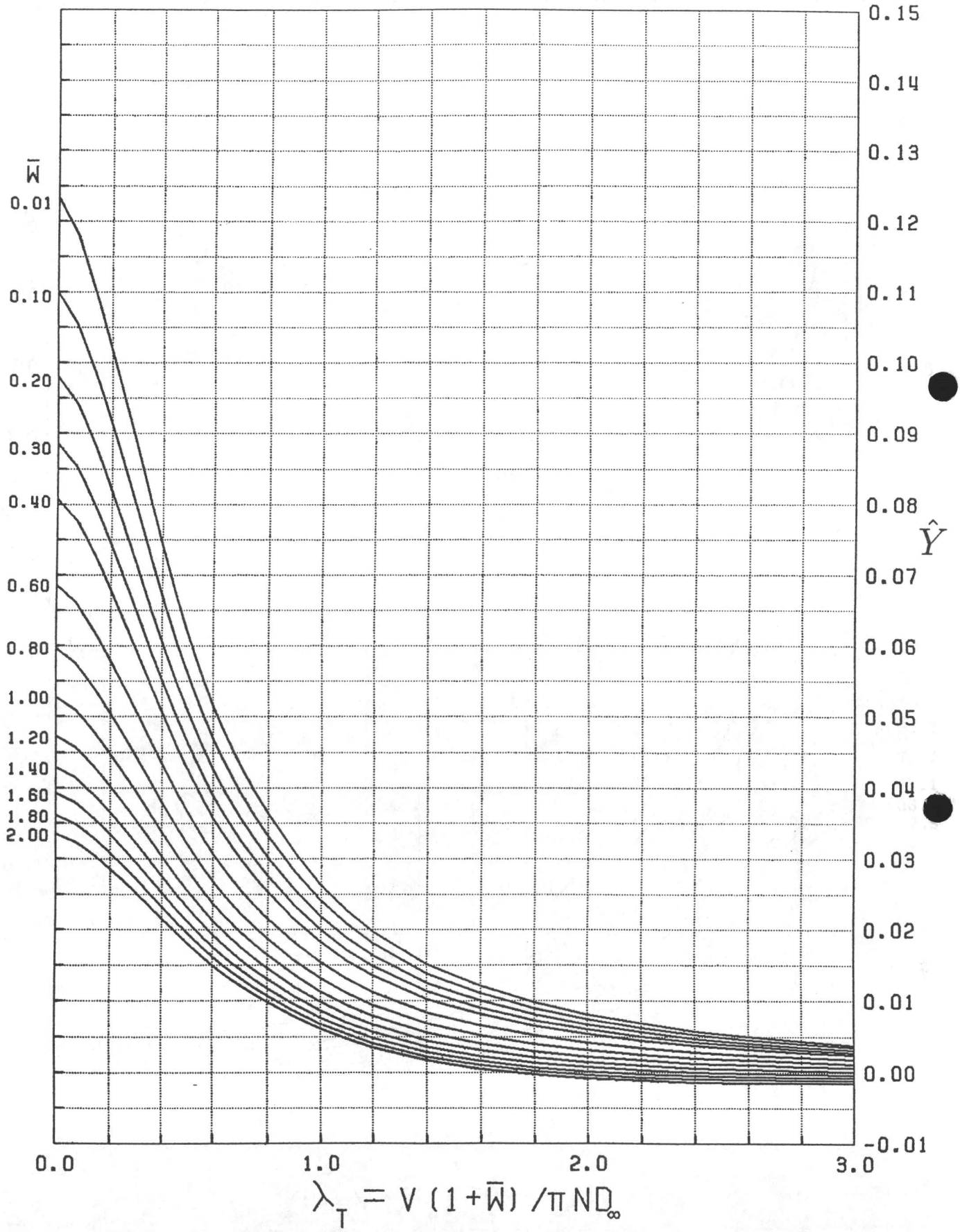

FIG. 53 CONTRACTION COEFFICIENT AT CONSTANT $\bar{w}$
TEN-BLADE PROPELLER

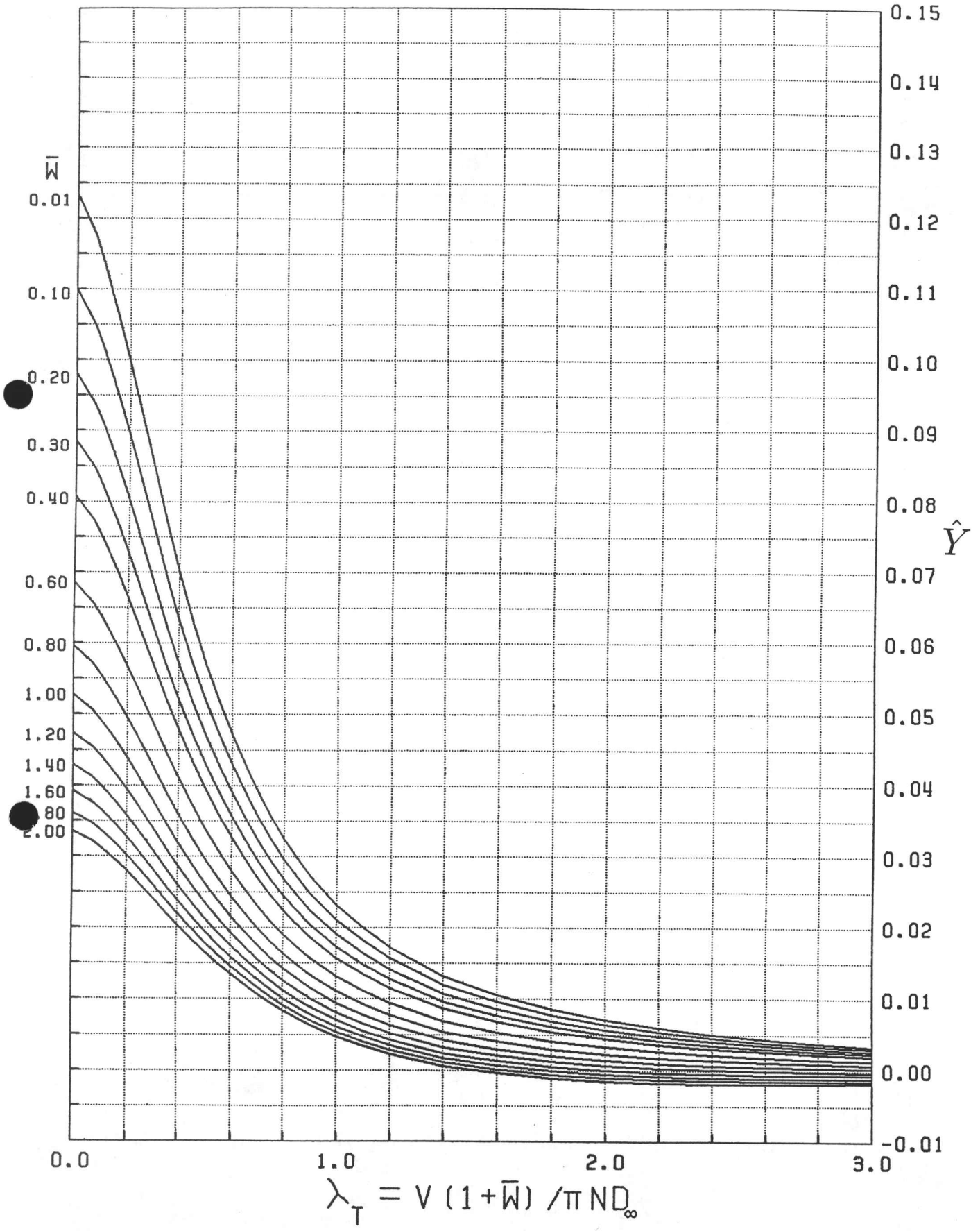

FIG. 52 CONTRACTION COEFFICIENT AT CONSTANT $\bar{w}$
EIGHT-BLADE PROPELLER

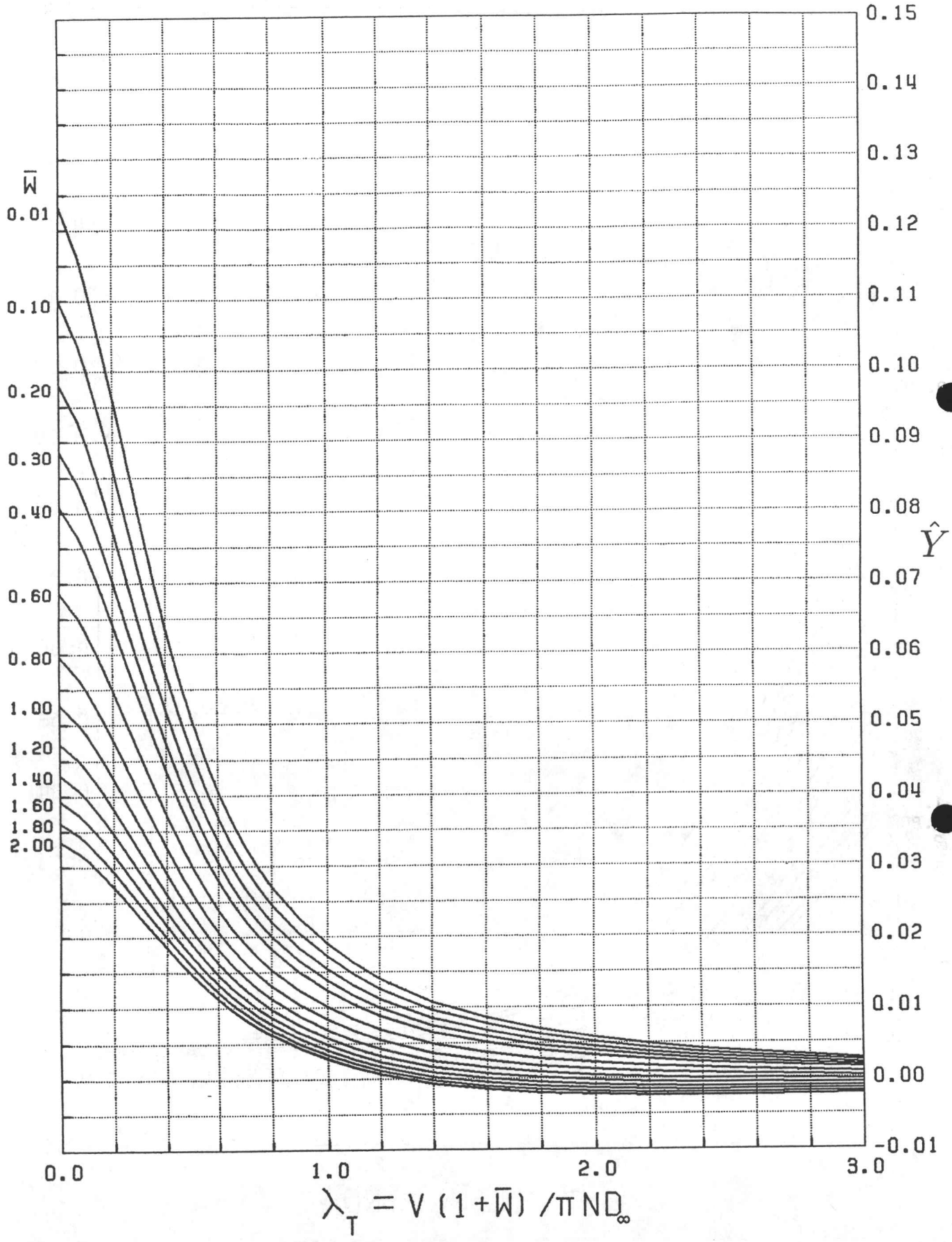

FIG. 51 CONTRACTION COEFFICIENT AT CONSTANT $\bar{w}$
SIX-BLADE PROPELLER

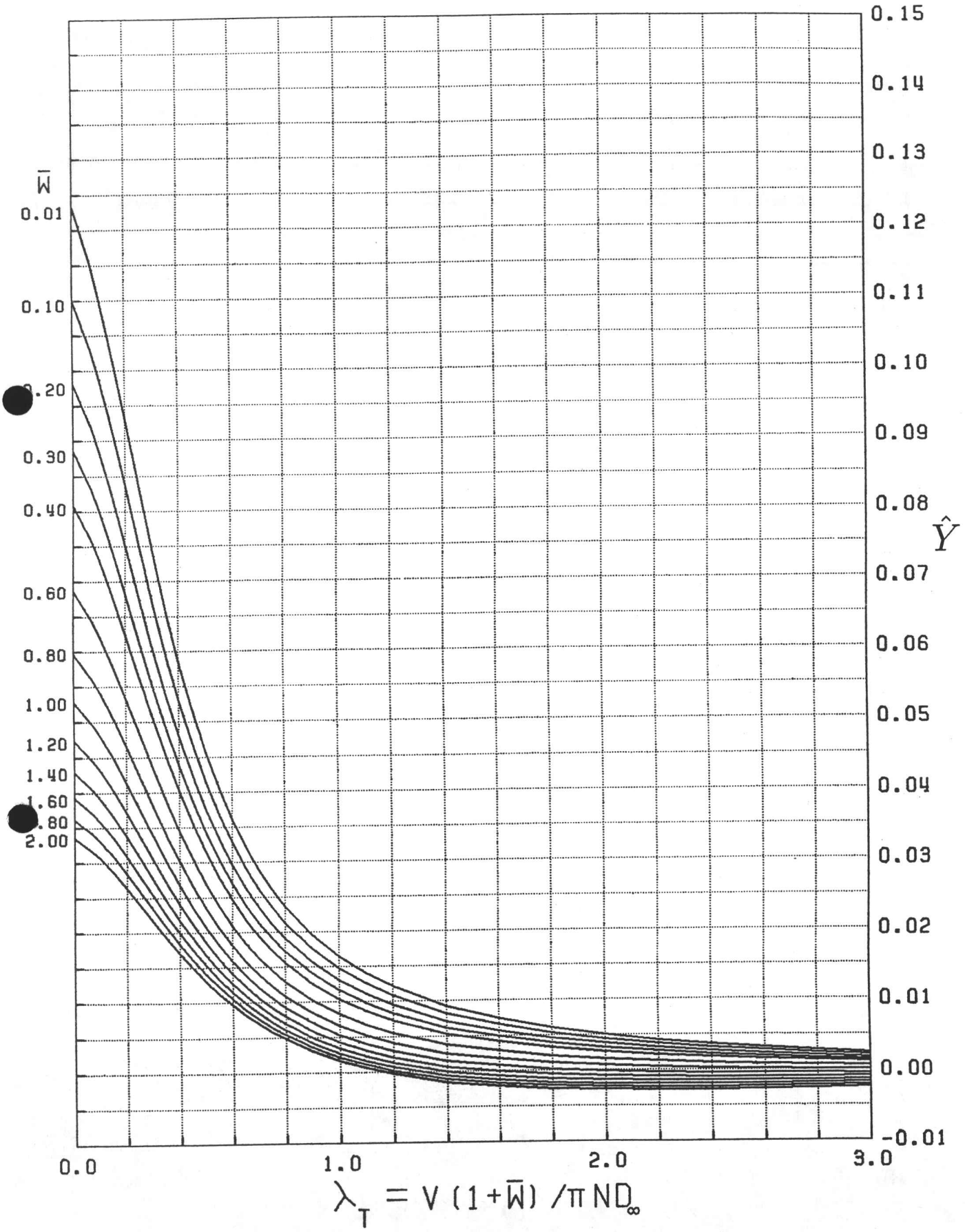

FIG. 50 CONTRACTION COEFFICIENT AT CONSTANT $\bar{w}$
FIVE-BLADE PROPELLER

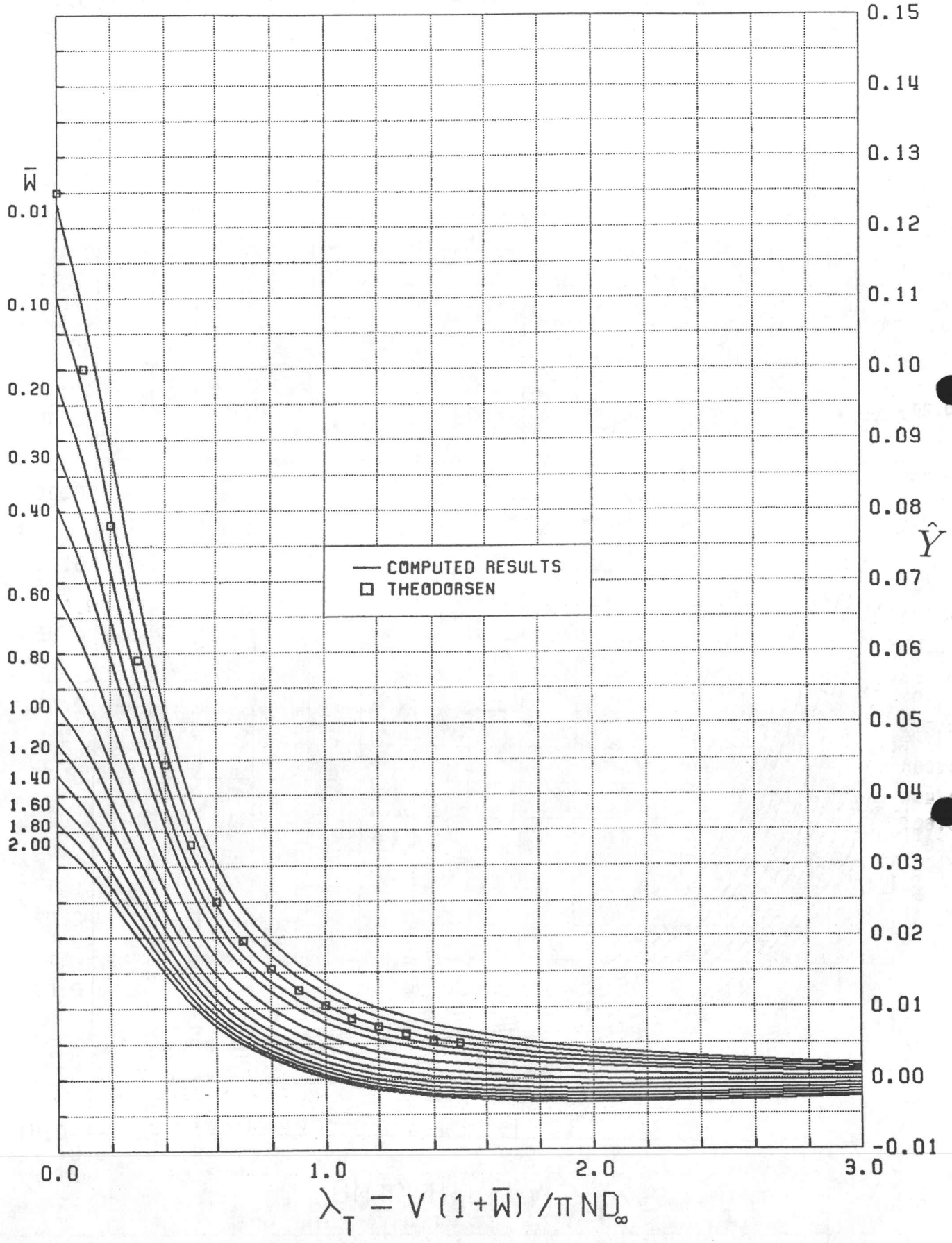

FIG. 49 CONTRACTION COEFFICIENT AT CONSTANT $\bar{w}$
FOUR-BLADE PROPELLER

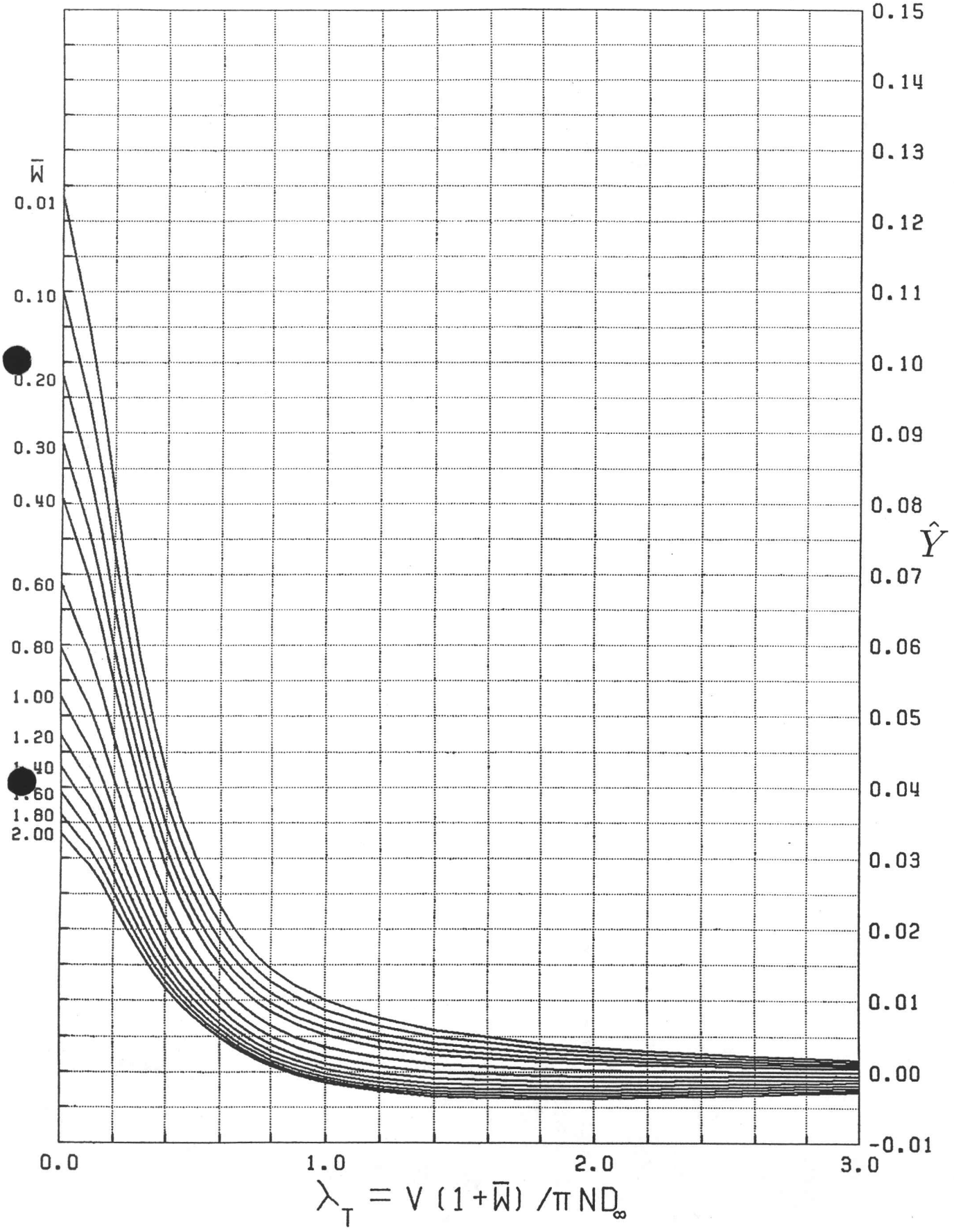

FIG. 48 CONTRACTION COEFFICIENT AT CONSTANT $\bar{w}$
THREE-BLADE PROPELLER

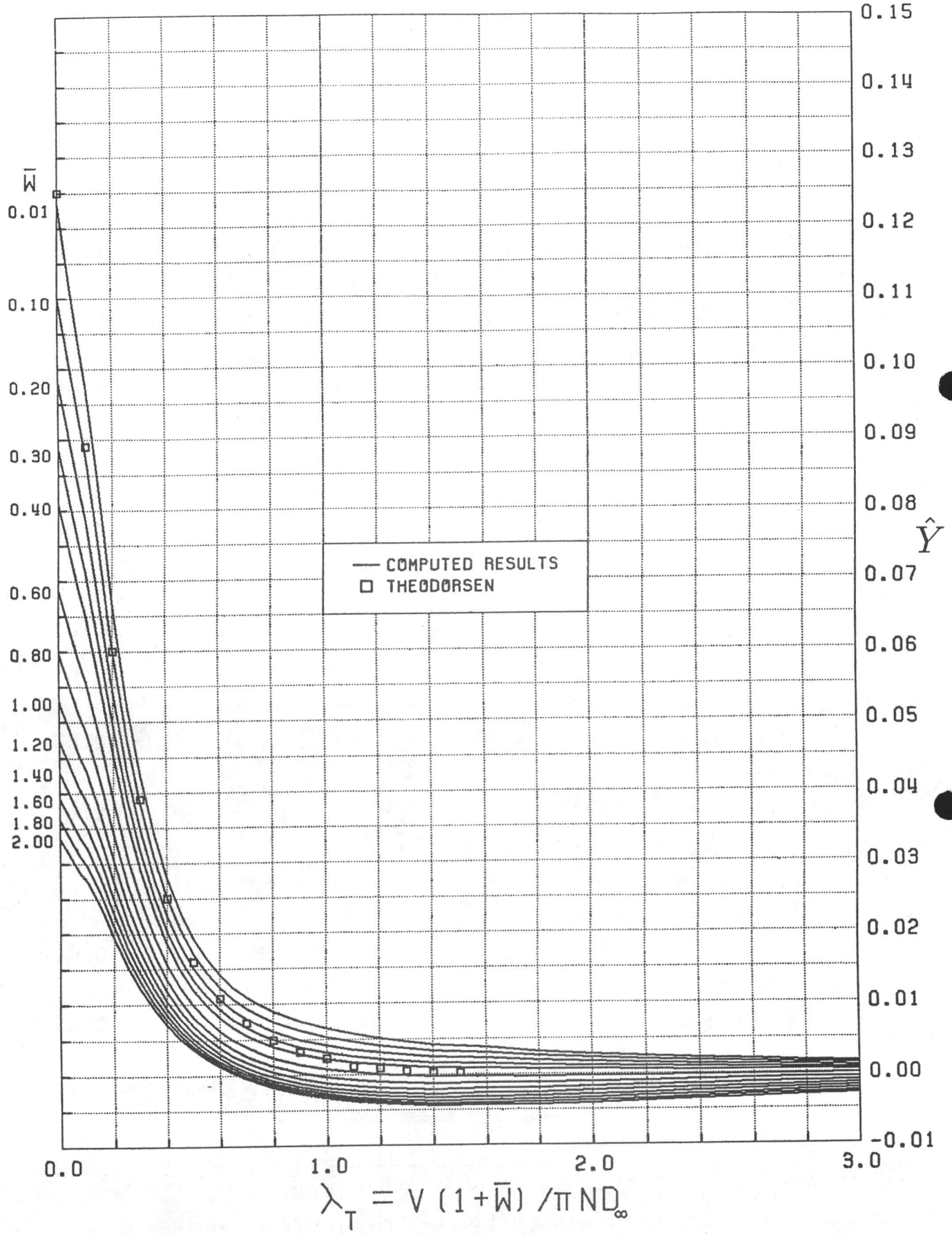

FIG. 47 CONTRACTION COEFFICIENT AT CONSTANT $\bar{w}$
TWO-BLADE PROPELLER

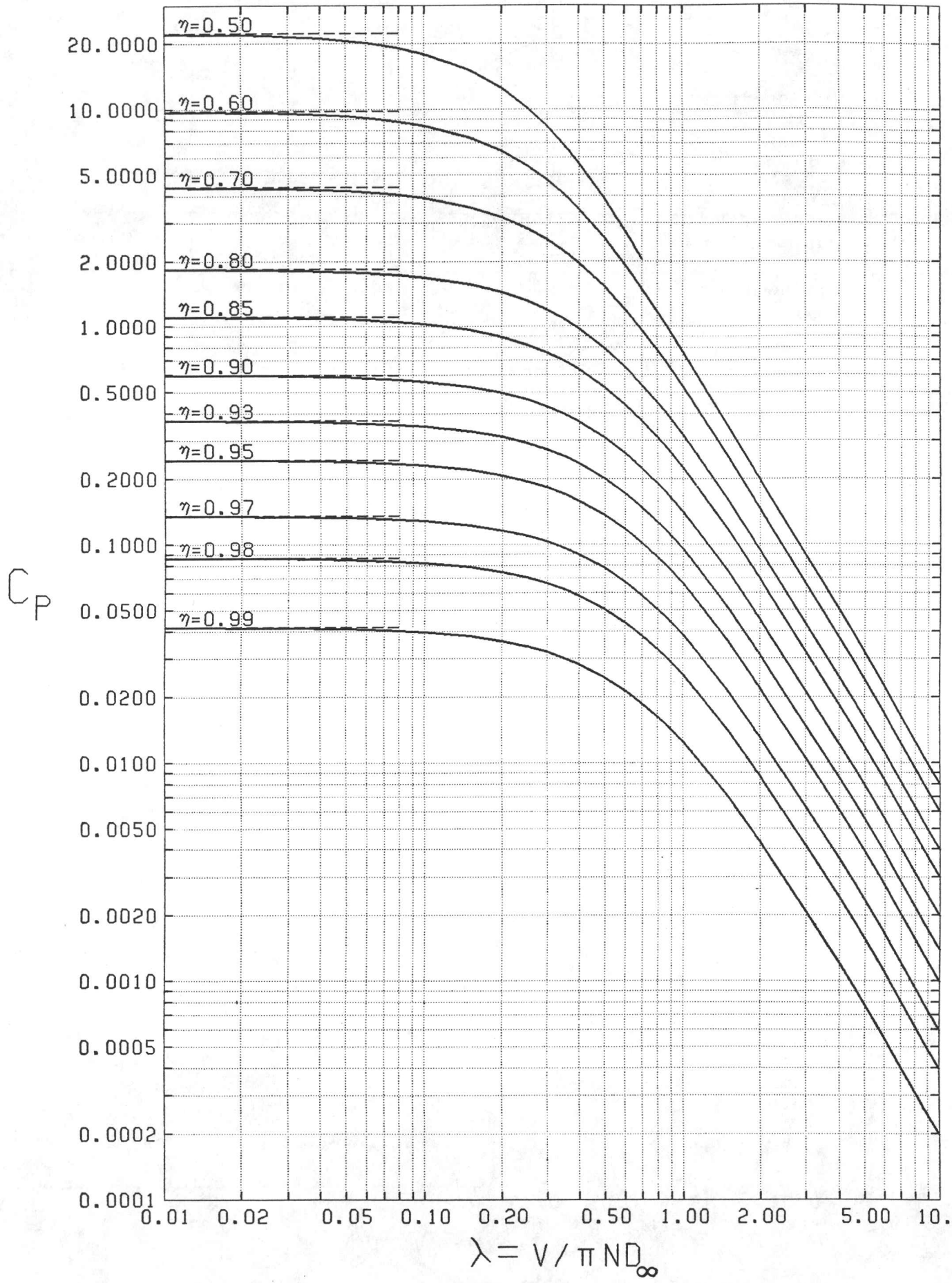

FIG.46 POWER COEFFICIENT AT CONSTANT EFFICIENCY
INFINITE BLADE NUMBER

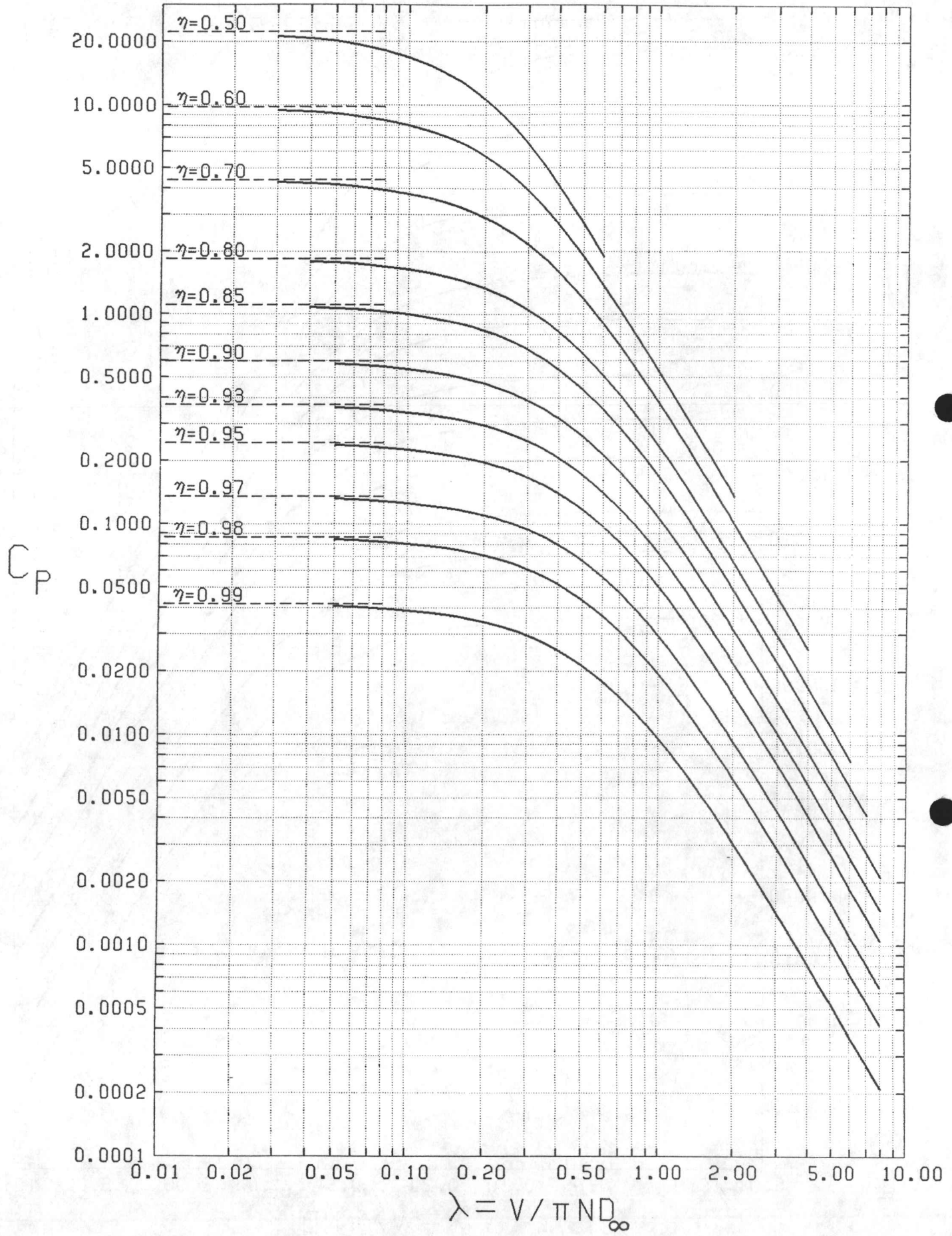

FIG.45 POWER COEFFICIENT AT CONSTANT EFFICIENCY
12 BLADE PROPELLER

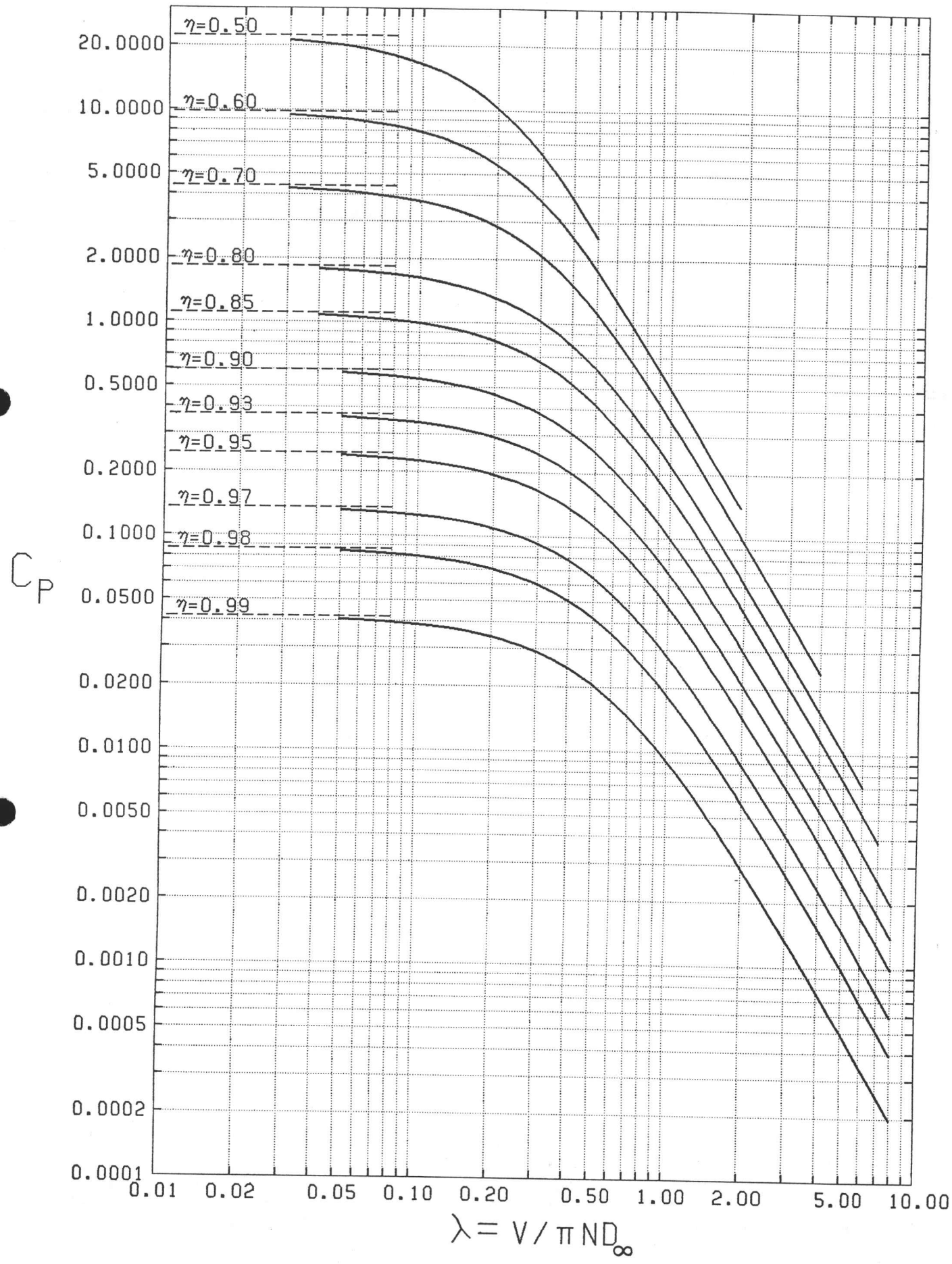

FIG.44 POWER COEFFICIENT AT CONSTANT EFFICIENCY
10 BLADE PROPELLER

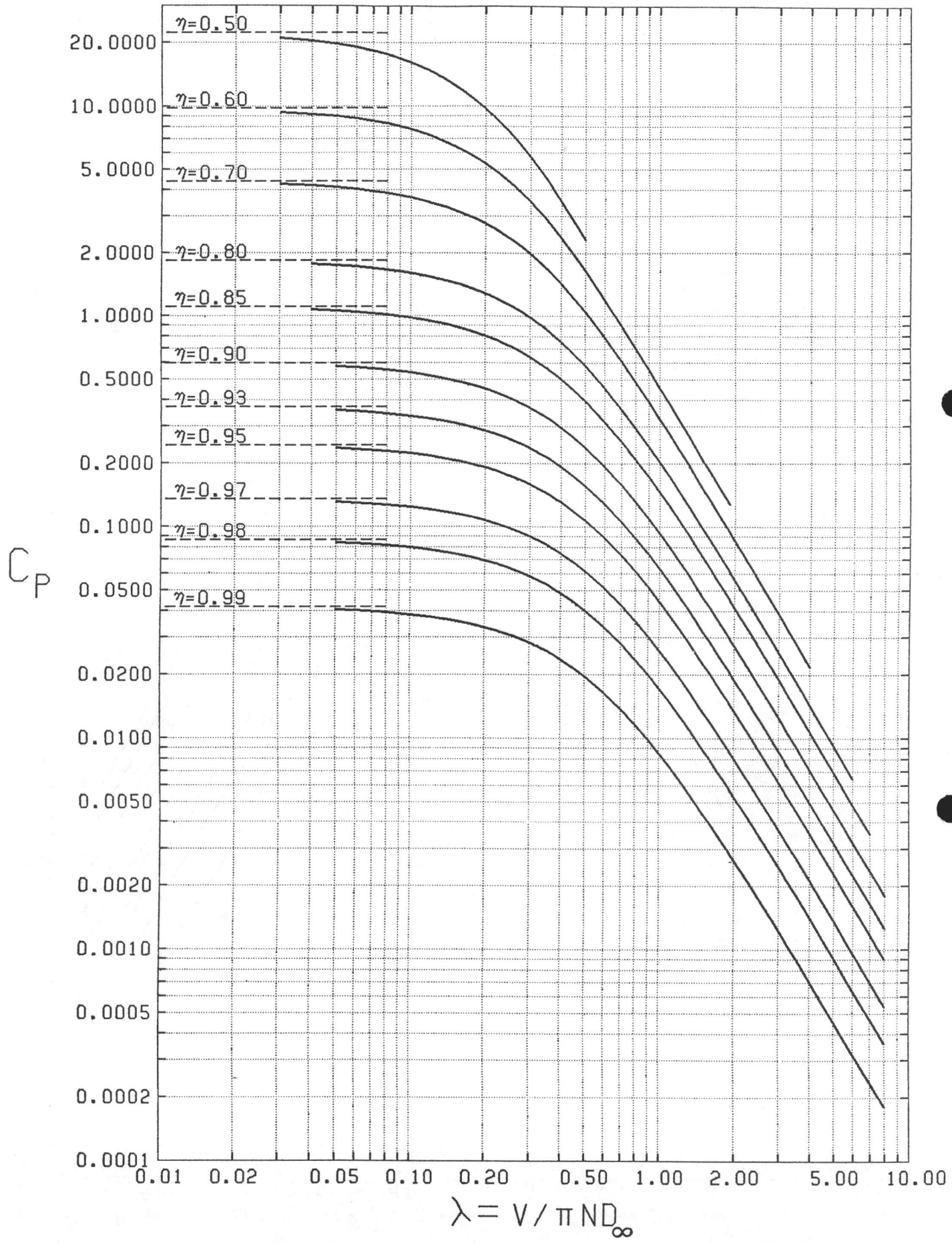

FIG.43 POWER COEFFICIENT AT CONSTANT EFFICIENCY
8 BLADE PROPELLER

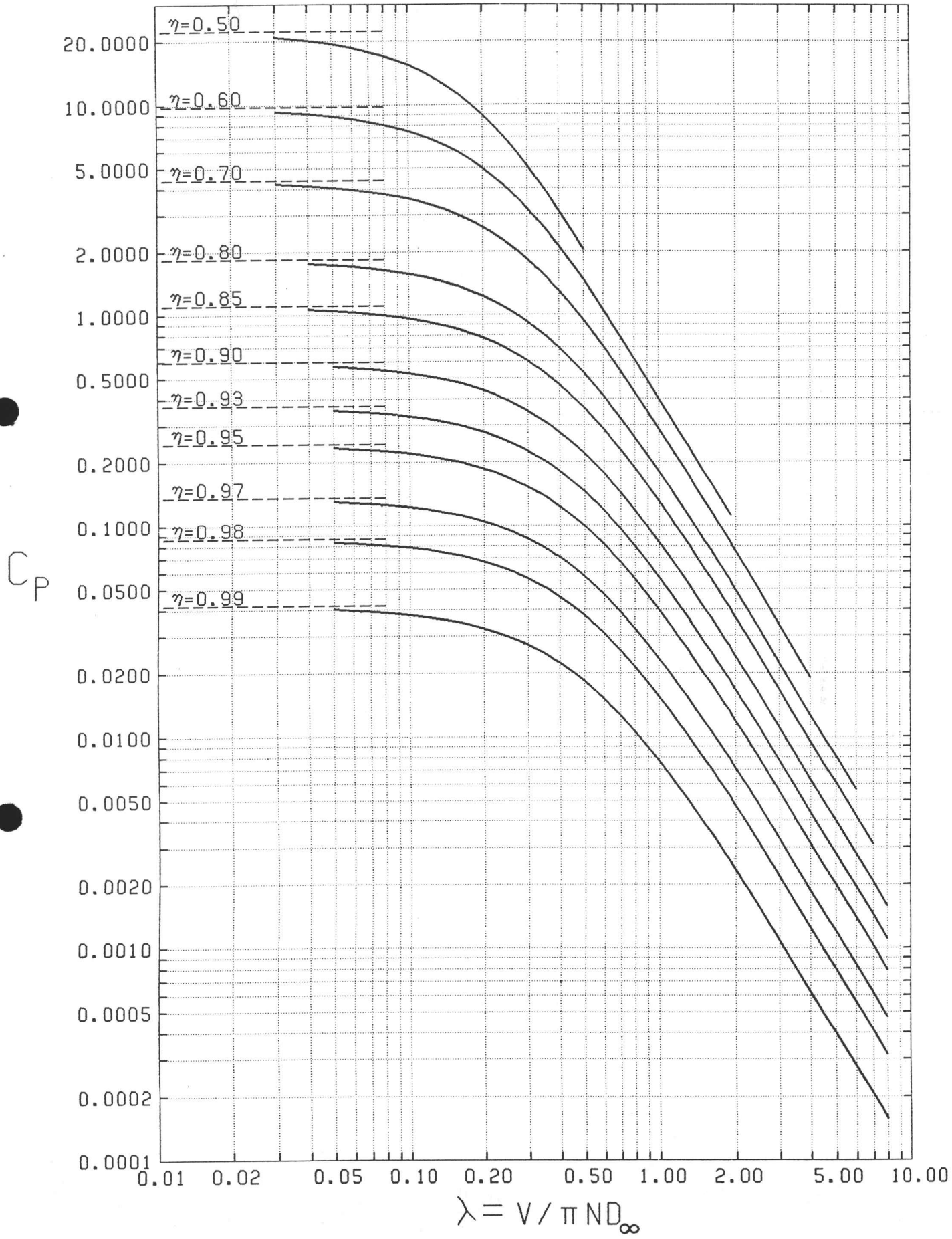

FIG.42 POWER COEFFICIENT AT CONSTANT EFFICIENCY
6 BLADE PROPELLER

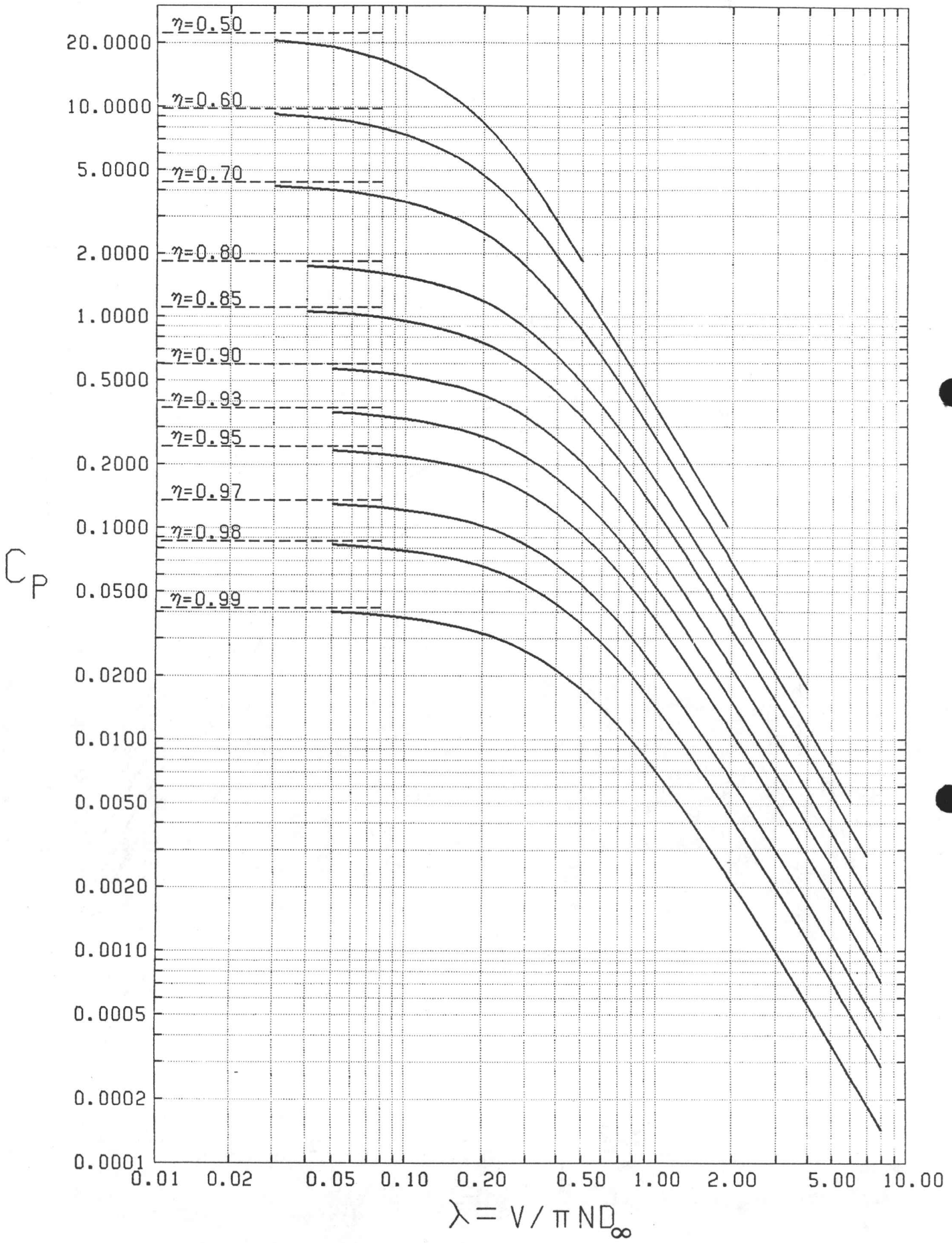

FIG.41 PØWER CØEFFICIENT AT CØNSTANT EFFICIENCY
5 BLADE PRØPELLER

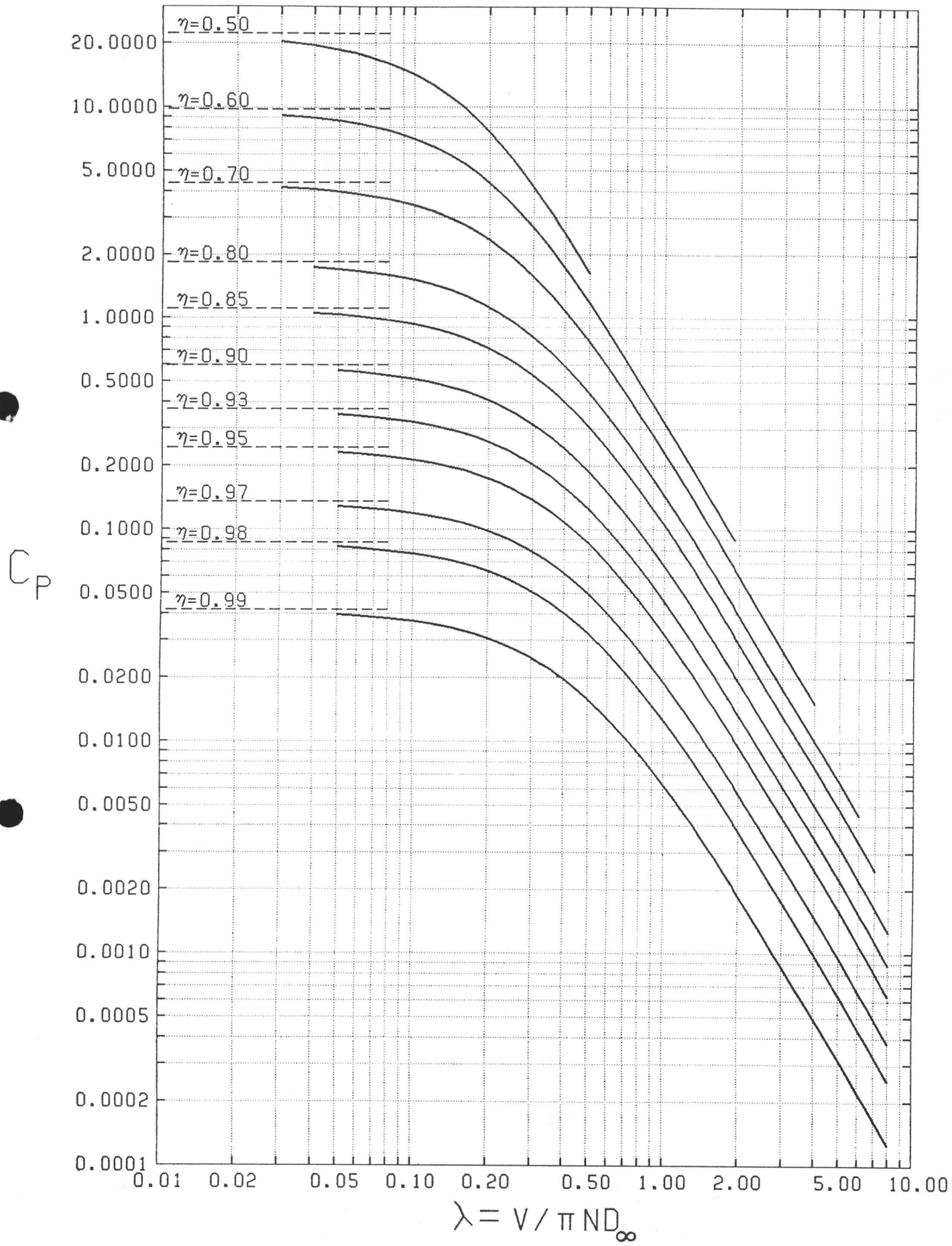

FIG.40 POWER COEFFICIENT AT CONSTANT EFFICIENCY
4 BLADE PROPELLER

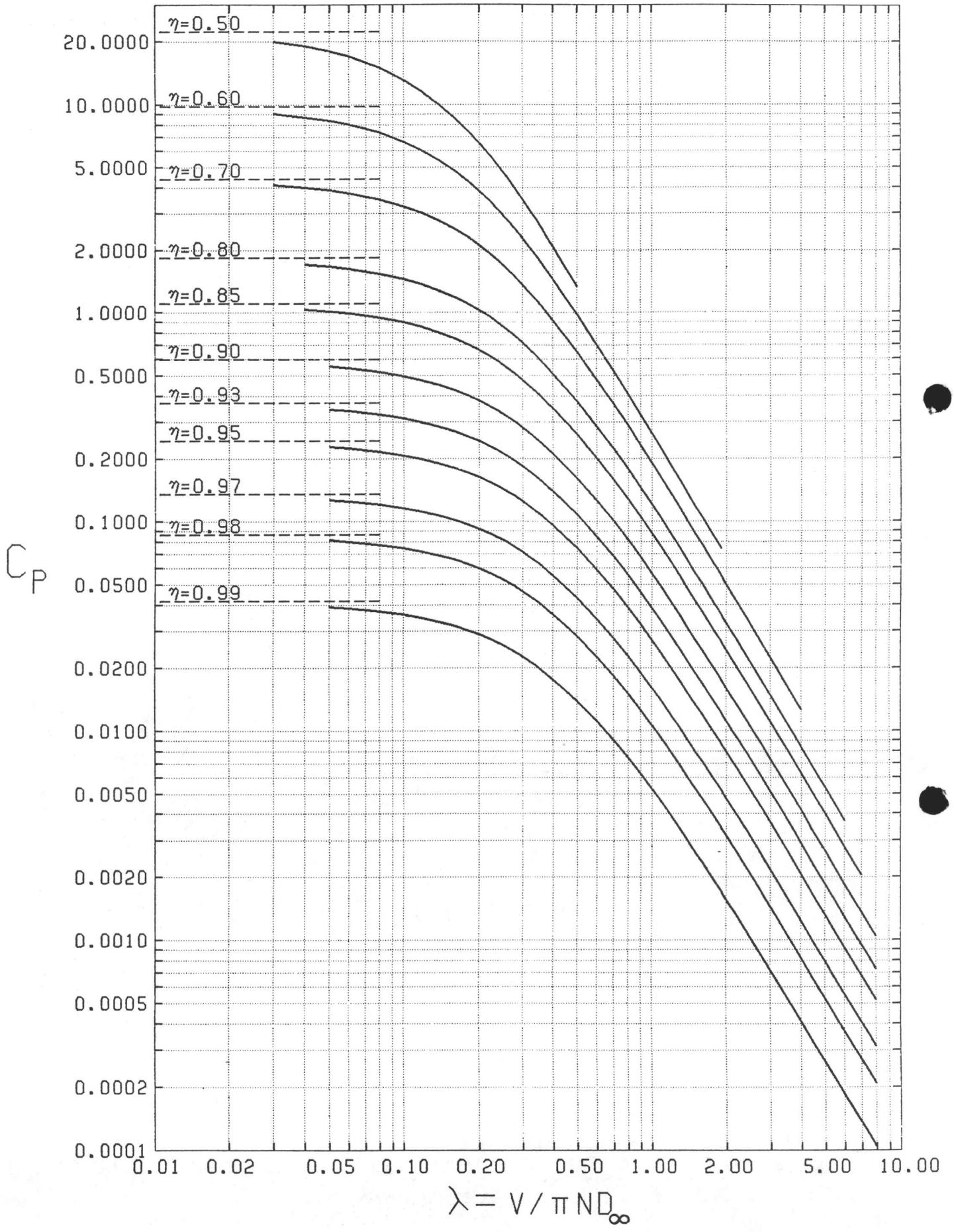

FIG.39 POWER COEFFICIENT AT CONSTANT EFFICIENCY
3 BLADE PROPELLER

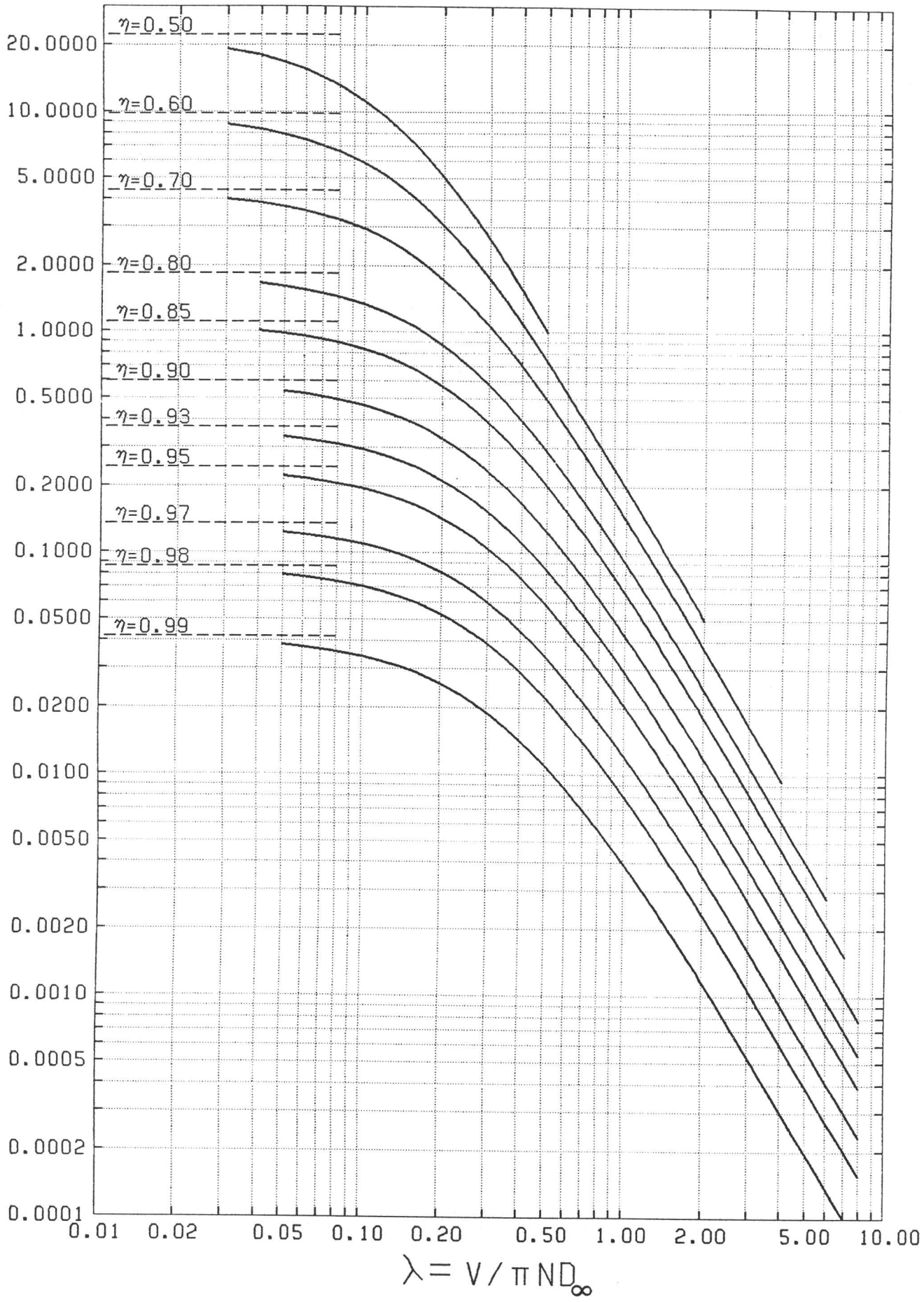

FIG.38 POWER COEFFICIENT AT CONSTANT EFFICIENCY
2 BLADE PROPELLER

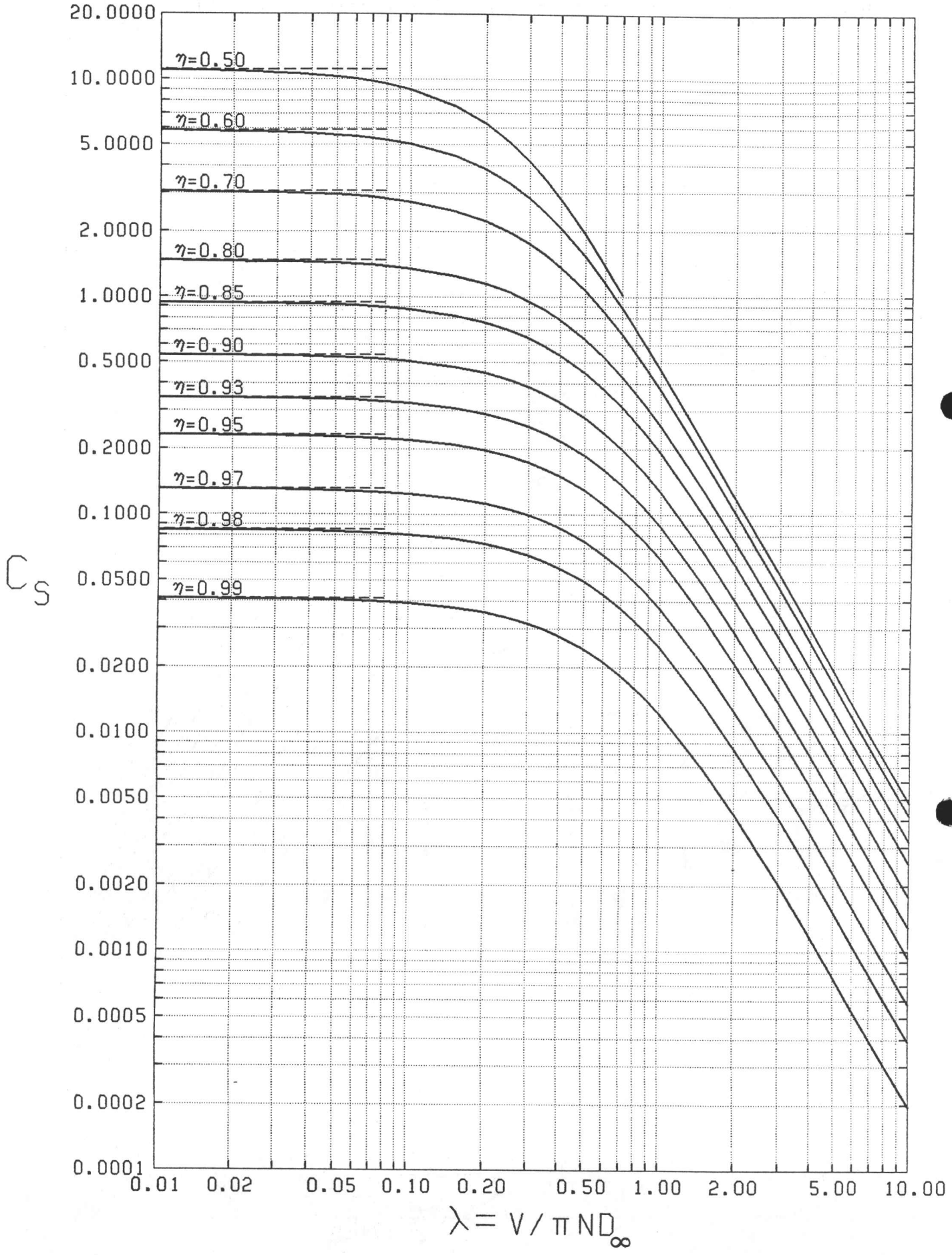

FIG.37 THRUST COEFFICIENT AT CONSTANT EFFICIENCY
INFINITE BLADE NUMBER

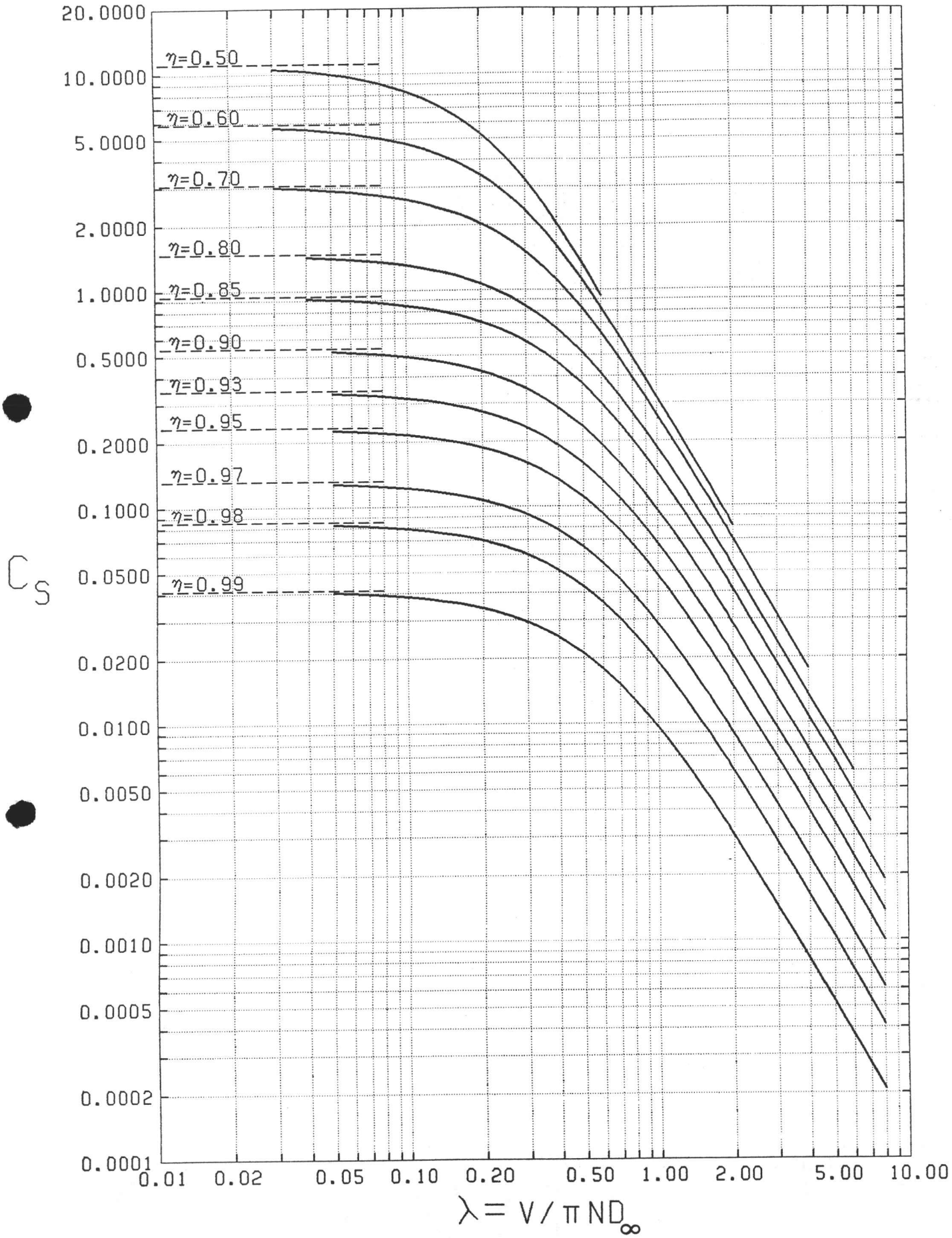

FIG.36 THRUST COEFFICIENT AT CONSTANT EFFICIENCY
12 BLADE PROPELLER

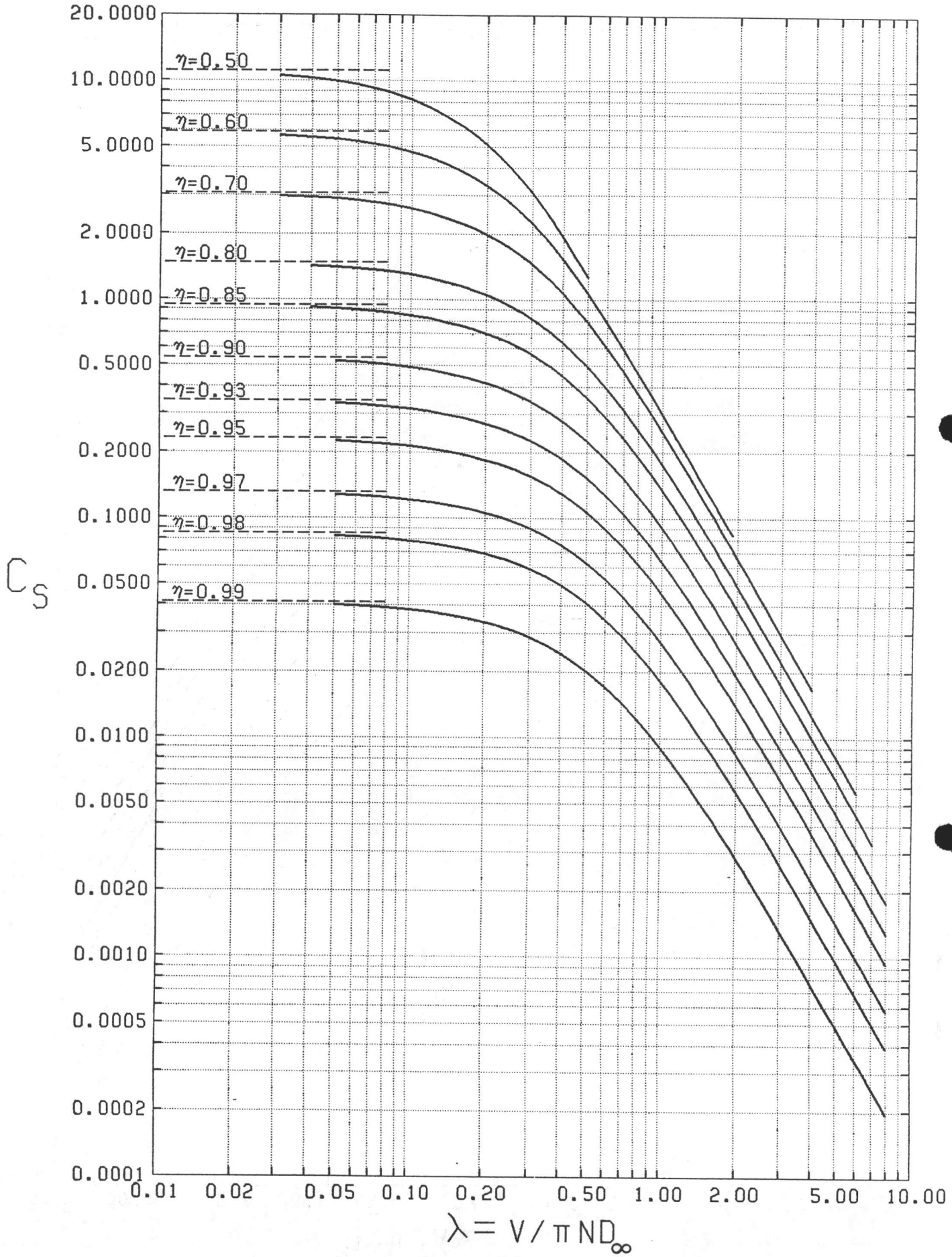

FIG.35 THRUST COEFFICIENT AT CONSTANT EFFICIENCY
10 BLADE PROPELLER

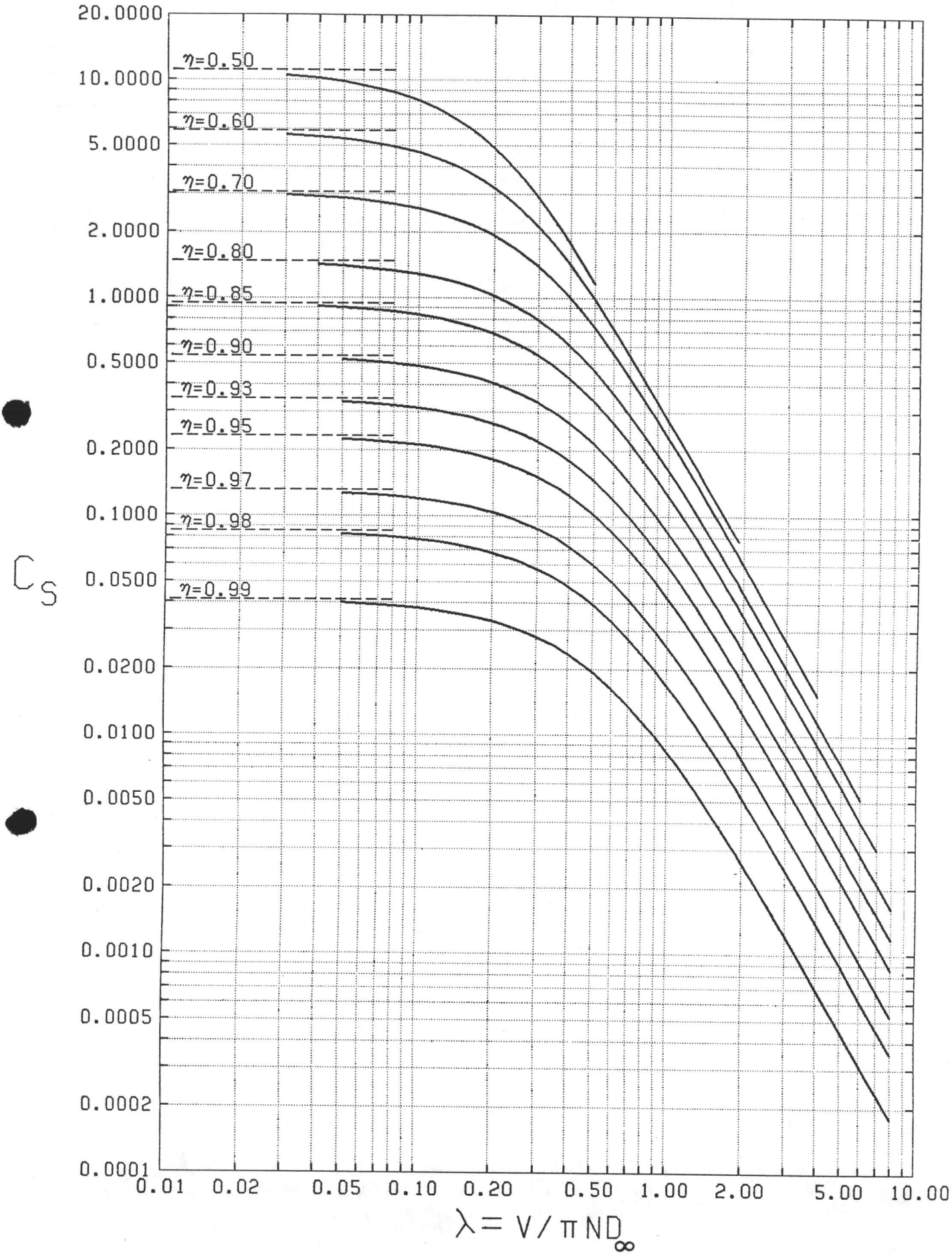

FIG.34 THRUST COEFFICIENT AT CONSTANT EFFICIENCY
8 BLADE PROPELLER

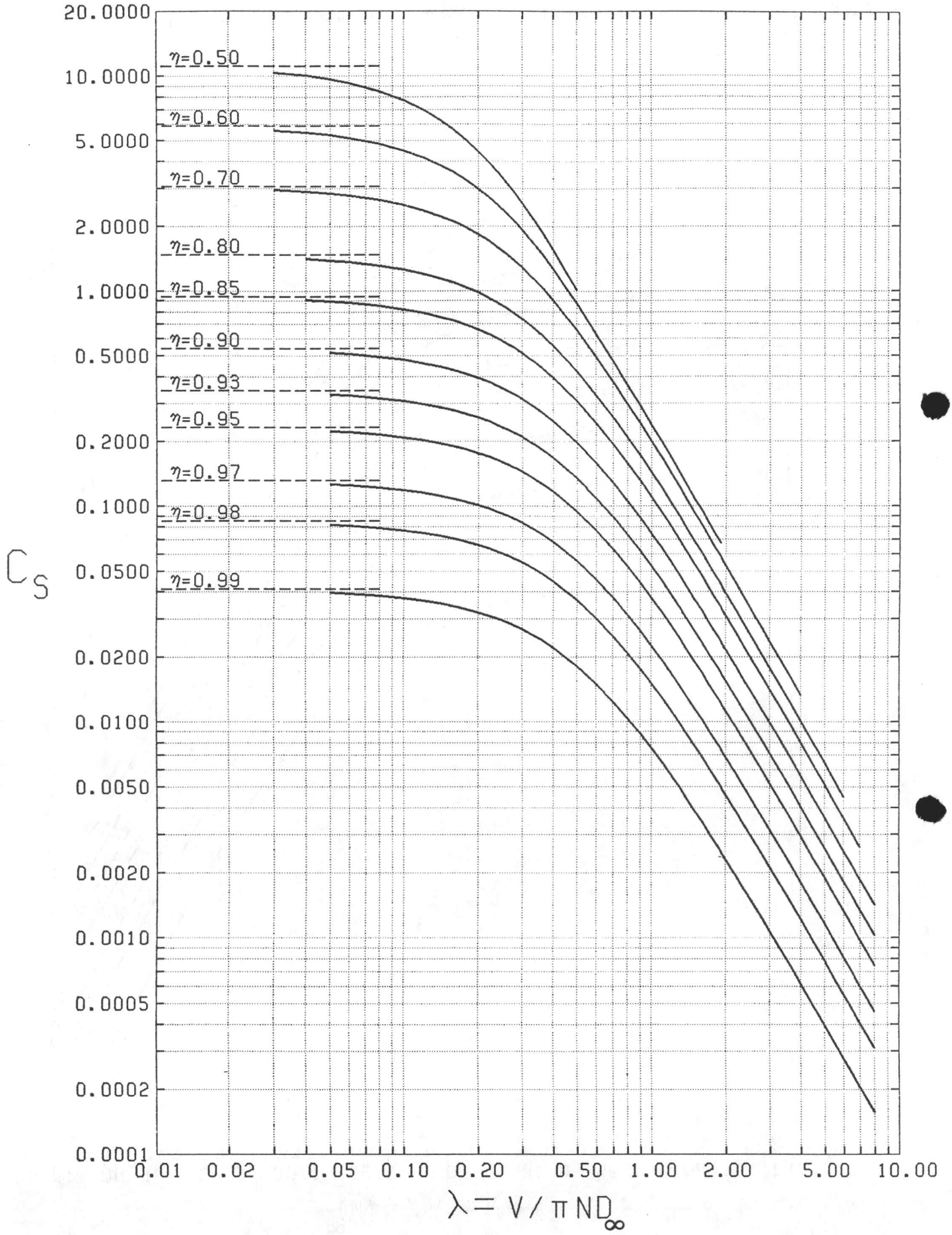

FIG.33 THRUST COEFFICIENT AT CONSTANT EFFICIENCY
6 BLADE PROPELLER

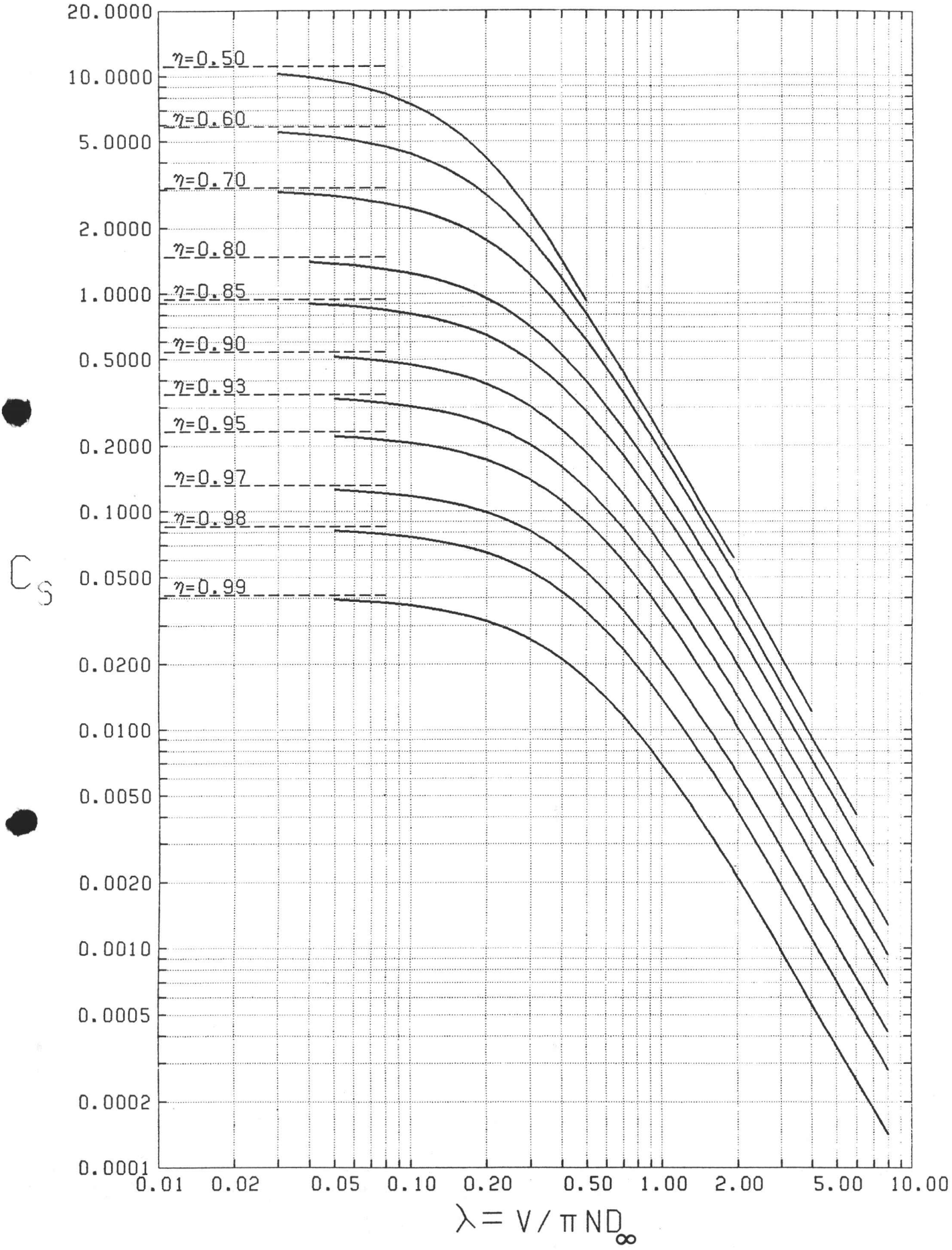

FIG.32 THRUST COEFFICIENT AT CONSTANT EFFICIENCY
5 BLADE PROPELLER

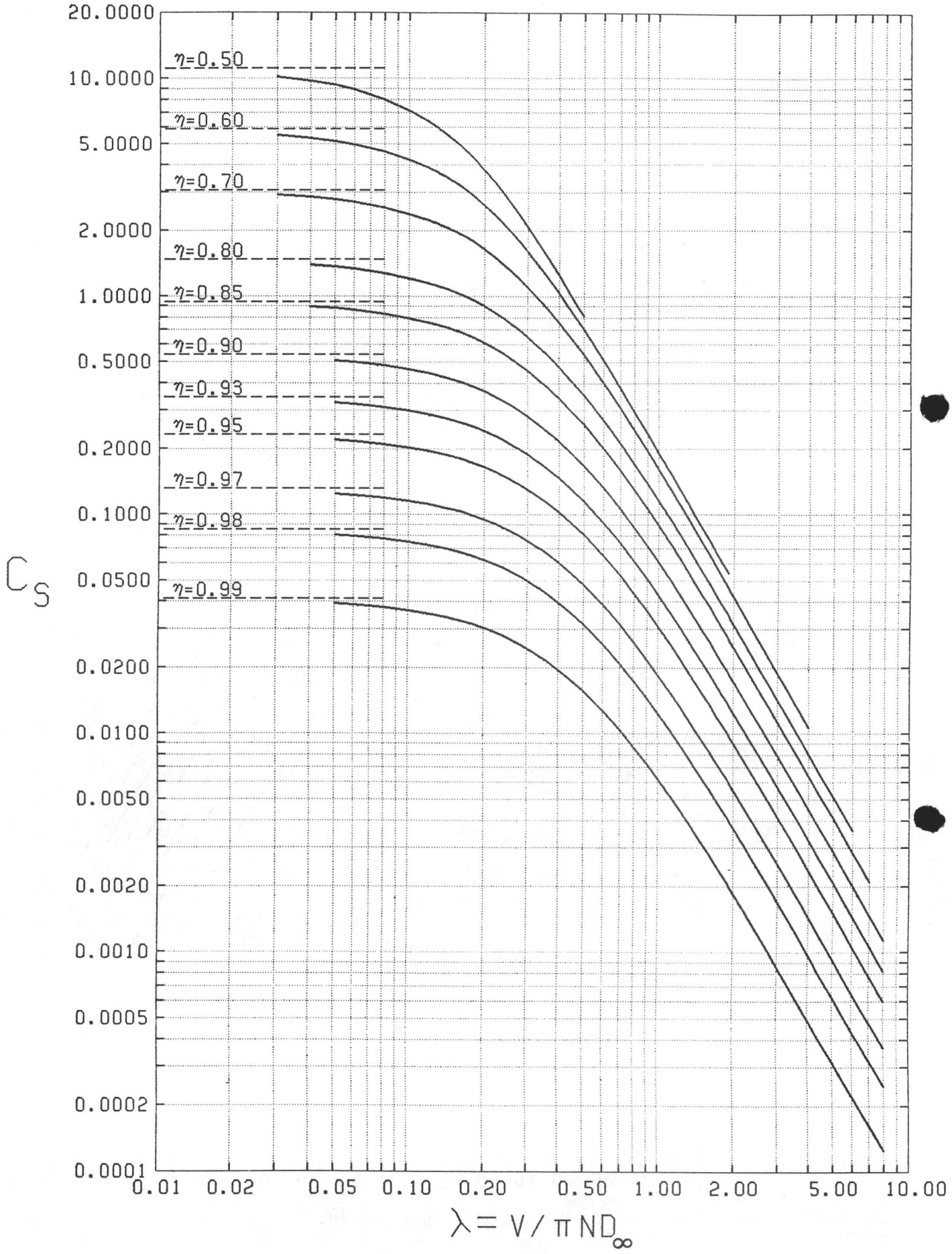

FIG.31 THRUST COEFFICIENT AT CONSTANT EFFICIENCY
4 BLADE PROPELLER

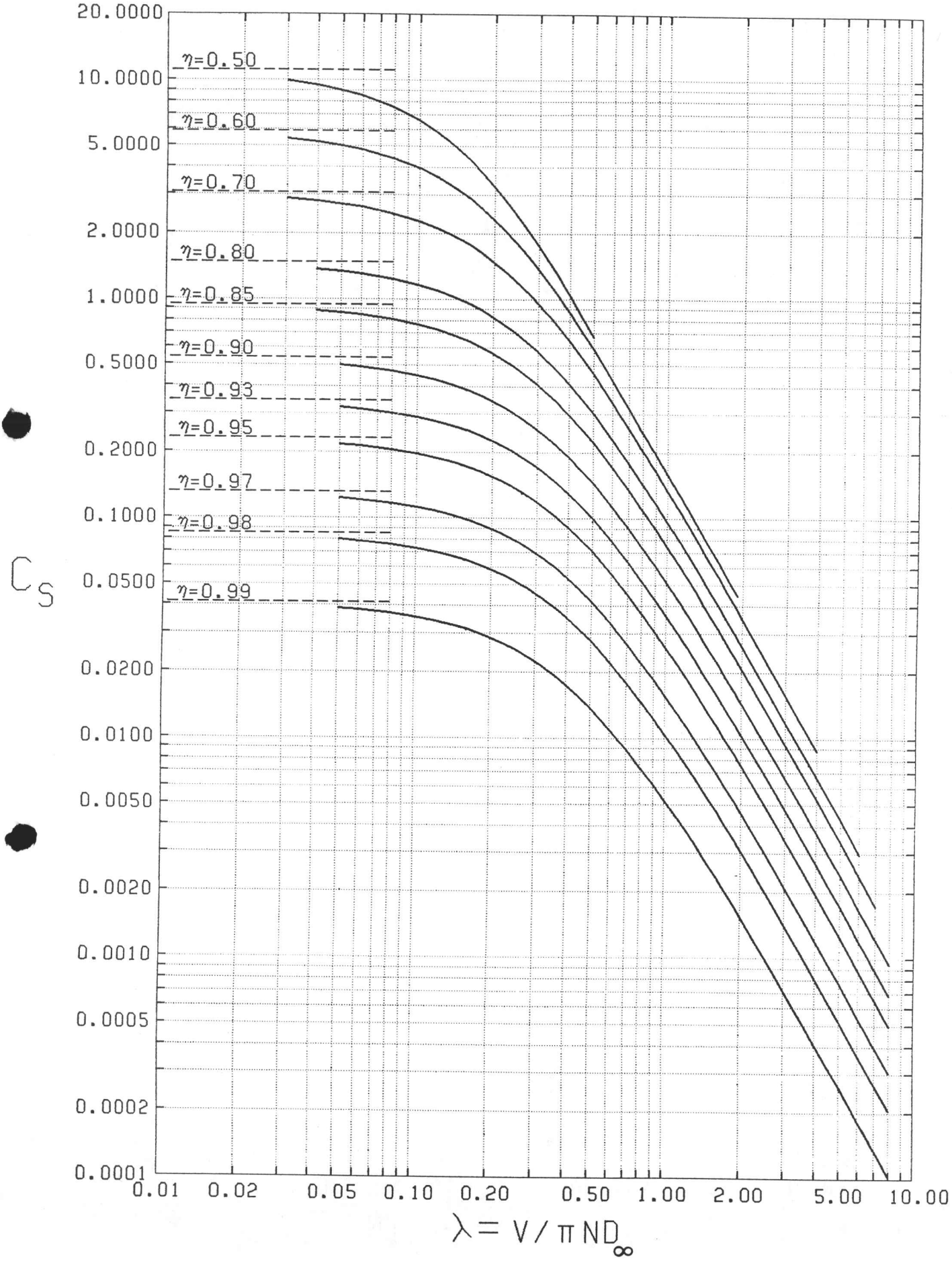

FIG.30 THRUST COEFFICIENT AT CONSTANT EFFICIENCY
3 BLADE PROPELLER

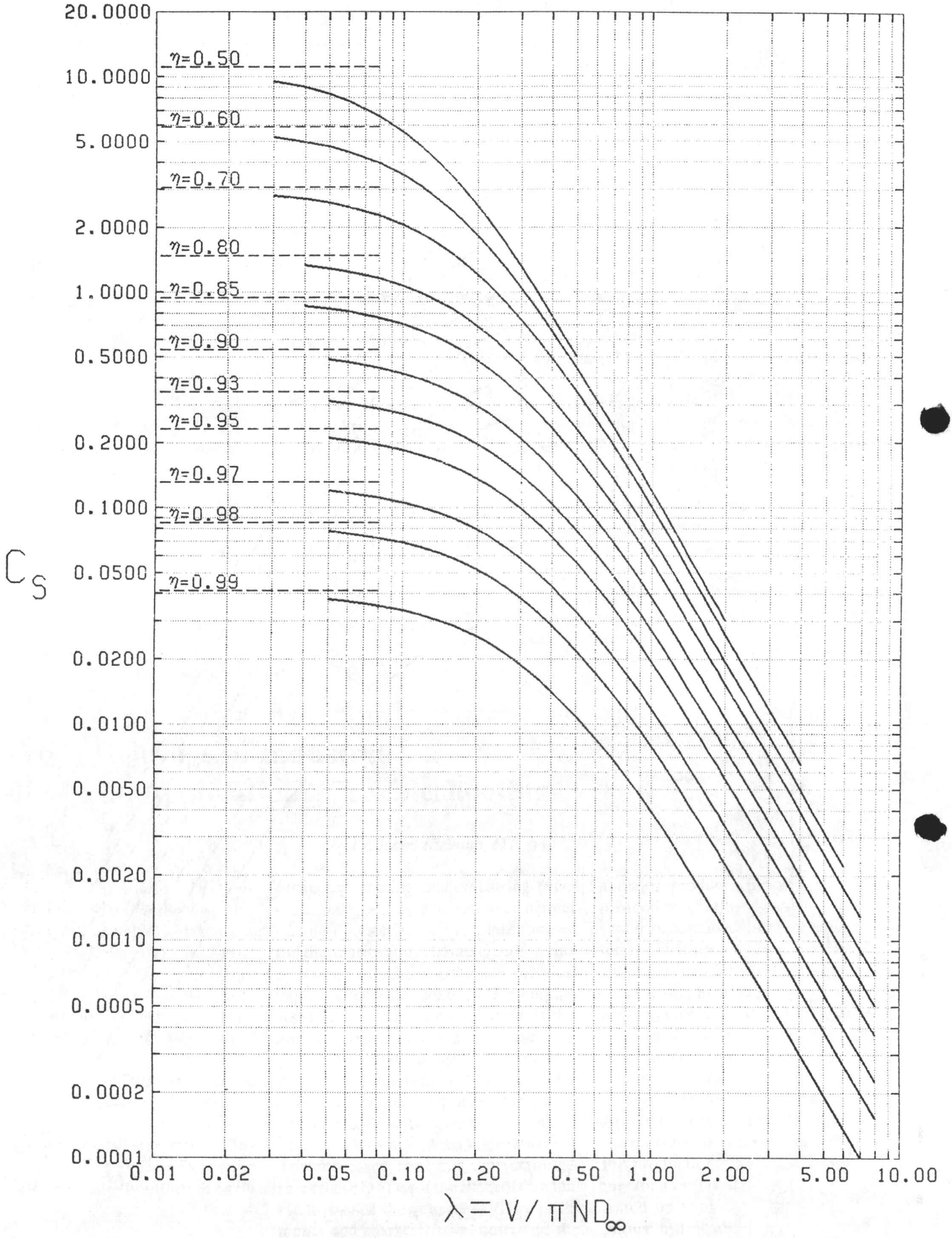

FIG. 29 THRUST COEFFICIENT AT CONSTANT EFFICIENCY
2 BLADE PROPELLER

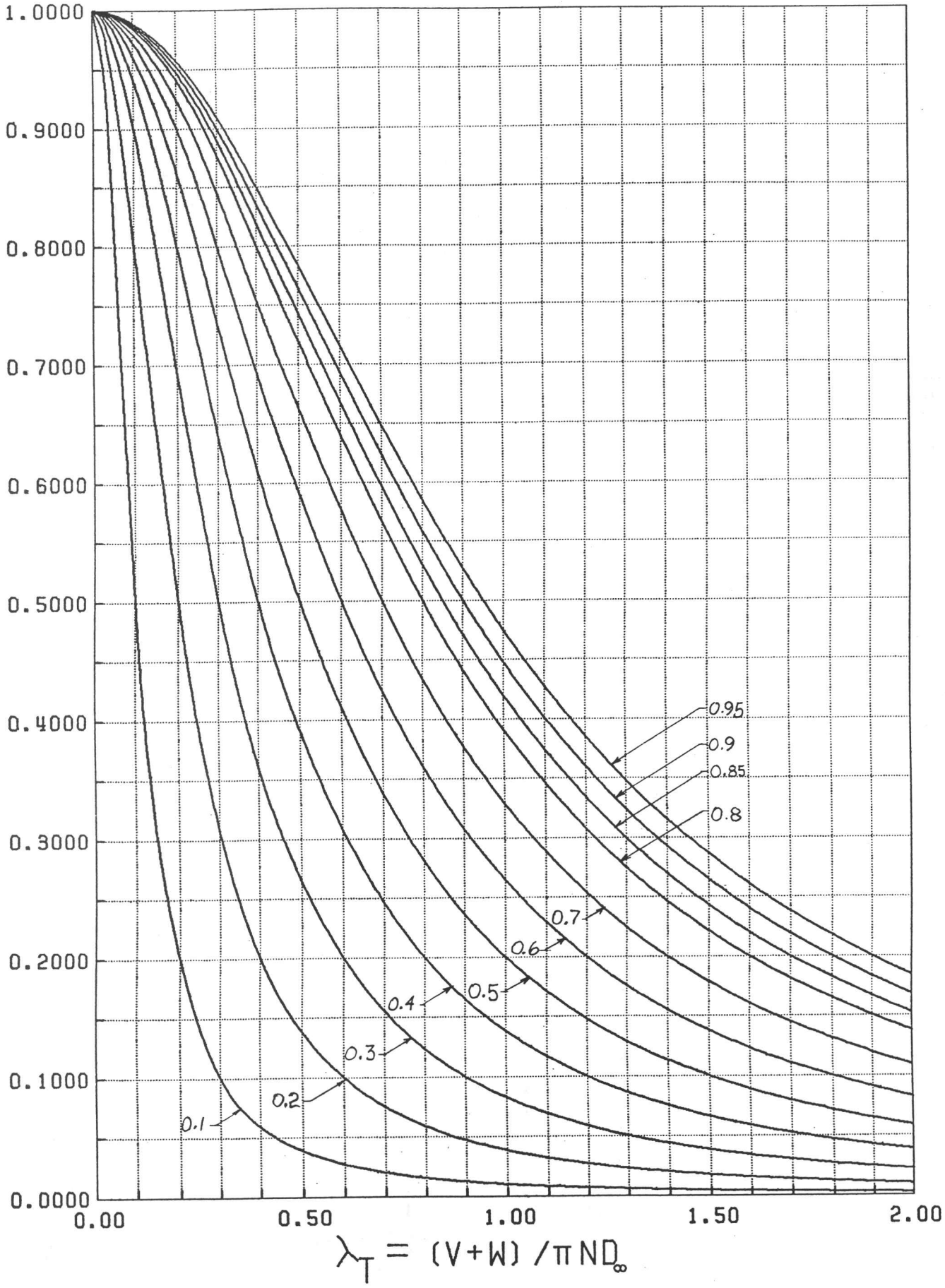

FIG. 28 OPTIMUM CIRCULATION AT CONSTANT RADIUS INFINITE BLADE NUMBER

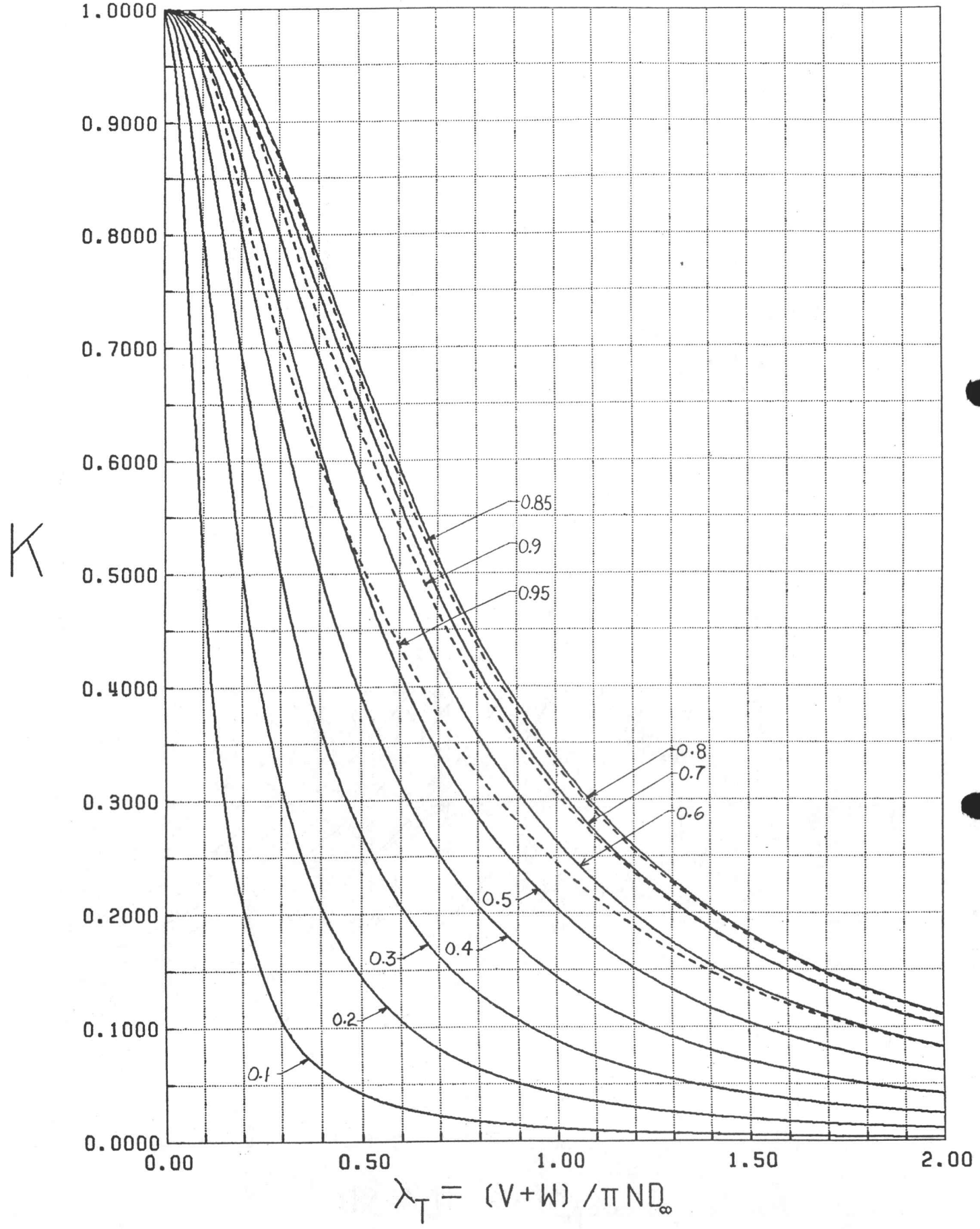

FIG. 27 OPTIMUM CIRCULATION AT CONSTANT RADIUS
12 BLADE PROPELLER

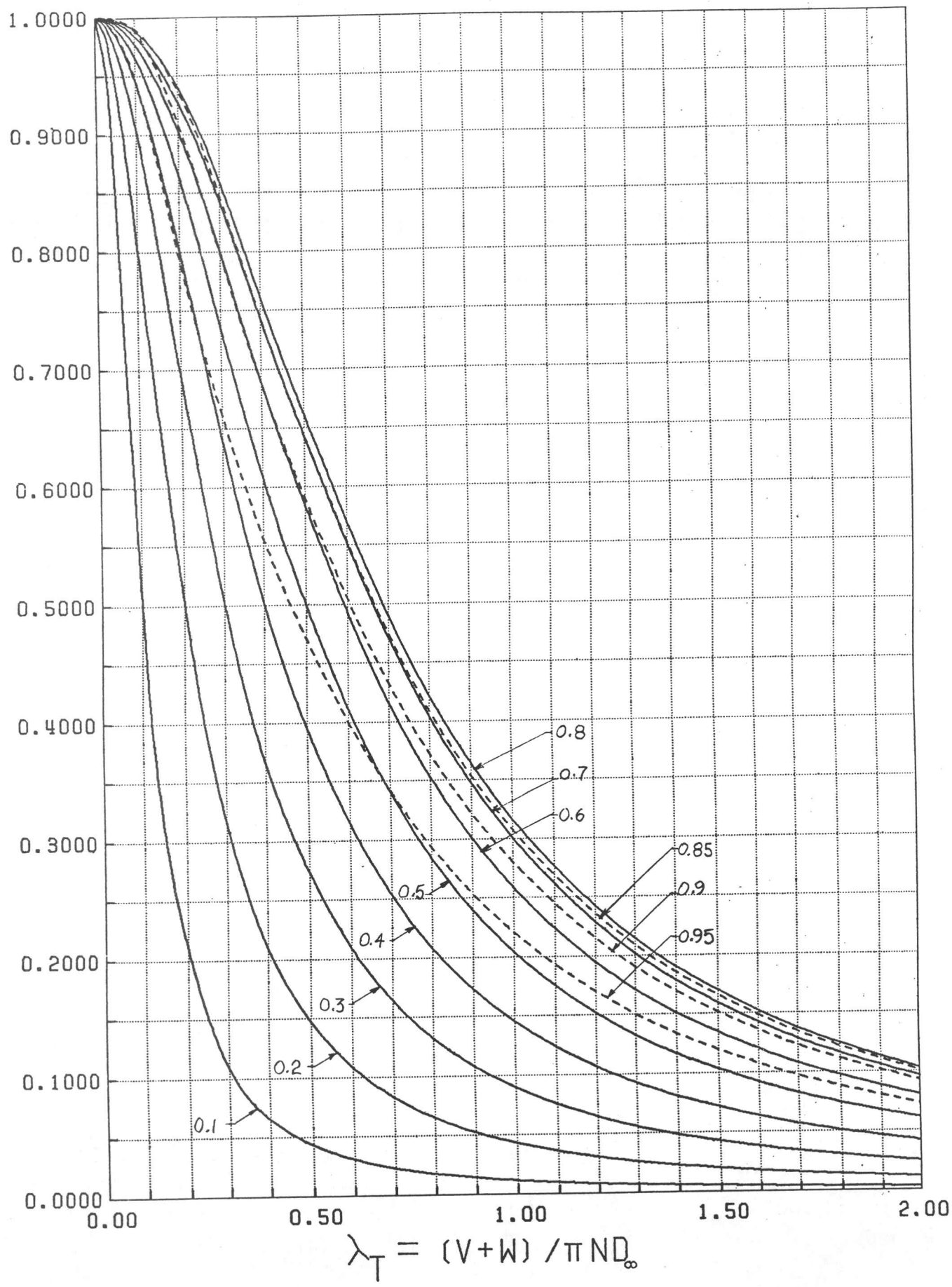

FIG. 26 OPTIMUM CIRCULATION AT CONSTANT RADIUS
10 BLADE PROPELLER

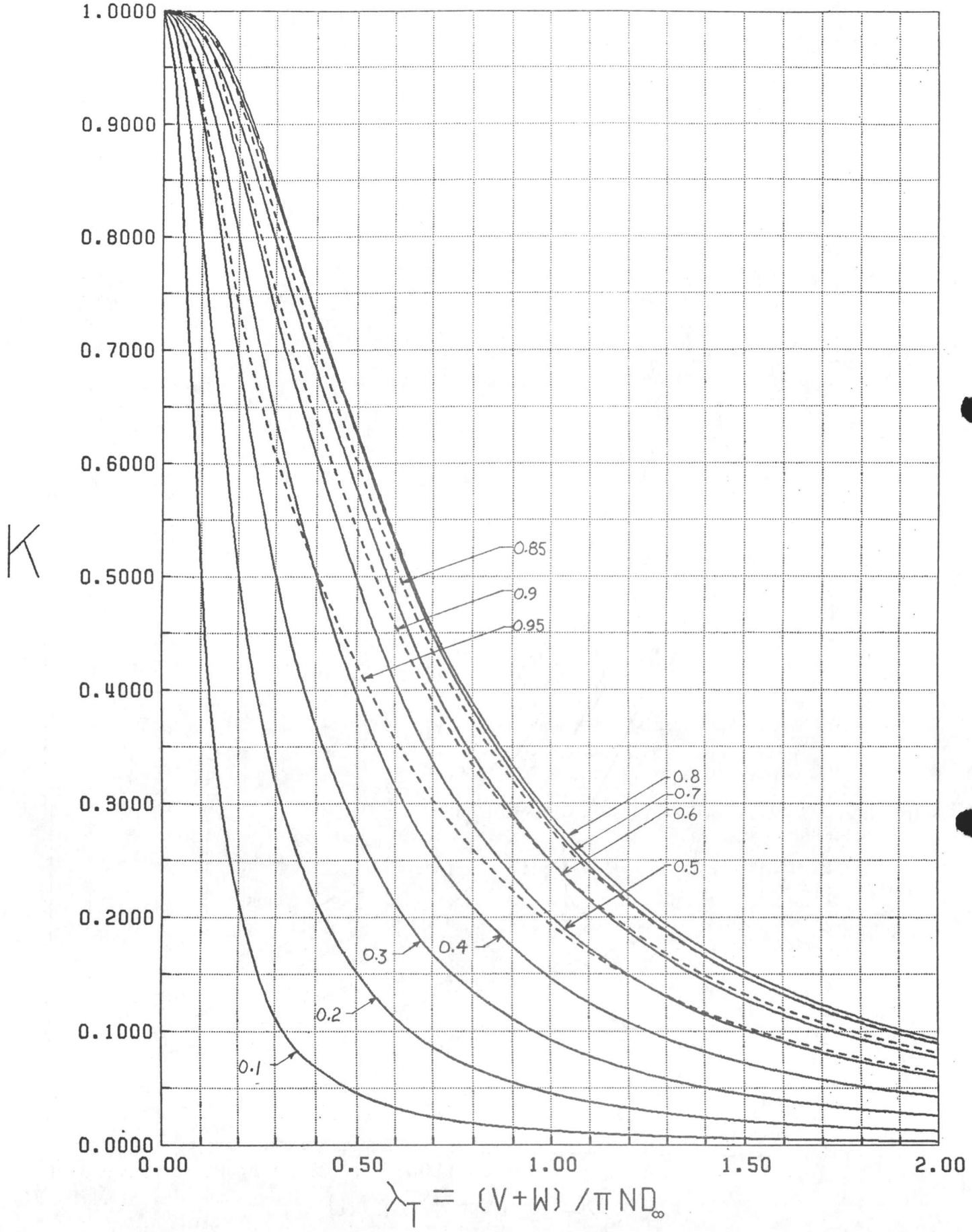

FIG. 25 OPTIMUM CIRCULATION AT CONSTANT RADIUS
8 BLADE PROPELLER

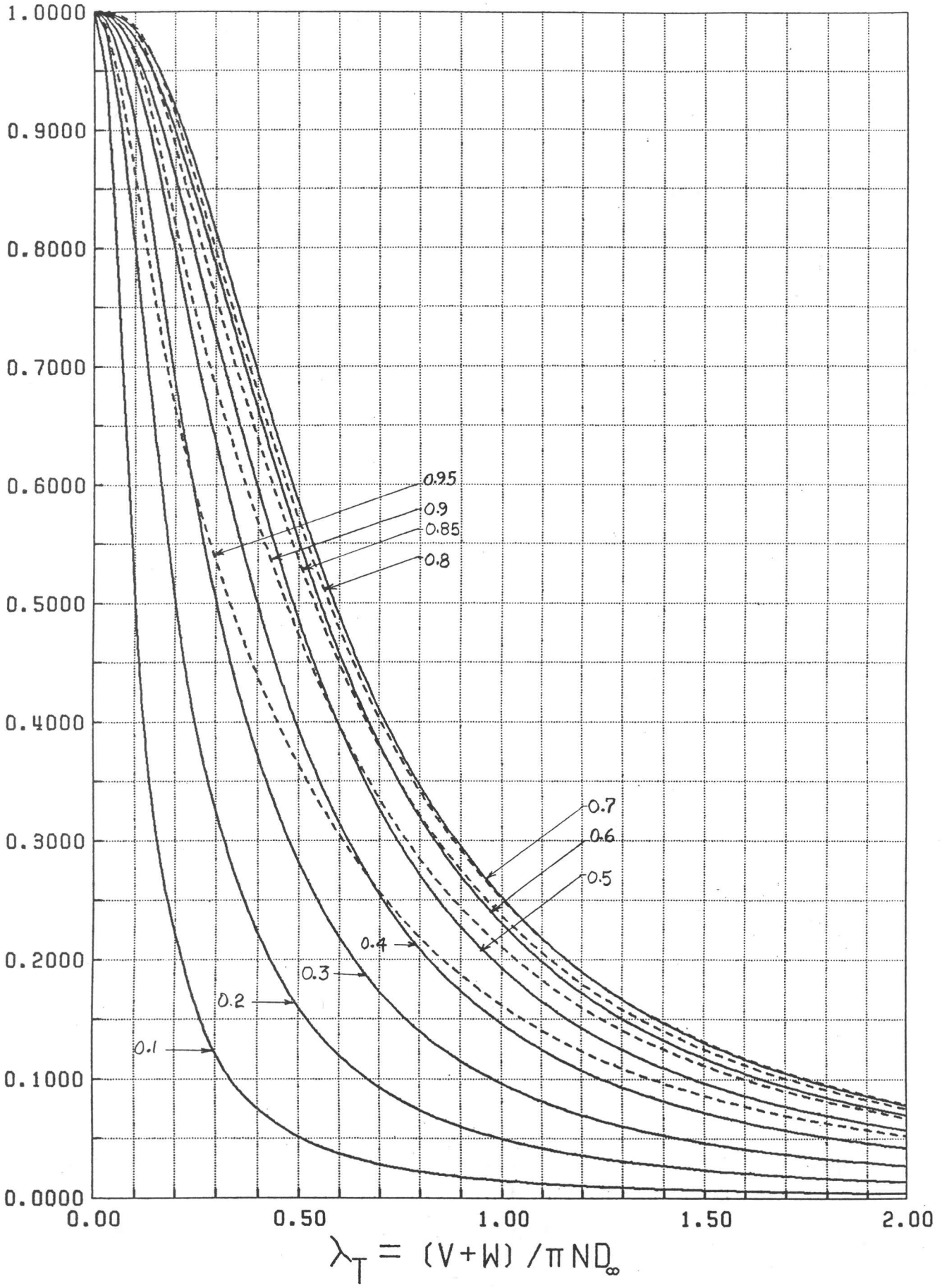

FIG. 24 OPTIMUM CIRCULATION AT CONSTANT RADIUS
6 BLADE PROPELLER

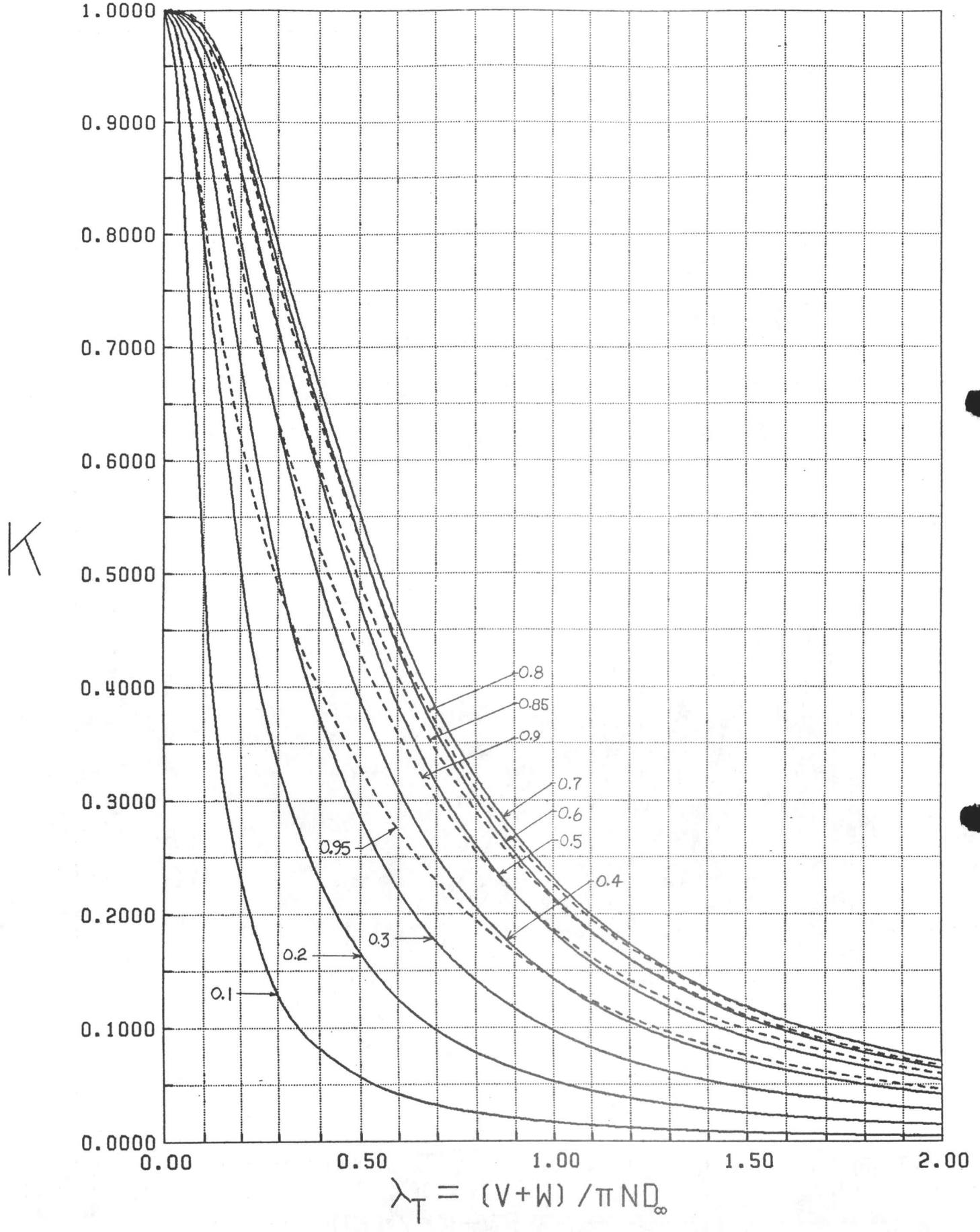

FIG. 23 OPTIMUM CIRCULATION AT CONSTANT RADIUS
5 BLADE PROPELLER

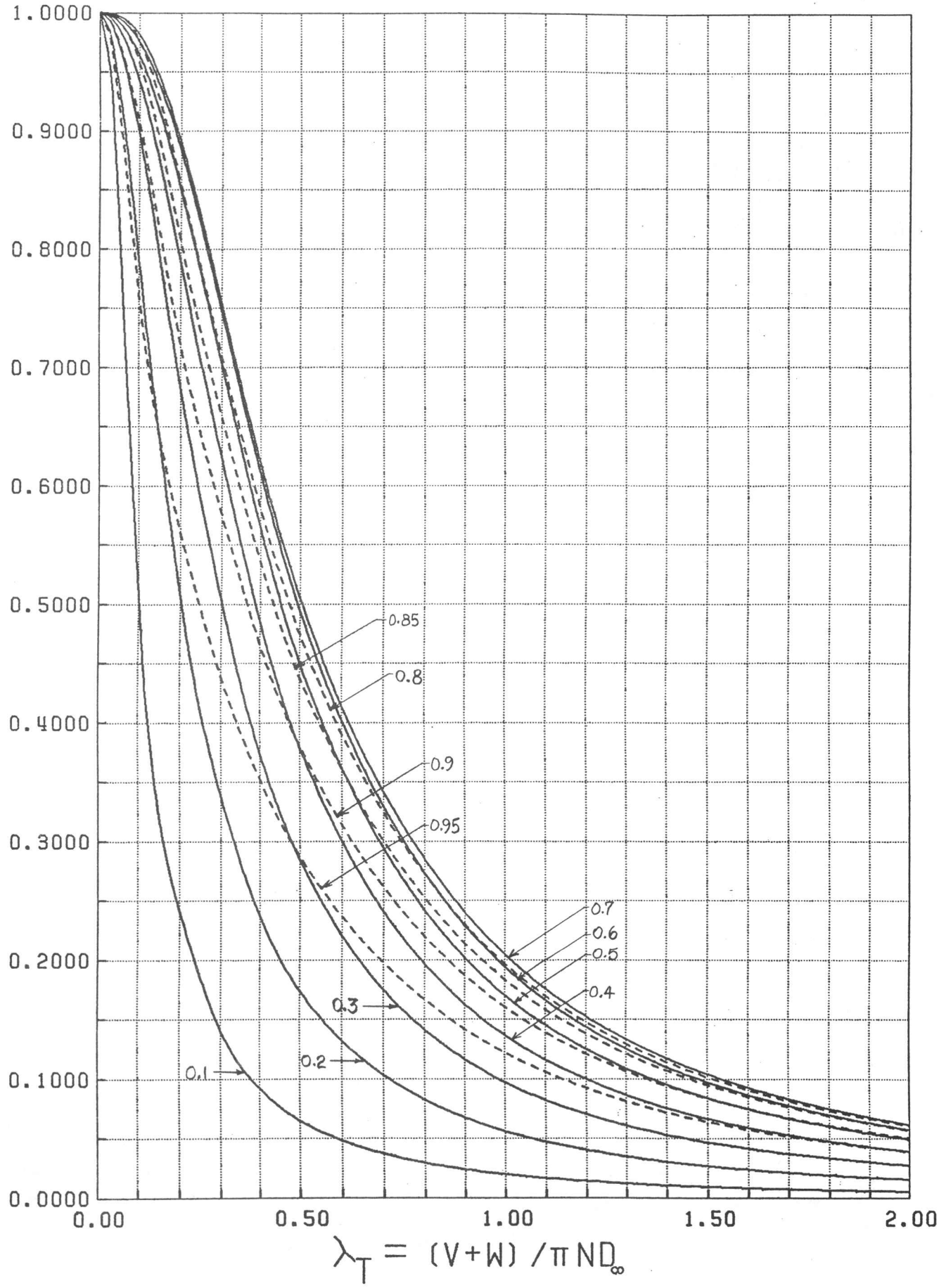

FIG. 22 OPTIMUM CIRCULATION AT CONSTANT RADIUS
4 BLADE PROPELLER

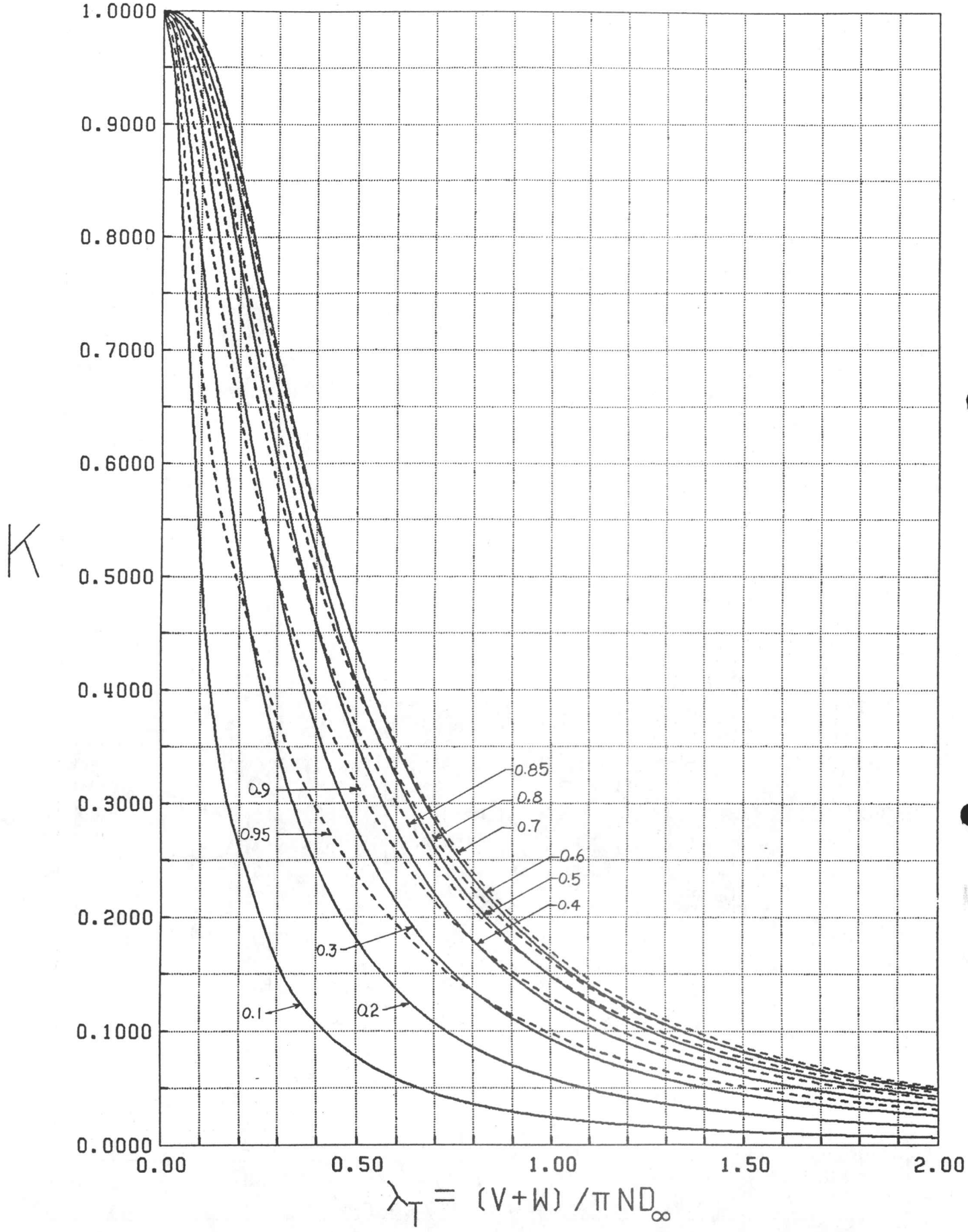

FIG. 21 OPTIMUM CIRCULATION AT CONSTANT RADIUS
3 BLADE PROPELLER

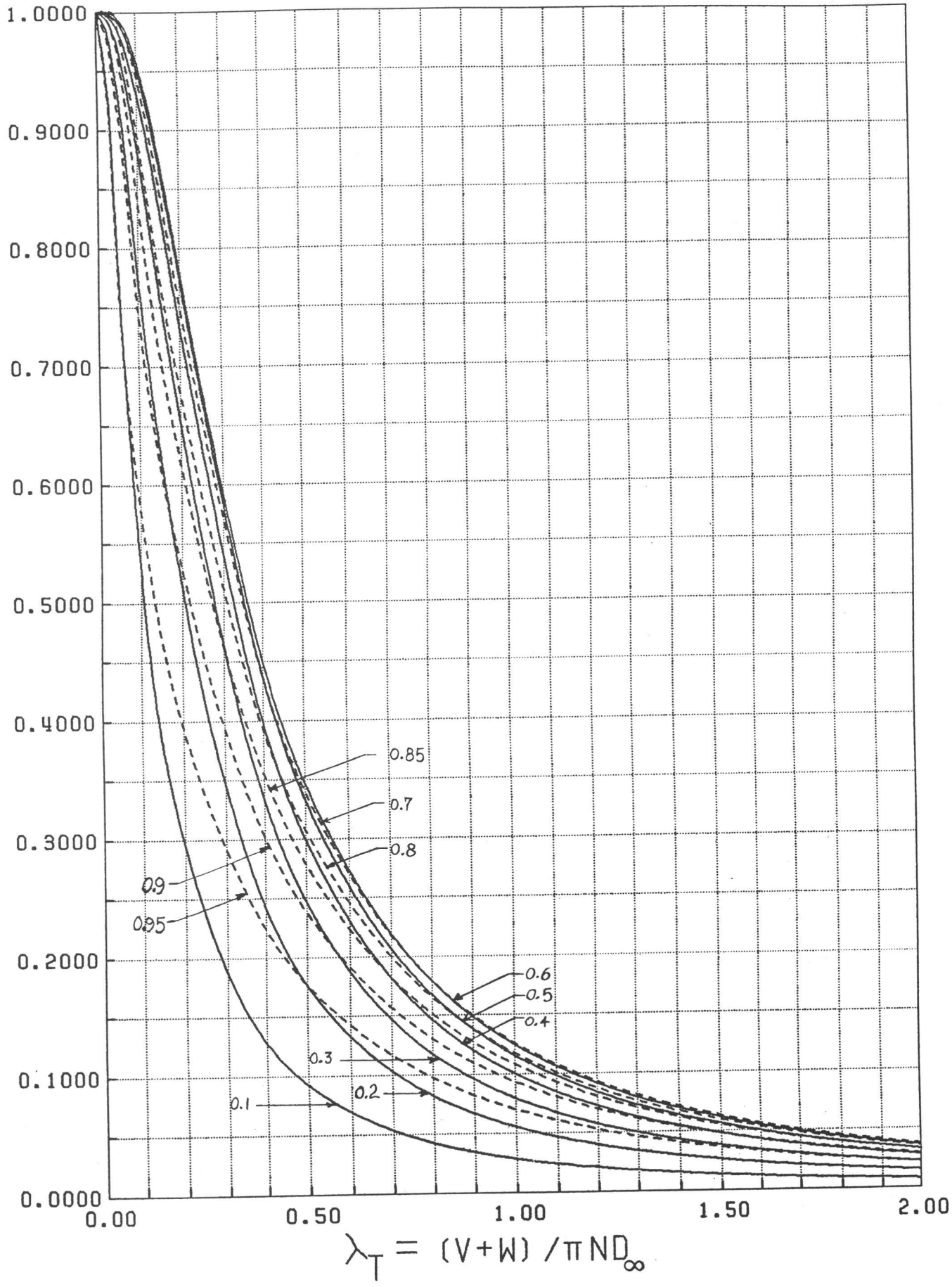

FIG. 20 OPTIMUM CIRCULATION AT CONSTANT RADIUS
2 BLADE PROPELLER

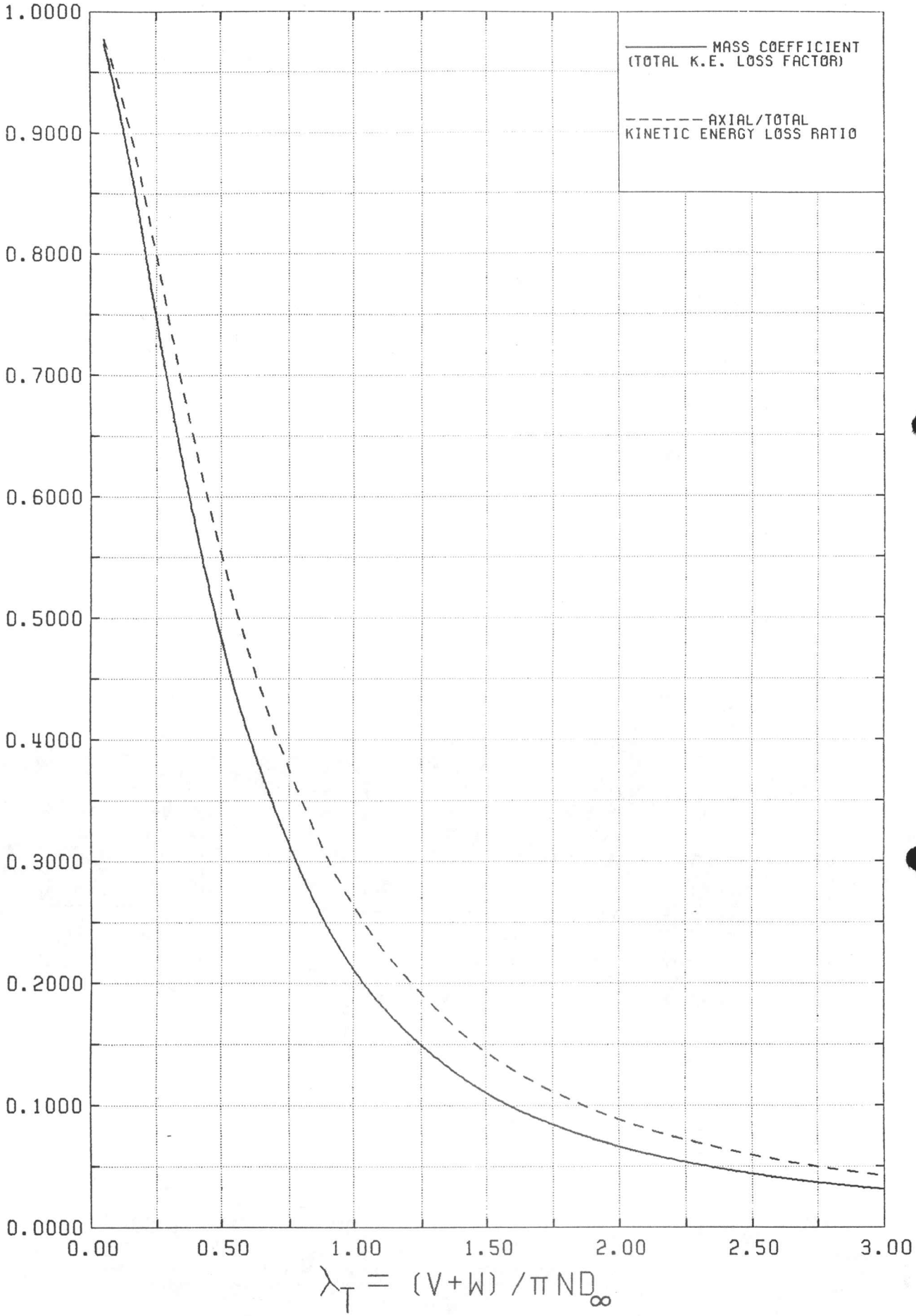

FIG.19 KINETIC ENERGY LOSS FACTORS
8 BLADE PROPELLER

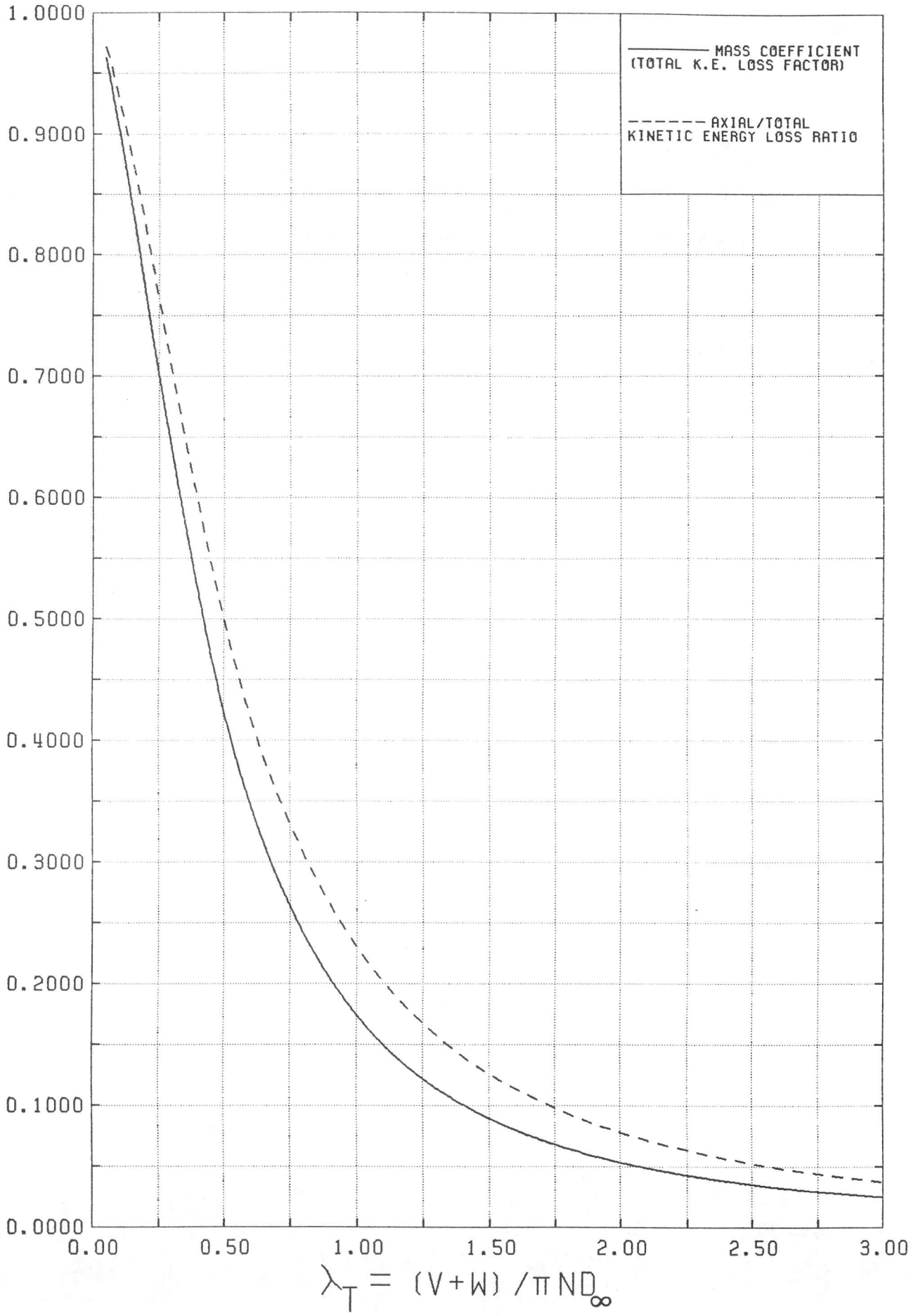

FIG.18 KINETIC ENERGY LOSS FACTORS
5 BLADE PROPELLER

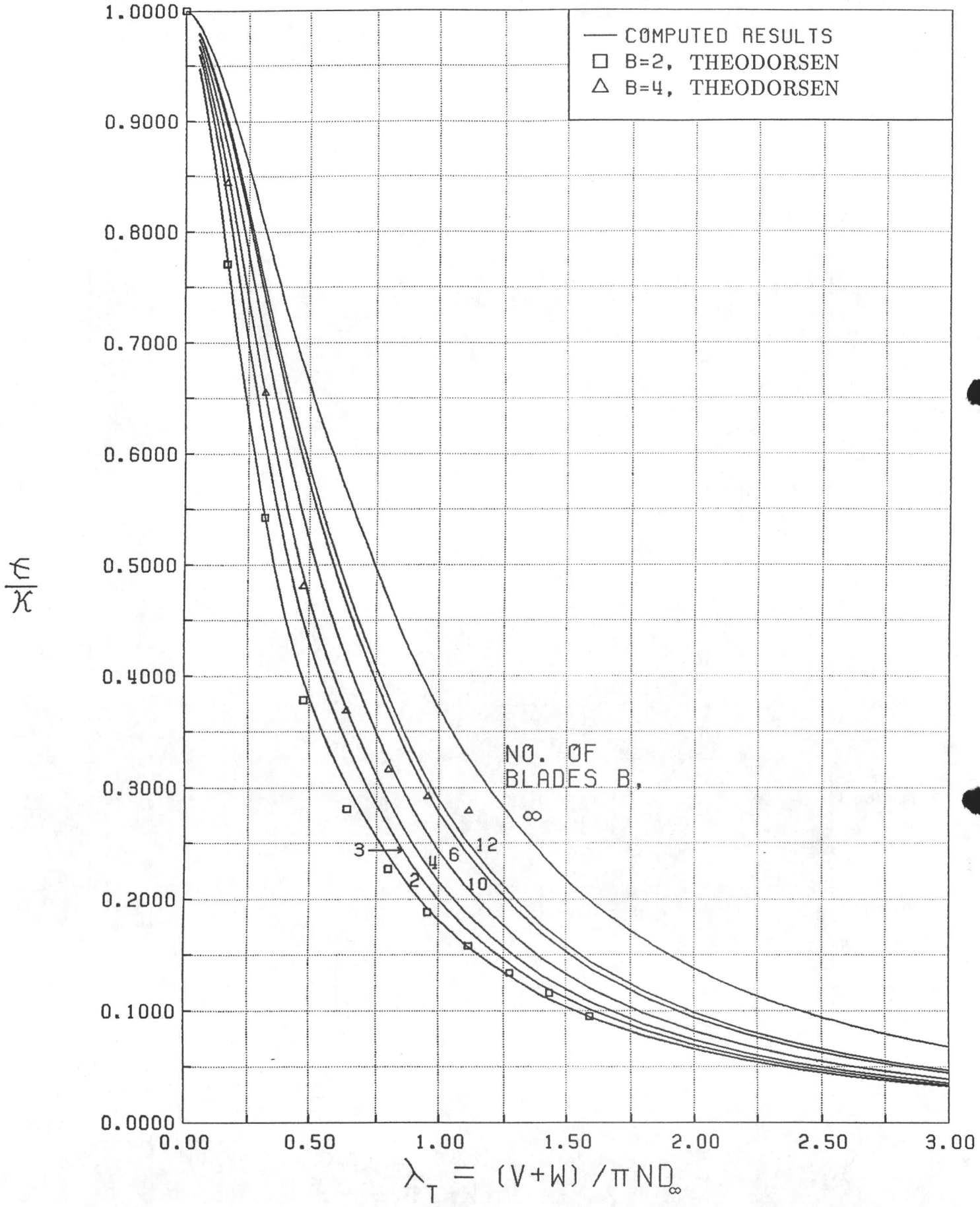

FIG. 17 AXIAL/TOTAL KINETIC ENERGY LOSS RATIO AT CONSTANT BLADE NUMBER

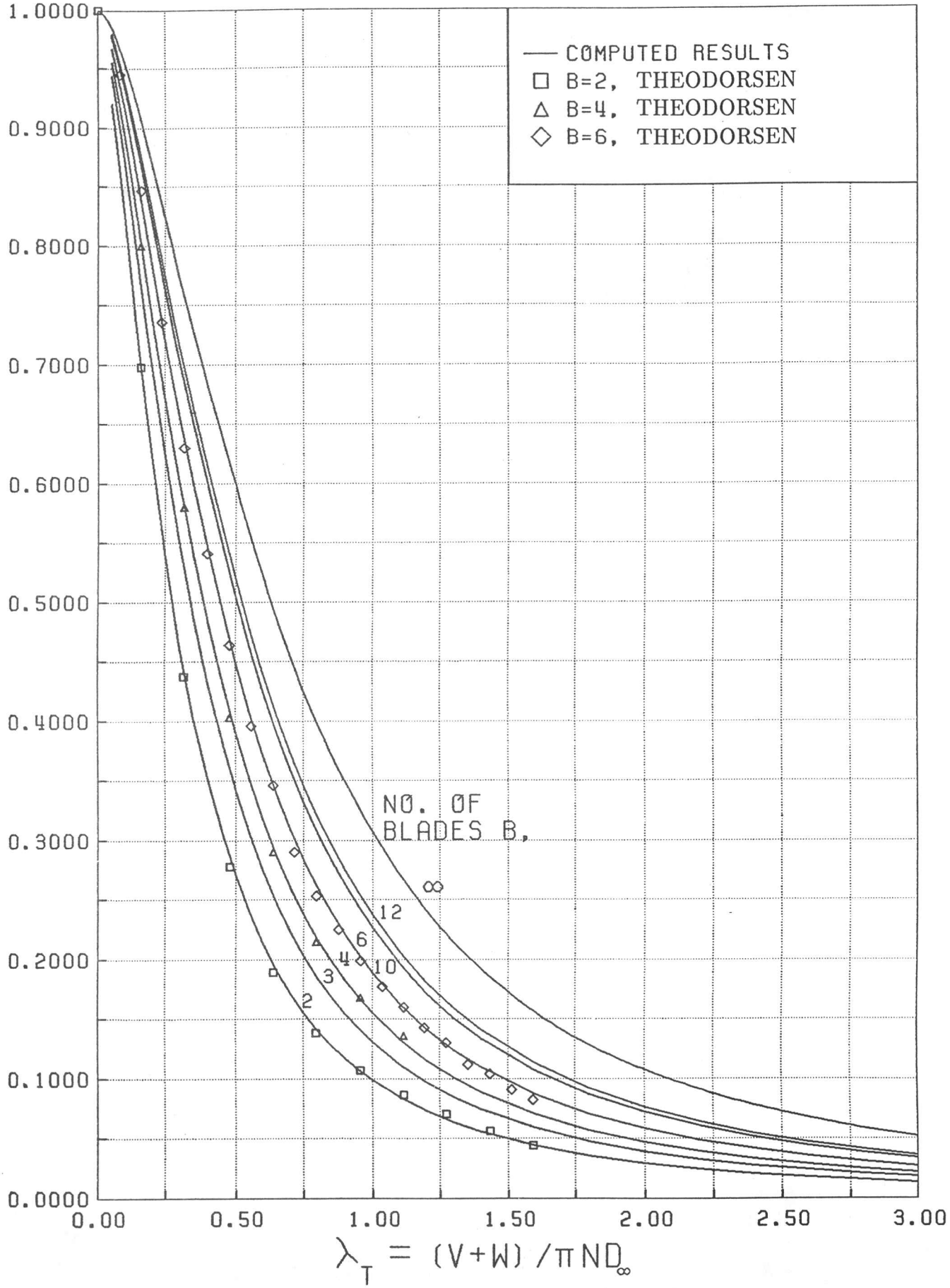

FIG. 16 MASS COEFFICIENT AT CONSTANT BLADE NUMBER

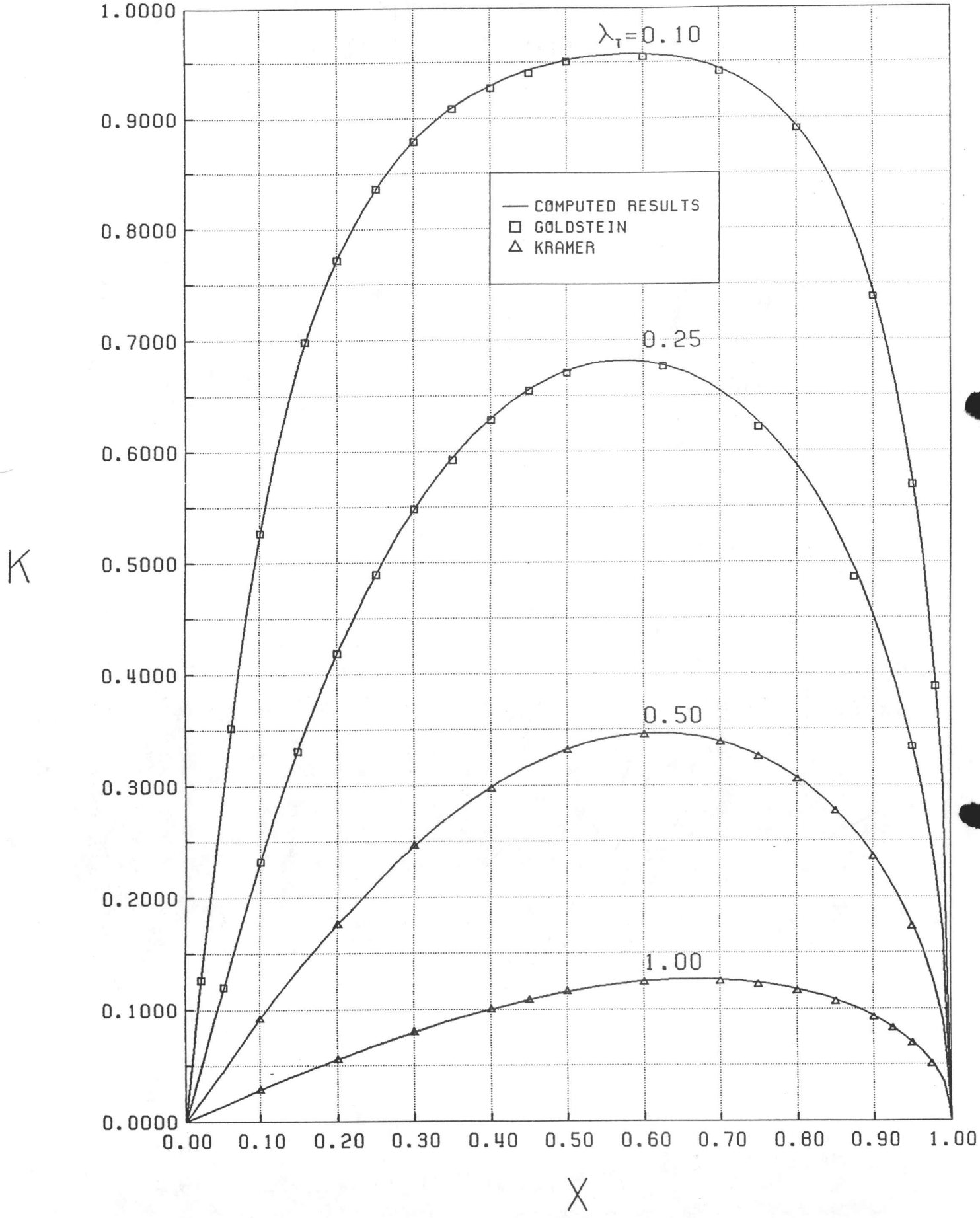

FIG. 15 IDEAL CIRCULATION FUNCTIONS
TWO BLADE PROPELLER

UTIAS Technical Note No. 271

University of Toronto, Institute for Aerospace Studies (UTIAS)
4925 Dufferin Street, Downsview, Ontario, Canada, M3H 5T6

IDEAL EFFICIENCY OF PROPELLERS BASED ON THEODORSEN'S THEORY:
A REVIEW AND COMPUTER STUDY, WITH EXTENDED PLUS SIMPLIFIED CHARTS
(With Foreword and Appendix Segments by H. S. Ribner)

Foster, Stephen P.

1. Propellers 2. Propeller efficiency 3. Propeller charts 4. Propeller theory 5. Theodorsen

I. Foster, Stephen P. II. UTIAS Technical Note No. 271

Ideal propeller performance is explored in an examination of Theodorsen's theory of propellers. This work presents an overview of the theory with analysis and interpretation. Computational methods are used in place of Theodorsen's analog techniques to calculate key parameters for more cases. In addition, relations between the fundamental quantities — thrust, power, advance, efficiency — are presented in his format plus a more convenient one that avoids iteration. Theodorsen's methodology is further applied to calculate the slipstream contraction; however, a slightly more general approach is taken with the removal of several light loading assumptions. A review of how the updated results may be applied to the design of single rotation propellers is also provided.

A limited number of copies of this report are printed for distribution free of charge.
Photocopies at $15.00 (Canadian) will be supplied when printed copies are no longer available.

UTIAS Technical Note No. 271

University of Toronto, Institute for Aerospace Studies (UTIAS)
4925 Dufferin Street, Downsview, Ontario, Canada, M3H 5T6

IDEAL EFFICIENCY OF PROPELLERS BASED ON THEODORSEN'S THEORY:
A REVIEW AND COMPUTER STUDY, WITH EXTENDED PLUS SIMPLIFIED CHARTS
(With Foreword and Appendix Segments by H. S. Ribner)

Foster, Stephen P.

1. Propellers 2. Propeller efficiency 3. Propeller charts 4. Propeller theory 5. Theodorsen

I. Foster, Stephen P. II. UTIAS Technical Note No. 271

Ideal propeller performance is explored in an examination of Theodorsen's theory of propellers. This work presents an overview of the theory with analysis and interpretation. Computational methods are used in place of Theodorsen's analog techniques to calculate key parameters for more cases. In addition, relations between the fundamental quantities — thrust, power, advance, efficiency — are presented in his format plus a more convenient one that avoids iteration. Theodorsen's methodology is further applied to calculate the slipstream contraction; however, a slightly more general approach is taken with the removal of several light loading assumptions. A review of how the updated results may be applied to the design of single rotation propellers is also provided.

A limited number of copies of this report are printed for distribution free of charge.
Photocopies at $15.00 (Canadian) will be supplied when printed copies are no longer available.

UTIAS Technical Note No. 271

University of Toronto, Institute for Aerospace Studies (UTIAS)
4925 Dufferin Street, Downsview, Ontario, Canada, M3H 5T6

IDEAL EFFICIENCY OF PROPELLERS BASED ON THEODORSEN'S THEORY:
A REVIEW AND COMPUTER STUDY, WITH EXTENDED PLUS SIMPLIFIED CHARTS
(With Foreword and Appendix Segments by H. S. Ribner)

Foster, Stephen P.

1. Propellers 2. Propeller efficiency 3. Propeller charts 4. Propeller theory 5. Theodorsen

I. Foster, Stephen P. II. UTIAS Technical Note No. 271

Ideal propeller performance is explored in an examination of Theodorsen's theory of propellers. This work presents an overview of the theory with analysis and interpretation. Computational methods are used in place of Theodorsen's analog techniques to calculate key parameters for more cases. In addition, relations between the fundamental quantities — thrust, power, advance, efficiency — are presented in his format plus a more convenient one that avoids iteration. Theodorsen's methodology is further applied to calculate the slipstream contraction; however, a slightly more general approach is taken with the removal of several light loading assumptions. A review of how the updated results may be applied to the design of single rotation propellers is also provided.

A limited number of copies of this report are printed for distribution free of charge.
Photocopies at $15.00 (Canadian) will be supplied when printed copies are no longer available.

UTIAS Technical Note No. 271

University of Toronto, Institute for Aerospace Studies (UTIAS)
4925 Dufferin Street, Downsview, Ontario, Canada, M3H 5T6

IDEAL EFFICIENCY OF PROPELLERS BASED ON THEODORSEN'S THEORY:
A REVIEW AND COMPUTER STUDY, WITH EXTENDED PLUS SIMPLIFIED CHARTS
(With Foreword and Appendix Segments by H. S. Ribner)

Foster, Stephen P.

1. Propellers 2. Propeller efficiency 3. Propeller charts 4. Propeller theory 5. Theodorsen

I. Foster, Stephen P. II. UTIAS Technical Note No. 271

Ideal propeller performance is explored in an examination of Theodorsen's theory of propellers. This work presents an overview of the theory with analysis and interpretation. Computational methods are used in place of Theodorsen's analog techniques to calculate key parameters for more cases. In addition, relations between the fundamental quantities — thrust, power, advance, efficiency — are presented in his format plus a more convenient one that avoids iteration. Theodorsen's methodology is further applied to calculate the slipstream contraction; however, a slightly more general approach is taken with the removal of several light loading assumptions. A review of how the updated results may be applied to the design of single rotation propellers is also provided.

A limited number of copies of this report are printed for distribution free of charge.
Photocopies at $15.00 (Canadian) will be supplied when printed copies are no longer available.